Mapping Gas Hydrate Dynamics in Porous Media

Experimental Studies of Gas Hydrates as a Source of CH_4 and Sink for CO_2

Stian Almenningen

Thesis for the degree of Philosophiae Doctor (PhD)
University of Bergen, Norway
2020

UNIVERSITY OF BERGEN

Mapping Gas Hydrate Dynamics in Porous Media

Experimental Studies of Gas Hydrates as a Source of CH_4 and Sink for CO_2

Stian Almenningen

Thesis for the degree of Philosophiae Doctor (PhD)
at the University of Bergen

Date of defense: 20.03.2020

Year: 2020

Title: Mapping Gas Hydrate Dynamics in Porous Media

Name: Stian Almenningen

Print: Skipnes Kommunikasjon / University of Bergen

Summary

The world needs more energy and the energy has to be more sustainable with respect to carbon dioxide (CO_2) emissions. This is the backdrop for studying the diverse applications of gas hydrates in nature. The ice-like substance is found worldwide as inclusions in the pore space of subsurface sediments and may affect the global energy supply and climate profoundly: 1) The large amounts of hydrate-bound natural gas, predominantly methane gas (CH_4), could provide the world with energy for decades. Global consumption of natural gas is expected to increase with 45% by 2030 (IEA, 2018b). Countries like Japan, China, India and South Korea are seeking to increase their energy security by developing natural gas production from subsurface accumulations of gas hydrates. 2) The natural affinity for CO_2 to form gas hydrates in the shallow subsurface could increase the storage capacity and security of carbon sequestration. Carbon capture and storage (CCS) is the removal of CO_2 from the atmosphere (or before it reaches the atmosphere) and subsequent long-term storage of the CO_2 in the subsurface. The projections of the IPCC that seeks to limit global warming to 1.5°C above the pre-industrial level rely on the use of CO_2 removal from the atmosphere on the order of 100 – 1000 gigatonnes of CO_2 ($GtCO_2$) during this century (IPCC, 2018). The formation of CO_2 hydrates could provide a self-sealing mechanism during CO_2 storage in saline aquifers which would decrease the risk of CO_2 leakage considerably. In both cases, fundamental knowledge about gas hydrates in porous media is needed.

The scientific work presented in this thesis contributes to the understanding of CH_4 and CO_2 hydrates in sediments with special emphasis on phase transitions and fluid flow in hydrate-saturated porous rock. Coupling the fluid flow with gas hydrate saturation and growth pattern is important to control the production rate of CH_4 gas from CH_4 gas hydrates and to model the sealing capacity of CO_2 gas hydrates. The rate and distribution of fluid flow during gas hydrate phase transitions in sediments were studied using a multiscale approach. Permeability measurements and quantitative mapping of water saturation were conducted on cylindrical Bentheim sandstone core plugs by high-precision pressure-volume-temperature (PVT) recordings and magnetic resonance

imaging (MRI). Pore-scale mapping of gas hydrate phase transitions was facilitated by etched silicon micromodels with pore networks replicating the geometry of real sandstone rock. The qualitative observations of phase transitions at pore-scale helped explain the flow rates measured at core-scale.

This thesis consists of seven scientific papers presenting a detailed description of gas hydrates effect on fluid flow in porous media. The first step in every gas hydrate experiment is to establish gas hydrates in the pore space and this was particularly investigated in **paper 1**. The effect of heterogeneous water distribution on CH_4 hydrate growth was resolved in Bentheim sandstone core plugs by MRI. The growth of CH_4 hydrate was more profound in regions of the core plug saturated with high water content and the final CH_4 hydrate distribution mirrored the initial water distribution. The same growth pattern of CH_4 hydrate was observed in the micromodel in **paper 2** and further developed into a conceptual growth model based on the initial pore-scale fluid distribution: A) A porous hydrate with encapsulated CH_4 gas surrounded by a shell of CH_4 hydrate formed in regions with high CH_4 gas saturation. B) A solid nonporous hydrate with no CH_4 gas formed in regions with low CH_4 gas saturation. The final hydrate morphology was mainly governed by local availability of water and mass transfer of water/CH_4 across the hydrate layer at the gas-water interface.

In **paper 3**, the controlling mechanisms on the rate of CH_4 gas recovery from CH_4 hydrates were investigated via constant pressure dissociation in Bentheim sandstone core plugs. The maximum rate of CH_4 gas recovery was governed by the CH_4 hydrate saturation and the rate was highest in the CH_4 hydrate saturation interval of 0.30 – 0.50 (frac.). The CH_4 gas recovery was slower at higher CH_4 hydrate saturation because of ineffective pressure transmission through the pore network and low relative permeability of the liberated CH_4 gas. The relative permeability to CH_4 (or CO_2) in gas hydrate-filled sandstone rock was measured in **paper 4**. The addition of solid hydrates in the pore space reduced the effective permeability to both CH_4 and CO_2 at constant CH_4 (or CO_2) saturation. The fitting exponent, *n,* in the modified Brooks-Corey curve increased during hydrate growth for both CH_4 and CO_2. The exponent increased from 2.7 to 3.6 when CH_4 hydrates formed in the pores and from 4.0 to 5.8 when CO_2

hydrates formed. The effective permeability to CH_4 (or CO_2) was more sensitive to inclusion of hydrates in the pores at low CH_4 (or CO_2) saturations, most likely because the limited CH_4 (or CO_2) phase was more prone to become disconnected and capillary immobilized.

The ability of CO_2 hydrates to immobilize CO_2 in water-saturated rock was explored in **paper 5-7**. The nature of CO_2 hydrate sealing during CO_2 injection was revealed at both micro- and core-scale in **paper 5**. Liquid CO_2 was completely immobilized by surrounding CO_2 hydrates that initially had formed at the CO_2-water interface and then later crystallized the water phase into nonporous CO_2 hydrates. The long-term sealing capability of the formed CO_2 hydrates was tested for different rock core samples in **paper 6-7**. In quartz-dominated rock core plugs, the CO_2 hydrate plug formed faster in tight rocks with low absolute permeability. Narrow pore throats in tight rocks were more easily obstructed by thin hydrate films that formed early in the nucleation process. The CO_2 hydrate formed later in an Edwards limestone core plug (K_{abs} = 80 mD) than in a Bentheim sandstone core plug (K_{abs} = 1500 mD) despite having a lower absolute permeability. The leakage rate of CO_2 through the CO_2 hydrate plug was higher in the limestone core plug compared to the sandstone core plug. The CO_2 hydrate self-sealing was therefore slower and less robust in carbonate rock compared to quartz-dominated rock.

Acknowledgements

I would like to acknowledge my supervisors Associate Professor Geir Ersland, Professor Martin Anders Fernø and Dr. Per Fotland for excellent guidance during my four years as a PhD candidate. A special thanks goes to my main supervisor Geir for mentoring me the last couple of years; your door was always open whenever I needed help.

I would also like to thank my fellow students and colleagues in the Reservoir Physics group at the University of Bergen. Thanks to groupleader Professor Arne Graue for providing exciting research oppurtunities both within the group and in collaboration with external partners.

The collaboration with Equinor in Bergen was very fruitful and I would like to express my gratitude for letting me use the MRI facility. The mechanical workshop at the Department of Physics and Technology was always helpful if something needed a repair.

Finally, I would like to thank friends and family for continuous support during my years at the university. A special thanks to Tharsicah for all your love and patience.

Contents

List of Papers

1) **Almenningen, S.**, Fotland, P. and G. Ersland, 2019. Magnetic Resonance Imaging of Methane Hydrate Formation and Dissociation in Sandstone with Dual Water Saturation. *Energies* **12**(17): 3231.

2) **Almenningen, S.**, Iden, E., Fernø, M.A. and G. Ersland, 2018. Salinity Effects on Pore-Scale Methane Gas Hydrate Dissociation. *J. Geophys. Res. Solid Earth* **123**(7): 5599-5608.

3) **Almenningen, S.**, Fotland, P., Fernø, M.A. and G. Ersland, 2019. An Experimental Investigation of Gas Production Rates During Depressurization of Sedimentary Methane Hydrates. *SPE J.* **24**(2): 522-530.

4) **Almenningen, S.**, Gauteplass, J., Hauge, L.P., Barth, T., Fernø, M.A. and G. Ersland, 2019. Measurements of CH_4 and CO_2 relative permeability in hydrate-bearing sandstone. *J. Petrol. Sci. Eng.* **177**: 880-888.

5) **Almenningen, S.**, Gauteplass, J., Fotland, P., Aastveit, G.L., Barth, T. and G. Ersland, 2018. Visualization of hydrate formation during CO_2 storage in water-saturated sandstone. *Int. J. Greenh. Gas Con.* **79**: 272-278.

6) Gauteplass, J., **Almenningen, S.**, Ersland, G., Barth, T., Yang, J. and A. Chapoy, 2020. Multiscale investigation of CO_2 hydrate self-sealing potential for carbon geo-sequestration. *Chem. Eng. J.* **381**: 122646.

7) **Almenningen, S.**, Betlem, P., Hussain, A., Roy, S., Senger, K. and G. Ersland, 2019. Demonstrating the potential of CO_2 hydrate self-sealing in Svalbard, Arctic Norway. *Int. J. Greenh. Gas Con.* **89**: 1-8.

List of Additional Papers

Almenningen, S., Flatlandsmo, J., Fernø, M.A., and G. Ersland, 2017. Multiscale Laboratory Verification of Depressurization for Production of Sedimentary Methane Hydrates. *SPE J.* **22**(01): 138-147.

Almenningen, S., Flatlandsmo, J., Kovscek, A.R., Fernø, M.A., and G. Ersland, 2017. Determination of pore-scale hydrate phase equilibria in sediments using lab-on-a-chip technology. *Lab Chip* **17**(23): 4070-4076.

Gauteplass, J., **Almenningen, S.**, Ersland, G., and T. Barth, 2018. Hydrate seal formation during laboratory CO_2 injection in a cold aquifer. *Int. J. Greenh. Gas Con.* **78**: 21-26.

Akhtar, N., Thomas, P.J., Svardal, B., **Almenningen, S.**, de Jong, E., Magnussen, S., Onck, P.R., Fernø, M.A., and B. Holst, 2018. Pillars or Pancakes? Self-Cleaning Surfaces without Coating. *Nano Lett.* **18**(12): 7509-7514.

Almenningen, S., Juliussen, H., and G. Ersland. *Permeability Measurements on Hydrate-Bearing Sandstone Cores with Excess Water.* Rev. Proc.: International Symposium of the Society of Core Analysts, Snowmass, Colorado, USA, August 22-26, 2016.

Almenningen, S. and G. Ersland. *Water Permeability Measurements on Hydrate-Saturated Sandstone Cores with Immobile Gas.* Rev. Proc.: International Symposium of the Society of Core Analysts, Vienna, Austria, August 27-31, 2017.

Almenningen, S., Gauteplass, J., Veland, V.F., Aastveit, G.L., Fotland, P., and G. Ersland. *High Field MRI of Hydrate Phase Transitions in Sandstone.* Rev. Proc.: International Symposium of the Society of Core Analysts, Trondheim, Norway, August 27-31, 2018.

Gauteplass, J., **Almenningen, S.**, and G. Ersland. *Storing CO_2 as Solid Hydrate in Shallow Aquifers: Electrical Resistivity Measurements in Hydrate-Bearing Sandstone.* Rev. Proc.: International Symposium of the Society of Core Analysts, Pau, France, August 26-30, 2019.

Almenningen, S., Flatlandsmo, J., Fernø, M.A., and G. Ersland. *Direct Pore-Level Visualization of Methane Hydrate Growth in an Authentic Sandstone Replicate*. The 9th International Conference on Gas Hydrates, Denver, Colorado, USA, June 25-30, 2017.

1. Introduction

The global energy demand is still increasing as it has been over the last 50 years. The world total primary energy supply was 6101 millions of tonnes of oil equivalent (Mtoe) in 1973 and has steadily increased to 13761 Mtoe in 2016 (IEA, 2018a). The projections for the next decades show a continuous increase of primary energy consumption and the consumption is expected to approach 15000 Mtoe in the 2020s, exceed 15000 Mtoe in the 2030s, and grow to 18000 Mtoe in the 2040s (BP, 2019). The World Energy Outlook 2018 (IEA, 2018b) expects the global energy demand to increase by more than 25% to 2040, and the International Energy Outlook 2018 (EIA, 2018) projects that the consumption will be 18600 Mtoe by the same time. The growth is primarily driven by rising incomes and increasing populations in developing countries, led by India (IEA, 2018b). The number of people without access to electricity dropped below 1 billion in 2017, but this number is expected to remain above 700 millions even in year 2040 (IEA, 2018b). Moreover, 3 billion people lack access to clean cooking fuels and facilities to date (UN, 2019). The increase in demand of energy takes place despite significant ongoing improvements in energy efficiency (IEA, 2018b). Accordingly, there is a great need for more and affordable energy in the coming decades.

There has been significant changes the last decade regarding which energy fuels are preferred and utilized by the consumer. In light of the severe consequences on global climate by emitting anthropogenic carbon dioxide (CO_2) into the atmosphere, the energy sector has turned from depending heavily on fossil fuels to include increasing contributions from renewable energy resources. Renewable energy, excluding hydropower, contributes to 4% of the primary energy today compared to a share of practically zero 20 years ago. In 2040, this number is expected to grow to approximately 15% (BP, 2019). Similarly, the share of generation of electrical power from renewables is forecasted to rise from 25% today to around 40% in 2040 (IEA, 2018b). Development of a more sustainable energy supply worldwide is paramount in order to reach the CO_2 mitigation goals outlined in the Paris Agreement of 2015. The agreement emphasizes that the global average temperature should be limited to well

below 2°C above pre-industrial levels to minimize the risks and consequences of climate change (UN, 2015). These risks include regional warming of extreme temperatures, more frequent heavy precipitation, and increased occurrences of droughts, along with global mean sea level rise affecting human and ecological systems of low-lying coastal areas (IPCC, 2018). Avoiding a temperature increase of 2°C, depends on reducing the CO_2 emissions by 25% from 2010 levels by 2030 and reaching net zero emissions around 2070 (IPCC, 2018). However, the projections on CO_2 emissions are not in line with the CO_2 mitigations that are needed. The World Energy Outlook 2018 (IEA, 2018b) expects a slight increase in the energy-related CO_2 emissions towards 2040, similar to the 7% increase projected by one scenario in the BP Energy Outlook 2019 (BP, 2019). All available options must therefore be employed to strive for lower CO_2 emissions. One of these options is the capture of CO_2 from emission sources, including capture of CO_2 from the atmosphere, and subsequent storage in the underground, called carbon capture and storage (CCS). The CO_2 is then temporarily removed from the carbon cycle in the period the CO_2 resides in the storage site and cannot contribute to global warming. The storage potential in geological formations is estimated to be 200 – 2000 gigatonnes of CO_2 ($GtCO_2$) (IPCC, 2005), which is quite substantial considering the present yearly emissions of anthropogenic CO_2 of approximately 42 $GtCO_2$ (IPCC, 2018). In fact, all scenarios that limit global warming to 1.5°C rely on the use of CO_2 removal from the atmosphere on the order of 100 – 1000 $GtCO_2$ over the present century (IPCC, 2018). Rapid and secure implementation of geological CO_2 sequestration is therefore essential to meet the required need for reducing CO_2 emissions.

The apparent conflict between growing energy demand and the need to reduce anthropogenic CO_2 emissions is a vast challenge that must be addressed by a range of approaches. One natural occurring compound that could contribute constructively to both challenges is natural gas hydrates. This fossil energy resource is made up of natural gas entrapped by crystalline water and is stabilized by low temperatures and moderate pressures. Ambient conditions reconcilable with gas hydrate growth are found in sub permafrost sediments and in marine sediments beneath water columns

greater than ~350-600 m. Natural gas hydrates may be exploited as an energy resource by producing the natural gas that is trapped in the hydrate structure. The energy density is high as one m^3 of hydrate releases up to 180 m^3 of natural gas when brought to the surface (Ruppel and Kessler, 2017). This fact, coupled with abundant and widespread accumulations, ensure an astonishing energy potential associated with hydrate exploitation. The exact amount of natural gas entrapped in hydrates is difficult to quantify, but a widely used statement is that the energy content of hydrates is in the same order as the total combined energy content of conventional natural gas, oil and coal (Milkov, 2004). Tapping into only a fraction of the global hydrate resources will provide significant amounts of natural gas to the energy market. Natural gas is fossil-based and will upon combustion add to the global CO_2 emissions. However, if the extra natural gas coming from hydrates is used as a substitute for burning of oil and coal, the net effect is reduced carbon emissions. The release of CO_2 upon combustion of natural gas is 0.18 kg/kWh compared to 0.25 for heating oil and 0.33-0.35 for coal (EIA, 2019). Shifting the use of oil and coal to natural gas is a first step in reducing the CO_2 emissions while maintaining the energy supply until permanent solutions for carbon-neutral energy supply is available. The burning of natural gas in power plants can also become carbon-neutral by applying carbon capture to the process. The captured carbon must then be transported and stored in a safe location, for instance in subsurface saline aquifers. Aquifer storage relies on a geological trap to be situated above the storage site in order to keep the injected CO_2 in place. The density of CO_2 is lower than water and buoyancy will cause the CO_2 to flow up towards the surface. The CO_2 is safely stored in the aquifer as long as the integrity of the seal is intact. However, there will always be uncertainties related to the areal extent and strength of the proposed seal. In this regard, gas hydrates may play a critical part in limiting the risk of CO_2 leakage from the storage site through the seal. CO_2 is able to form gas hydrates at temperatures and pressures found in the shallow subsurface offshore and in permafrost-affected sediments. Leaking CO_2 that eventually migrates into the CO_2 hydrate stability zone becomes immobilized as it reacts with formation water and crystallizes into solid hydrates. The formation of CO_2 hydrates severely prolongs the residence time of the

CO_2 in the subsurface and provides a secondary safety factor during geological carbon sequestration.

The work presented in this thesis is aimed at improving the understanding of sedimentary gas hydrates in nature. Methane (CH_4) and CO_2 hydrates were formed in a series of experiments inside rock core plugs and micromodels in the laboratory. The focus of the CH_4 hydrate experiments was to investigate different parameters possibly affecting the hydrate formation and dissociation process. The results of this work are valuable in order to understand better the mechanisms controlling hydrate formation and stability in nature, and the results give improved understanding of the mobilization of fluids during production of natural gas hydrates. The CO_2 hydrate experiments were performed with emphasis on how the formation of CO_2 hydrates reduced the flow of CO_2 through the pore network. The strength of the formed CO_2 hydrate seal and the leakage rate of CO_2 through the seal were evaluated. The output of this work demonstrates the feasibility of CO_2 hydrate as a secondary safety factor during underground storage of CO_2. The next chapter gives a brief introduction to gas hydrates in nature and is followed by an in-depth discussion of the results from this work.

2. Theory

2.1 Gas Hydrates Fundamentals

Gas hydrates are a part of the clathrate family of substances and were first discovered in 1810 by Sir Humphrey Davy (Sloan and Koh, 2008). In hydrates, water molecules are arranged systematically in a crystal lattice that is stabilized by the inclusion of guest molecules. The guest molecules are situated in cavities formed in-between the hydrogen-bonded water molecules and contribute to the cavity stability by dispersion forces (Sloan and Koh, 2008). The list of guest molecules include small hydrophobic molecules like CH_4 and N_2, water-soluble acid gases like CO_2 and H_2S, as well as higher-order hydrocarbons like propane (Sloan and Koh, 2008). The different guest molecules can form different hydrate structures based on their molecular weight and geometric shape. Structure I hydrate is most common in nature and consists of two small cavities and six large cavities per symmetrical unit of 46 water molecules. CH_4 and CO_2 form structure I hydrate. The CH_4 molecule can in principle fit both cavities and the theoretical hydration number becomes 5.75:

$$CH_4 + 5.75H_2O \leftrightarrow CH_4\ hydrate. \quad (1)$$

In practice, the formation process is not completely stoichiometric and there will exist some empty cavities. An experimentally determined hydration number of 5.99 is used in this work to calculate the number of water molecules that reacts with each CH_4 molecule (Circone et al., 2005). The larger CO_2 molecule is harder to fit into the small cavities and the hydration number of CO_2 is generally higher than for CH_4. The hydration number for CO_2 is predicted to range between 6.2 and 6.4 for the particular pressure and temperature conditions used in this work (Udachin et al., 2001; Henning et al., 2000). The other natural occurring hydrate structure, which is formed by larger hydrocarbon molecules, is structure II. This hydrate structure is composed of 16 small cavities and 8 large cavities. Independent of the particular hydrate structure, the dense packing of the cavities within hydrates results in a significant up-concentration of CH_4 in the hydrate structure. Hence, one m^3 of CH_4 hydrate releases up to 180 m^3 of CH_4 gas at standard temperature and pressure (Ruppel and Kessler, 2017).

In addition to govern the hydrate structure, the guest molecule also determines the particular temperature and pressure at which hydrates form (**Fig. 1**). Hydrate growth relies on favorable thermodynamics, i.e. sufficiently high pressure and sufficiently low temperature, and availability of water and guest molecules. The hydrate formation process starts as a competition between nucleation and decomposition of the hydrate forming molecules until clusters of hydrate reach a critical size. At this point, termed the induction time, the Gibbs free energy is minimized by further hydrate growth. The hydrate formation will then continue with large crystals growing at the expense of smaller crystals. The growth continues as long as water and guest molecules are continuously supplied and the thermodynamics remain favorable. The addition of salt in the hydrate-forming water will act as a hydrate inhibitor. Salt ions are not incorporated into the hydrate crystal lattice and up-concentrates in the water phase during hydrate growth. The increased salinity leads to a lowering of the chemical potential of water in the liquid phase and eventually the water molecules prefer to remain as liquid water instead of forming hydrates. At this critical salinity, the hydrate formation process stops as the residual water is in equilibrium with the hydrate. The pressure and/or temperature must then be adjusted to bring the system back to hydrate forming conditions (Fig. 1).

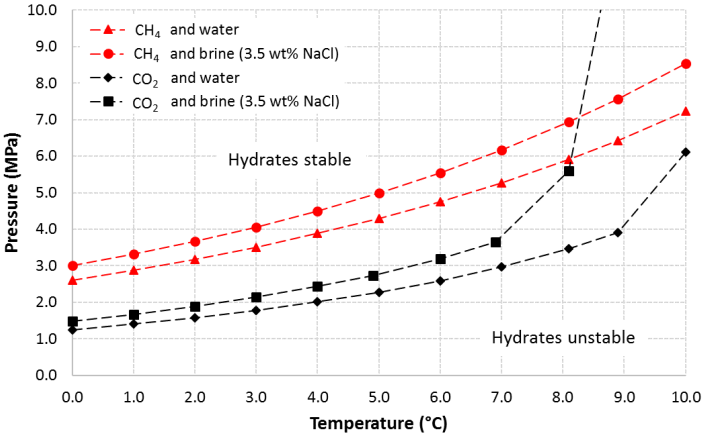

Figure 1. Pressure and temperature plot of gas hydrate stability of CH_4 and CO_2 with and without sodium chloride in the water. The stability curves are calculated using the CSMGem software (CSMGem, 2015).

2.2 Gas Hydrates in Nature

In the 1960s, it was first realized that gas hydrates exist in nature. Gas hydrates may form wherever natural gas is in contact with pore water at hydrate-forming pressure and temperature conditions. The origin of the natural gas in the subsurface is usually either biogenic or thermogenic, and CH_4 is by far the predominant hydrate former in nature. Subsurface locations where CH_4 hydrates may form include onshore permafrost-sediments, artic subsea permafrost-sediments, subglacial sediments, and offshore marine sediments (Ruppel and Kessler, 2017). The majority (~99%) of CH_4 hydrates are found in marine sediments while only around 1% are believed to exist onshore (Ruppel and Kessler, 2017). Sedimentary intervals containing CH_4 hydrates are sampled by coring/well-logging or inferred from seismic acquisition, which causes large uncertainties in the global amount of CH_4 hydrates. The estimated volume of hydrate-bound CH_4 gas has decreased the last decades as the knowledge of sedimentary hydrates has evolved. Boswell and Collett (2011) report a global estimate of around 1500 gigatonnes of carbon (GtC) which fits into the range of 500 – 2500 GtC given by Milkov (2004). Other estimates are lower (Archer et al., 2009) and some are higher (Klauda and Sandler, 2005). Compared to the 5000 GtC stemming from conventional fossil fuels (Milkov, 2004), the amount of carbon present in CH_4 hydrates is significant regardless of which estimate is used. Additionally, the substantial volumes of CH_4 hydrates are globally distributed on all continents. The theoretical gas hydrate stability zone has been mapped worldwide (Kretschmer et al., 2015) and shows great potential of finding CH_4 hydrates close to the seafloor in deepwater continental slopes. This makes CH_4 hydrates an attractive energy resource for many countries trying to improve their energy security.

The distribution of gas hydrates within sediments in nature depends on the prevailing lithology, thermodynamic condition, and transport mechanism of gas and water. Gas hydrates have been observed to occupy the intergranular pore space of sand and silt, act as grain-displacing in the form of veins and nodules, fill fractures, and be massive containing nearly no sediments (**Fig. 2**) (Collett et al., 2009). You et al. (2019) divided the gas hydrate occurrences in nature into five different types: 1) Regionally

disseminated hydrate in muddy sediments, 2) Fracture-filling hydrate at nonvent sites, 3) Enriched hydrate at the base of the hydrate stability zone in muddy sediments, 4) Concentrated hydrate at vent sites, and 5) Concentrated hydrate in sand-rich intervals. The gas hydrate saturation varies tremendously in different lithological units. The saturation is typically 1-3% in fine-grained marine sediments with local exceptions of up to 30% (Boswell and Collett, 2011; Lee and Collett, 2008). In coarse-grained sand, the gas hydrate saturation is usually in the range of 60% to as high as 90% (Collett et al., 2009). The pore-scale distribution of hydrates in coarse-grained sediments has also been investigated in the laboratory. Especially elastic wave velocities have been used to infer whether hydrates form within the pore fluid (pore-filling), on individual grains (grain-coating), or at grain contacts (grain-cementing) (Dvorkin et al., 1994; Helgerud et al., 1999). Several of the studies suggest that hydrates form at grain contacts when the initial water saturation is low (Priest et al., 2005; Waite et al., 2004) and within the pore fluid when the initial water saturation is high (Hu et al., 2010). The same result is reflected by the choosing of the formation technique. Forming hydrates by the "excess gas" method, i.e. finite amount of water in the core, results in hydrates forming on the grain surface while the "excess water" method results in pore-filling hydrate for hydrate saturations less than 40% (Priest et al., 2009; Lee et al., 2010). The pore-scale distribution of hydrates is thus heavily affected by the initial gas and water saturation prior to hydrate formation. Formation of hydrates in nature is believed dominated by nucleation of dissolved CH_4 in the pore water (Collett et al., 2009) and the "excess water" formation method is therefore likely the best approach to mimic the hydrate morphology found in nature. It should be noted that the hydrate never attaches directly to the grain surface in coarse-grained sediments independent of the starting fluid saturation and formation method (Cook and Waite, 2018). A layer of water is observed to exist between sediment grains and the hydrate (Chaouachi et al., 2015; Kerkar et al., 2014). The load-bearing effect on sediments observed at hydrate saturations above 40% is explained by the interconnectivity of hydrates between pores which provides stiffness and restricts grain movement without actual hydrate adhesion to the grain surface (Cook and Waite, 2018).

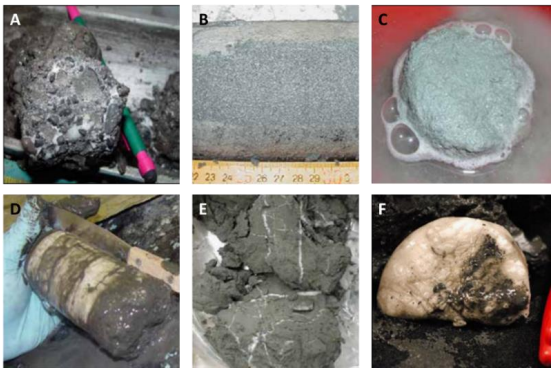

Figure 2. Different accumulations of gas hydrates (white) found in nature. A: Conglomerate of gas hydrates and coarse-grained sand from Arctic Canada (courtesy JOGMEC-NRCan-USGS). B: Pore-filling gas hydrate in sand from offshore Japan (courtesy JOGMEC). C: Disseminated gas hydrates in fine-grained sediment from offshore China (courtesy GMGS-01 Science Party). D: Massive grain-displacing gas hydrates in fine-grained sediment from offshore India (courtesy NGHP-Expedition-01). E: Thin veins of grain-displacing gas hydrates in fine-grained sediment from offshore Korea (courtesy UBGH-Expedition-01). F: Nodule of gas hydrates containing fine-grained sediments from offshore India (courtesy NGHP-Expedition-01). Modified from the compilation of images presented in Beaudoin et al. (2014).

2.3 CH_4 Production from Gas Hydrates

The category of hydrate deposits that is most likely to be producible in the near future is highly concentrated hydrates in sand. These hydrate deposits are the only ones that are labeled technically recoverable resources by Boswell and Collett (2011) and are estimated to constitute a volume in the order of 150 GtC. The main advantage of these deposits compared to distributed hydrates in clayey sediments is the orders of magnitude higher intrinsic permeability. The high permeability of the sand results in highly concentrated hydrate accumulations, effective transference of pressure and/or temperature perturbations during production, and sustainable flow of gas from the dissociation zone to the wellbore (Boswell and Collett, 2011). The most energy-efficient method to induce hydrate dissociation and CH_4 gas production is pressure depletion potentially aided by heating of the wellbore (Liang et al., 2018). The pressure drawdown can be initiated by producing the liquid water (and possibly free gas) in the reservoir from a single well. As the pressure is lowered below the hydrate stability

pressure, hydrate dissociates into liquid water and CH_4 gas. The success of the specific gas production relies heavily on the interplay between permeability, saturation and distribution of fluids, and heat transfer of the formation (Moridis et al., 2011). The endothermic nature of hydrate dissociation lowers the reservoir temperature immediately and local reformation of hydrates and ice formation may take place, especially in the near-well region (Moridis and Reagan, 2007). Introducing geomechanical instabilities with potential collapse of the wellbore and even large-scale deformations, as well as severe sand production with related strain on the equipment, are other concerns associated with dissociating the hydrate in-place. Another production scheme is therefore proposed and is showed to work in the laboratory (Graue et al., 2008), where CO_2 is injected into hydrate-filled sandstone. The CO_2 enters spontaneously into the hydrate structure and exchanges the hydrate-bound CH_4 gas because of favorable thermodynamics. CH_4 gas is then produced without large-scale dissociation of the hydrates, and thereby minimizing the risk of altering the geomechanical stability of the formation. However, this production method is even more reliant on significant permeability to facilitate throughput of the injected CO_2.

To date, there has been no long-term production of CH_4 gas from hydrate reservoirs. The production tests that have been conducted this far have merely demonstrated the possibility of producing CH_4 gas from hydrate during a short time period without assessing the long-term geomechanical stability of the formation. The first intentional gas production from CH_4 hydrates were demonstrated in the Mackenzie Delta, Canada in 2002. A total of 468 m^3 of gas was produced during five days by circulating hot water in the well (Hancock et al., 2005). A follow up test in 2007/2008 resulted in the production of 13 000 m^3 of gas during six days of depressurization. The test was initially halted by severe sand production but six days of production was later enabled by successfully implementing a sand screen into the wellbore (Yamamoto and Dallimore, 2008). In 2012, cumulative gas (CH_4) production reached 24 410 m^3 after 31.5 days of production in the Ignik Sikumi field experiment within the Prudhoe Bay Unit on the Alaska North Slope (Boswell et al., 2017). The production followed 14 days of injecting a mixture of nitrogen and CO_2 into the hydrate formation, and the

CH_4 gas was produced both above and below the hydrate stability pressure. Initial sand production was observed despite using a 200 μm sand screen, but virtually no sand was produced during the last stage of the production when the bottom-hole pressure and flow rate had stabilized (Boswell et al., 2017). The first offshore production test was performed in 2013 at the Daini Atsumi Knoll off the coast of Japan. A 60 m thick zone of hydrate-filled sand was produced by pressure depletion over the course of six days (Konno et al., 2017). A total of 119 500 m^3 of gas was produced before the production was terminated due to abrupt sand production (Konno et al., 2017). A prolonged production test was repeated in the same area in 2017 utilizing two production wells. The first well produced 41 000 m^3 of gas during 12 days of operation before the well was once again shut down because of unmanageable sand production (Yamamoto et al., 2019). The other well was opened after the closing of the first well and produced 222 500 m^3 of gas during a 24 days period. No sand problems were experienced in the second well. However, the water production rate was significantly higher than expected and limited the magnitude of the pressure drawdown (Yamamoto et al., 2019). In the same year, China conducted its first offshore production test from a clayey-silt hydrate reservoir located in the Shenhu area in the South China Sea. The production test lasted for 60 days and the cumulative gas production was reported to be 309 000 m^3 (Li et al., 2018). All of these short production tests have demonstrated the potential of producing gas from hydrate deposits and have highlighted the need for special requirements on equipment and subsea systems. The next significant contribution towards commercial production is an anticipated one-year-long flow test onshore in Alaska which will provide longer-term production data (Yamamoto et al., 2019).

2.4 Permeability of Sedimentary Gas Hydrates

A key parameter controlling the gas production rate from hydrate reservoirs is the permeability of the formation (Moridis et al., 2007; Reagan et al., 2008). The intrinsic permeability of the sediment affects the flow rate of gas and water towards the production well and the effective permeability of the hydrate-filled sediment controls the propagation rate of the dissociation front through the formation. A variety of permeability models for hydrate-bearing sediments are provided by Kleinberg et al.

(2003). A widely used model that relates relative permeability to water, k_{rw}, to hydrate saturation, S_H, originates from Masuda et al. (1997):

$$k_{rw} = (1 - S_H)^N. \quad (2)$$

The exponent N is a fitting parameter that reflects the hydrate pore-occupancy. The value of N has been empirically estimated to range from 3-5 (Kumar et al., 2010) to 38 (Li et al., 2013) in different studies. The model is only applicable to sedimentary hydrates together with one fluid phase, such as when the pore space is saturated with hydrates and liquid water supersaturated with dissolved CH_4. During a production scenario when hydrates dissociate into liquid water and CH_4 gas, the flow is characterized by each fluids relative permeability in the presence of hydrates. This is usually managed in a two-step process where the effect of hydrate saturation on the absolute permeability is considered first. The absolute permeability reduction is modelled in the reservoir simulator TOUGH+HYDRATEv1.5 as (Moridis and Pruess, 2014):

$$\frac{k(S_H)}{k_0} = \left(\frac{\phi(S_H) - \phi_c}{\phi_0 - \phi_c}\right)^n, \quad (3)$$

where the subscript *0* denotes reference state and Φ_c is a non-zero critical porosity where the absolute permeability k becomes zero. The exponent n is reported to range from 2 to 3 but can also be as large as n = 10 or higher, depending on how hydrate grows in the pore space (Moridis and Pruess (2014) and references therein). The next step is to model the relative permeability to water and gas using the dynamic absolute permeability corresponding to the given hydrate saturation. The two-phase flow is then described by a standard relative permeability correlation such as the modified Brooks-Corey curves (Alpak et al., 1999). The equation for the relative permeability to gas becomes:

$$k_{r,g} = k^0_{r,g}\left(\frac{S_g - S_{gr}}{1 - S_{gr} - S_{wr}}\right)^{n_g}, \quad (4)$$

where $k^0_{r,g}$ is end-point relative permeability to gas at residual brine saturation S_{wr}, S_{gr} is residual saturation of gas, and n_g is a fitting parameter controlling the slope of the

curve. Simulation results have shown that n_g increases from 2.6 for $S_H = 0.2$ to 3.5 for $S_H = 0.6$ in hydrate-bearing sediments (Mahabadi et al., 2016).

2.5 CO_2 Sequestration

Carbon capture and storage (CCS) refers to the capture of CO_2 from exhaust gas (or pre-combustion capture) and subsequent transportation and permanent storage of the CO_2. The technology concept is a key factor to limit anthropogenic CO_2 emissions from fossil-fuel power plants and industrial manufacturing facilities such as iron, steel and cement production. In fact, many of the forecasting models of the IPCC cannot limit global warming to below 2°C over the 21st century relative to pre-industrial levels in the absence of CCS (IPCC, 2014). Potential storage sites for the CO_2 include ocean storage, geological storage, and surface mineral carbonation (IPCC, 2005) with geological storage as the most promising option (Bachu, 2015). The geological media considered for CO_2 storage include depleted oil and gas reservoirs, deep saline aquifers, coal beds and salt caverns (Bachu, 2000). Deep saline aquifers provide the largest storage potential with a likely global storage capacity of at least 1000 $GtCO_2$ and possibly as large as 200 000 $GtCO_2$ (IPCC, 2005). The trapping mechanisms of CO_2 in saline aquifers are divided into structural and stratigraphic trapping, residual CO_2 trapping, solubility trapping and mineral trapping (IPCC, 2005). Structural trapping involves the presence of tight sediments around the aquifer that limits the flow of the CO_2 phase. Residual trapping refers to the immobilization of CO_2 in a water-CO_2 two-phase system by interfacial tension interactions. Solubility trapping is the dissolution of CO_2 in liquid water. Water containing dissolved CO_2 is in the order of 1% denser than pure water and the CO_2-saturated water will sink downwards in the formation due to convective mixing (Bachu, 2015). Mineral trapping refers to the slow process, potentially taking thousands of years, of converting CO_2 to stable carbonate minerals through interactions with the rock matrix (IPCC, 2005).

Another form of trapping which can provide additional storage security is the conversion of liquid CO_2 to solid CO_2 hydrates. The shallow subsurface beneath deep water or onshore subpermafrost sediments possess suitable temperatures and pressures for CO_2 hydrate formation. The base of the CO_2 hydrate stability zone reaches a depth

of up to 450 m below the sea floor in Western Europe (Rochelle et al., 2009). The CO_2 is envisioned to migrate into the hydrate stability region where it will react with the *in situ* pore water and form solid CO_2 hydrates that block the pore space for further CO_2 flow (Koide et al., 1995; Koide et al., 1997). The immobilization of CO_2 through CO_2 hydrate formation can be utilized in two different schemes either as a primary or secondary sealing mechanism (Rochelle et al., 2009). Injecting liquid CO_2 into the subsurface just below the CO_2 hydrate stability zone aims to utilize CO_2 hydrate formation as a primary sealing mechanism. The slightly buoyant liquid CO_2 will then migrate upward and quickly precipitate as solid CO_2 hydrates. The potential capacity of CO_2 hydrate storage offshore Japan is estimated to be nearly 199 $GtCO_2$ (Inui and Sato, 2006). Storing supercritical CO_2 in the deep subsurface may also benefit from CO_2 hydrate formation as a secondary sealing mechanism if the CO_2 unintentionally starts leaking. This may happen along unidentified faults creating transport routes from the storage aquifer and upwards through the stratigraphic seal. The leaking CO_2 will eventually reach the hydrate stability zone where CO_2 hydrate formation provides a backup safety factor (Rochelle et al., 2009). The former mechanism is especially interesting as it enables sequestration of liquid CO_2 in the shallow subsurface in aquifers without any stratigraphic or structural seals (Teng and Zhang, 2018). Liquid CO_2 storage, in contrast to supercritical CO_2 storage, benefits from increased storage capacity due to high-density CO_2, decreased CO_2 mobility due to high density and high viscosity of the CO_2, and increased solubility of CO_2 in liquid water at low temperatures. However, the solubility is also controlled by salinity, pressure, and pH and will therefore depend on local conditions (Rochelle et al., 2009).

3. Results and Discussion

The following chapters summarize the main results of this experimental study. The results include a thorough description of CH_4 hydrate growth and dissociation in porous media, CO_2 hydrate growth and sealing properties in porous media, and permeability measurements of CH_4- and CO_2 hydrate-saturated porous media. The characterization of the different process phenomena is aided by micrometer-scale observations in a micromodel chip and centimeter-scale measurements in rock core plugs by magnetic resonance imaging (MRI). The imaging techniques are used complementary to understand sedimentary hydrate dynamics across length scales ranging from pore- to core-scale. The key components of the experimental procedure are intertwined with the presentation of the results in the following chapters. The reader is referred to **paper 1-7** enclosed in this dissertation for specifics about the experimental systems and procedures.

3.1 Gas Hydrate Growth in Sediments

The hydrate growth process occurring over geological time in nature is difficult to replicate in the laboratory over the course of a few weeks. Formation of hydrates in nature is believed dominated by nucleation of dissolved CH_4 in the pore water (Collett et al., 2009), whereas in the laboratory hydrates form more easily at the interface between liquid water and gaseous CH_4. The first part of the results section is devoted to unravelling how the final hydrate distribution is affected by the initial fluid (water and CH_4) saturation prior to hydrate formation. The final hydrate distribution is a key component in analyzing the subsequent hydrate dissociation and CH_4 gas production.

3.1.1 Effect of Initial Fluid Saturation

The effect of initial water saturation was investigated in a dual water-saturated composite core in **paper 1**. One Bentheim sandstone core with low water saturation was stacked together with another Bentheim core with high water saturation and visualized by MRI. Two runs with different initial water distribution were performed in which hydrate was formed at constant pressure 8.30 MPa and constant temperature ~3°C in both of them (**Fig. 3**). Most of the hydrate formed in the high water saturation

region and the final hydrate distribution mirrored the initial water distribution (**Fig. 4**). The magnitude of hydrate formation was clearly dependent on local availability of water. In fact, the growth of hydrate started and continued in the high water saturation region until the water saturation dropped to a similar value as in the low water saturation region. Further limited hydrate growth continued slowly in the entire core until the water saturation stabilized around 0.1 (frac.). T_2 distribution curves were also measured during the growth sequence. The area under the T_2 distribution curve is a measure of the water saturation and the average T_2 is indicative of the water distribution at pore-scale, where shorter T_2 values suggest water present close to mineral grains (Kleinberg et al., 2003). Different responses were observed in the high- and low water saturation regions: The area under the T_2 distribution curve (**Fig. 5**) and the average T_2 (**Fig. 6**) decreased significantly during hydrate growth in the high water saturation region. In the low water saturation region, the area decreased similarly but the average T_2 remained unchanged at the same value as the final average T_2 in the high water saturation region. The amount and pore-scale distribution of remaining water were likely the same after hydrate formation in regions with both high and low initial water saturation. The main difference in final fluid saturation between the regions was the amount of hydrate which was occupying the center of pores at the expense of CH_4 gas.

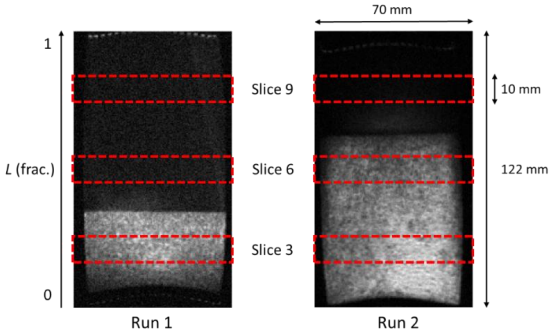

Figure 3. Sagittal view of the initial water saturation in the composite core. Run 1 (left) started with a short water-filled core stacked together with a long air-filled core. Run 2 (right) started with the opposite saturation in the cores. The red dashed rectangles mark the position of the three axial slices that are used to visualize hydrate growth. From **paper 1**.

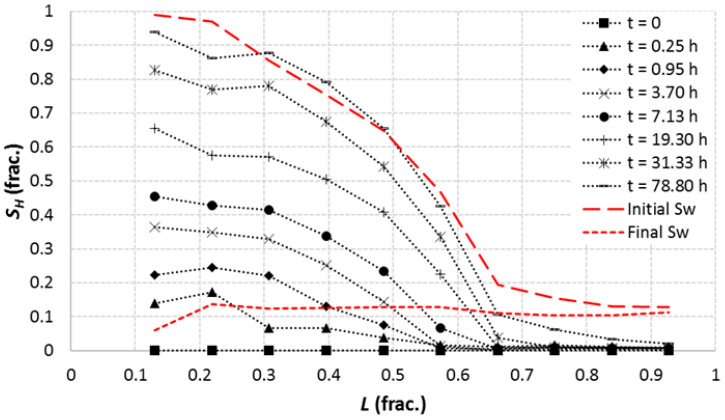

Figure 4. Methane hydrate saturation profiles during hydrate growth in Run 2. The pressure and temperature were kept constant at 8.30 MPa and ~3°C, respectively. From **paper 1**.

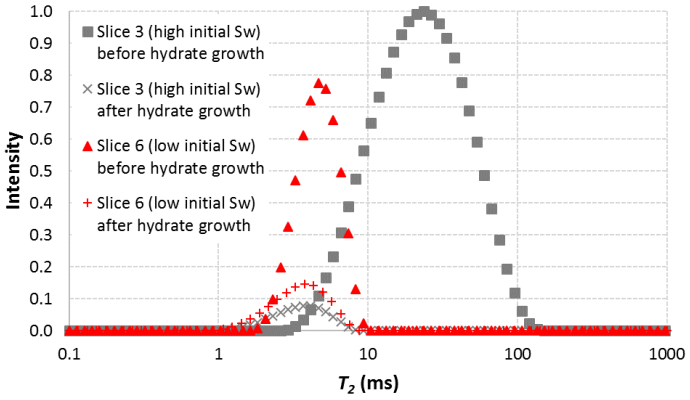

Figure 5. Distribution of transverse relaxation time constant, T_2, in two different cross-sections of the core in Run 1. In slice 3 (high initial S_w), the intensity of the distribution decreases and shifts leftwards as hydrate grows. The intensity of the distribution in slice 6 (low initial S_w) decreases as hydrate grows, but the average T_2 remains constant. From **paper 1**.

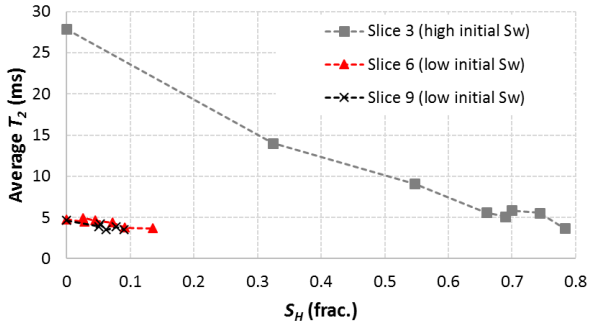

Figure 6. Average T_2 in three different cross-sections of the core during hydrate growth in Run 1. From **paper 1**.

Additional knowledge about the effect of initial fluid saturation on hydrate formation characteristics was obtained by explicit pore-scale imaging in a transparent micromodel chip in **paper 2**. The chip was an authentic replicate of actual sandstone pore geometry except from the pore height, which was constant equal to 25 μm. Hydrate formation in individual pores saturated with different amounts of water and CH_4 gas showed that the growth of hydrate always started at the water-gas interface. Continued growth resulted in two different final distributions of hydrate (**Fig. 7**): A) A porous hydrate with encapsulated CH_4 gas surrounded by a shell of CH_4 hydrate or B) a solid nonporous hydrate with all the CH_4 gas consumed during growth. The final hydrate morphology was mainly governed by local availability of water and mass transfer of water across the hydrate layer at the gas-water interface. In pore-clusters where the CH_4 gas saturation was high, all the visible water converted to hydrate and the formation process ceased before all the CH_4 gas was consumed. Small isolated gas bubbles spanning only a couple of pore bodies were on the contrary fully consumed and yielded nonporous hydrate. The latter hydrate morphology was also the result when hydrate formed from dissolved CH_4 in liquid water. These observations are in line with the findings from **paper 1** where the average T_2 became the same after hydrate formation independent of the initial fluid saturation. The remaining water after hydrate formation was always located adjacent to the water-wet rock grains with the porous or nonporous hydrate residing in the middle of pores.

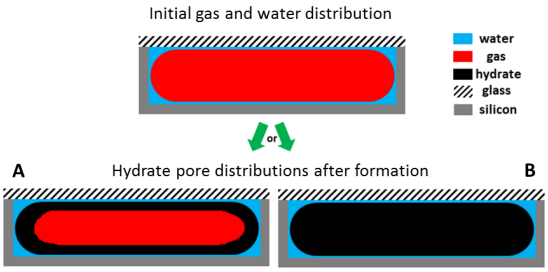

Figure 7. Conceptual model (not to scale) of pore-level hydrate growth. Each image represents a cross-section of an average pore with diameter 100 µm. The pore is initially filled with a CH_4 gas bubble surrounded by a water film coating the water-wet solid boundaries. Hydrate growth follows the water-gas interface until the gas phase is either encapsulated by a porous hydrate (A) or consumed and a nonporous hydrate is formed (B). Modified from **paper 2**.

3.2 Gas Hydrate Dissociation in Sediments

The scope of the following chapter is to evaluate the production response of CH_4 gas from CH_4 gas hydrates. The rate of CH_4 gas recovery is analyzed with respect to the initial hydrate saturation and distribution, production pressure, and salinity of the pore water.

3.2.1 Effect of Hydrate Saturation

A series of core-scale experiments were conducted in **paper 3** to investigate the effect of hydrate saturation on CH_4 production rates, aiming to identify the saturation region at which the maximum rate of CH_4 recovery occurred. The CH_4 hydrate saturation ranged between 0.19 to 0.88 (frac.) in the different Bentheim sandstone core plugs, and the CH_4 hydrate was dissociated at a specific constant production pressure in each core plug at constant system temperature of 4.0°C. The pressure driving force was calculated for each core plug as the difference between the theoretical hydrate dissociation pressure and the production pressure at the time of maximum CH_4 recovery. The maximum rate of CH_4 recovery, i.e. the maximum amount of CH_4 gas produced from hydrate per time, was significantly depending on the hydrate saturation in the core plug prior to dissociation (**Fig. 8**). The maximum rate was largest in the hydrate saturation interval of 0.30 to 0.50 (frac.) with diminishing maximum rates at lower and higher hydrate saturations. A very low hydrate saturation of less than 0.30

(frac.) could not sustain a large maximum rate because of the limited amount of CH_4 gas that was present in the hydrate. A high hydrate saturation of more than 0.50 (frac.) contained plenty of CH_4 gas that could fuel a large maximum rate of CH_4 recovery. Still, the maximum rate decreased with increasing hydrate saturation for $S_H > 0.50$ (frac.). The dissociation rate was low when the volume-to-surface ratio of the hydrate was high because of limited mass transport of liberated CH_4 gas, which again affected the effective heat transfer in the porous medium.

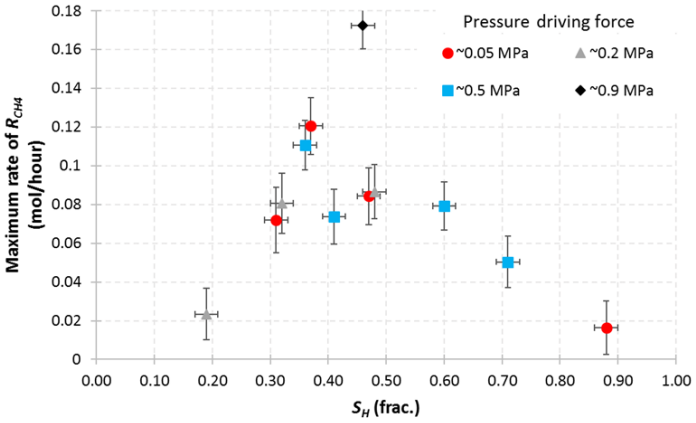

Figure 8. Maximum rate of CH_4 gas recovery (R_{CH4}) as a function of initial hydrate saturation for four different pressure driving forces (legend). The pressure driving force is the difference between the theoretical hydrate dissociation pressure and production pressure at the time of maximum recovery. The maximum production rate (mol/hour) is highest at a hydrate saturation of 0.30 – 0.50 (frac.) and seems independent of pressure driving force. From **paper 3**.

Direct visual confirmation of the effect of hydrate saturation was obtained through pressure-induced dissociation of CH_4 hydrate in the micromodel. Two different hydrate saturations and distributions were subsequently established in the micromodel prior to the dissociation, with reference to Fig. 7. In the first experiment, the pore space was saturated with approximately 0.2 (frac.) porous CH_4 hydrate in co-occurrence with liquid water and gaseous CH_4 (**Fig. 9**). The CH_4 hydrate was mainly distributed as a hydrate shell around the gas phase separating the gas from the grain-coating water. Setting the production pressure to 2.40 MPa resulted in complete hydrate dissociation in about 10 minutes. The hydrate shell in the field of view (Fig. 9) dissociated

immediately when the gas inside the hydrate shell was able to flow down-stream. The high gas saturation ensured high relative permeability to gas which facilitated rapid gas transport away from the dissociation reaction. In the other experiment, the pores were filled with nearly 100% nonporous CH_4 hydrate along with trace amounts of CH_4-saturated water (**Fig. 10**). The absence of a separate gas phase prior to dissociation affected the recovery rate of CH_4 gas significantly. Setting the production pressure to 2.50 MPa led to minor dissociation over the course of five hours, and the production pressure was further reduced down to atmospheric pressure. Still, the dissociation resumed slowly and 30 minutes were needed to dissociate just a small part of the pore space (Fig. 10). The nonporous hydrate filling the pores obstructed the pressure reduction from transmitting through the pore space and hydrate had to dissociate in one pore before the pressure reduction was transmitted to the next pore. The liberated gas was initially capillary trapped before reaching a critical saturation at which point the gas could flow down-stream. The low tortuosity of the pore network hindered an effective escape of the CH_4 gas and limited the heat transfer stemming from forced convection. Based on these observations, a conceptual model of pressure-induced hydrate dissociation was developed in **paper 2** (**Fig. 11**). Depressurization of porous hydrate (A^P) benefits from effective pressure transmission and rapid gas flow away from the dissociation reaction. Depressurization of nonporous hydrate (B^P) suffers from low mobility of the liberated gas during initial dissociation. The pressure transmission is slow at elevated hydrate saturation and the nonporous hydrate obstructs interaction between neighboring pores. This explains the decreasing rate of CH_4 gas recovery with increasing hydrate saturation observed in **paper 3**.

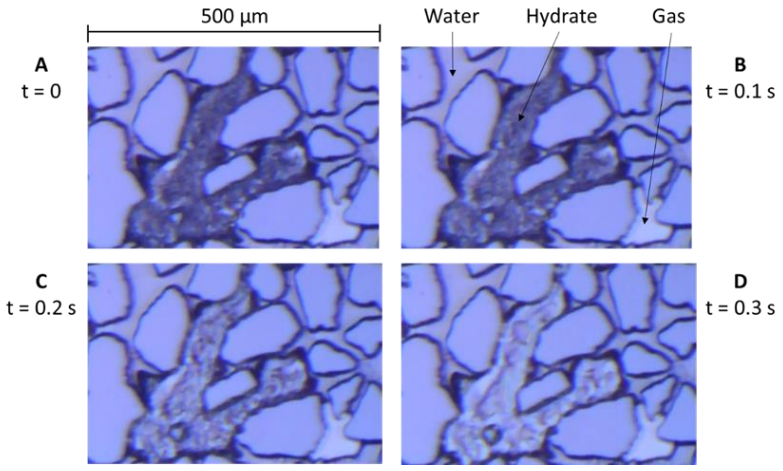

Figure 9. CH_4 hydrate dissociation at $T = 1.3$°C and $P = 2.40$ MPa. When the hydrate in field of view first started to dissociate (A), complete dissociation was finished within less than a second (B-D). From **paper 3**.

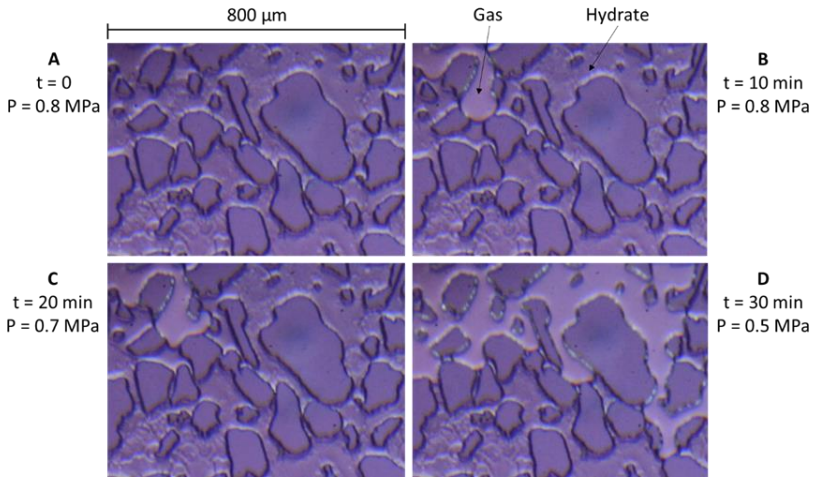

Figure 10. CH_4 hydrate dissociation during depressurization (A-D) at $T = 1.3$°C. The dissociation was slow and the production continued for nine hours before all hydrate dissociated. From **paper 3**.

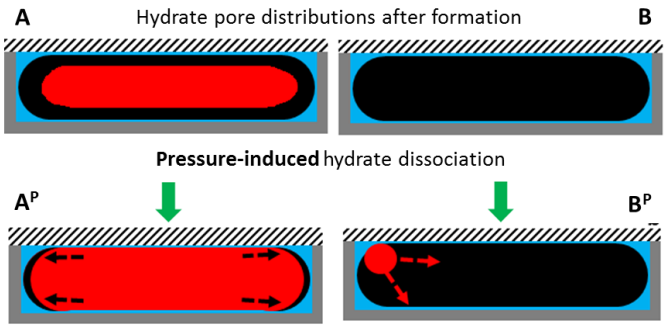

Figure 11. Conceptual model (not to scale) of pore-level hydrate dissociation by pressure depletion. Each image represents a cross-section of an average pore with diameter 100 µm. A^P: Dissociation of hydrate-encapsulated gas by pressure depletion starts in the middle of pores (seen from above) where the hydrate layer is thinnest. The dissociation pattern follows a reverse growth evolution. B^P: Dissociation of nonporous hydrate surrounded by a water film by pressure depletion starts in the pore corners since the pressure reduction propagates through the liquid water phase accumulated in the corners. The gas bubble expands as hydrate dissociation continues. Modified from **paper 2**.

3.2.2 Effect of Production Pressure

A range of different production pressures were used in the core experiments in **paper 3** to investigate the effect on CH_4 gas recovery rate. Despite having limited effect on the maximum rate of recovery (Fig. 8), the production pressure was the governing factor on the total CH_4 recovery time (**Fig. 12**). The average pressure driving force is the arithmetic average of the dynamic pressure driving force experienced from start to end of the hydrate dissociation. Although the production pressure was kept constant in each experiment, the pressure driving force changed dynamically because of temperature changes resulting from endothermic dissociation and salinity changes resulting from pore water freshening. The ultimate CH_4 recovery time decreased as the average pressure driving force increased (Fig. 12). The initial hydrate saturation also affected the total recovery time, as observed in Fig. 9-10, but for similar hydrate saturations, the effect of production pressure was clear. The initial production rate of CH_4 gas is thus expected to be governed by the hydrate saturation and distribution, and then the magnitude of the production pressure contributes increasingly to the recovery rate as dissociation evolves.

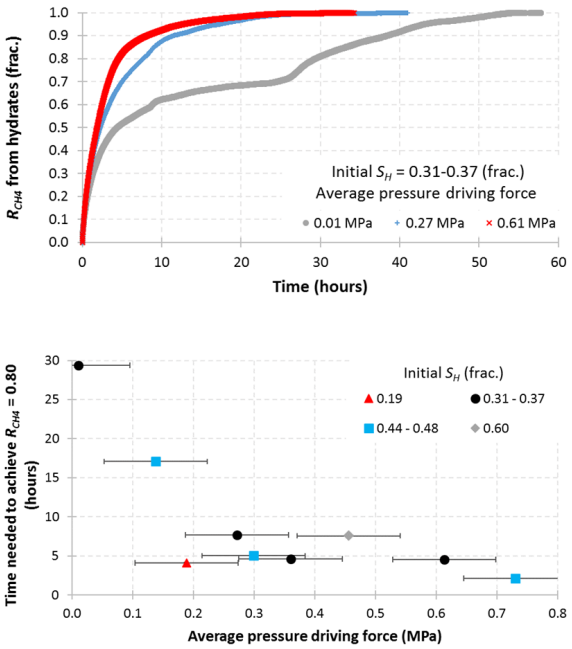

Figure 12. Recovery of CH_4 gas from CH_4 hydrate dissociation (R_{CH4}) as a function of pressure driving force. Top: Normalized CH_4 gas recovery from hydrates as a function of time for three different average pressure driving forces (initial hydrate saturation ranges between S_H = 0.31 – 0.37 for the three experiments). The total recovery time decreases with increasing pressure driving force. Bottom: The time (hours) needed to produce 80% of available CH_4 gas from hydrates decreases with increasing average pressure driving force. From **paper 3**.

3.2.3 Effect of Pore Water Salinity

A stepwise pressure reduction scheme was implemented in the micromodel experiments to investigate the effect of pore water salinity on the dissociation behavior. In a series of tests, hydrate was formed from CH_4 gas and pore water containing 2.0, 3.5 or 5.0 wt% NaCl. The salinity of the pore water increased during hydrate growth as the salt ions were excluded from the hydrate structure. The increased salinity resulted in a shift in the hydrate phase behavior and the hydrate dissociation started at elevated pressure. For instance, hydrate formed from 5.0 wt% NaCl pore water started to dissociate at a pressure corresponding to pore water containing 5.6 wt% NaCl (**Fig. 13A**). The start of hydrate dissociation was determined by visual observation of hydrate

phase changes and the measured pressure and temperature at that time were linked to pore water salinity through the CSMGem software (CSMGem, 2015). More than half of the CH_4 hydrate dissociated at this pressure (Fig. 13A). After the pressure was kept constant for one hour without any further hydrate dissociation, the pressure was reduced by 0.07 MPa and another fraction of the hydrate dissociated. This stepwise pressure reduction of 0.07 MPa continued until the last fraction of the hydrate dissociated at a pressure of 4.14 MPa, corresponding to a pore water salinity of 1.8 wt% NaCl (CSMGem, 2015). The hydrate that dissociated at the final pressure step was located in the middle of pores surrounded by CH_4 gas (Fig. 13B). The hydrate dissociation with distilled water was on the contrary promoted when the hydrate was surrounded by CH_4 gas compared to water. The delayed hydrate dissociation observed for saline pore water is believed to originate from pore water freshening. The freshwater that was liberated by initial dissociation of hydrate surrounded by gas, accumulated at the adjacent grain surface as a thin water film (Fig. 13B). Salt ions from water located in neighboring pores did not diffuse into the freshwater film during the timespan of the experiment. The hydrate was thus temporarily stabilized by the freshwater film and a lower pressure had to be implemented to drive dissociation forward.

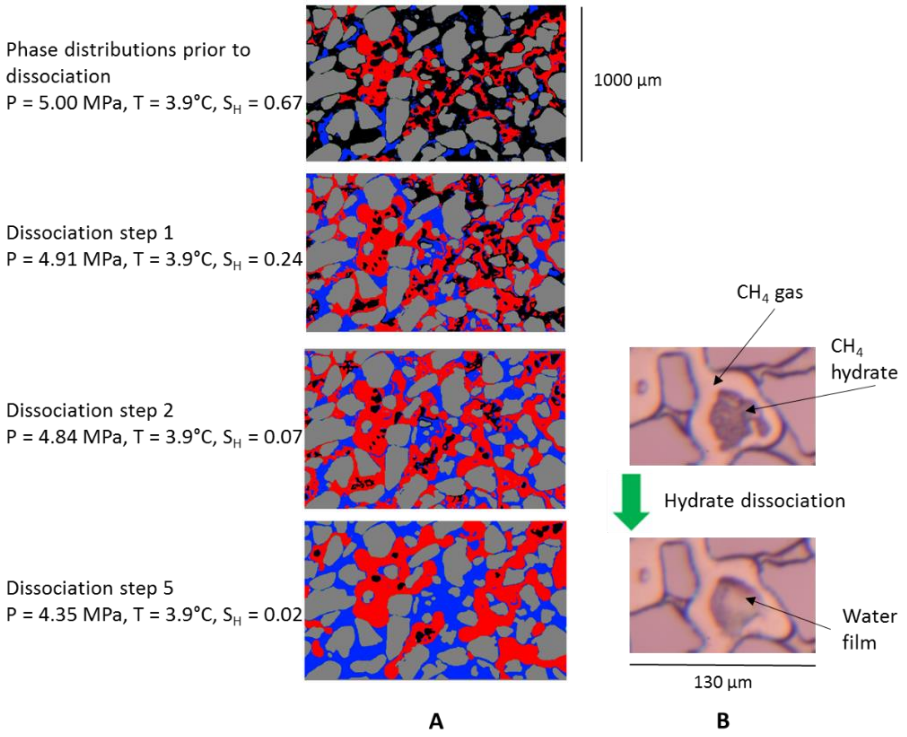

Figure 13. A: Some of the pressure steps needed to dissociate CH_4 hydrate by decreasing the pressure in decrements of 0.07 MPa at 3.9°C. Silicon grains are colored grey, CH_4 gas is red, brine is blue and CH_4 hydrate is black. The initial brine salinity prior to hydrate formation was 5.0 wt% NaCl. The final hydrate saturation after ~24 hours of hydrate growth was 0.67, and both gaseous CH_4 (red) and liquid water (blue) were present in the pore space. Initial dissociation started when the pressure was lowered to 4.91 MPa, corresponding to a brine salinity of 5.6 wt% NaCl (CSMGem, 2015). The dissociation of hydrates continued for 26 min and the hydrate saturation reached 0.24. No further changes in saturation were observed the next hour. The pressure was then reduced to 4.84 MPa and the dissociation process recommenced until the hydrate saturation was reduced to 0.07. The system was again held at constant pressure for one hour without further phase changes. Reducing the pressure 0.07 MPa at the time led to small hydrate saturation reductions at each pressure step. When the pressure was lowered to 4.35 MPa, the hydrate saturation had contracted to 0.02. All the hydrate dissociated with a pore pressure of 4.14 MPa. B: Unsegmented images of dissociation of pore-center surface-hydrate surrounded by CH_4 gas. The liberated water coated the grain surface as a film with reduced ion content compared to mobile water in adjacent pores. The water film thickness decreased as the water drained laterally and the salinity of the film increased slowly as salt ions diffused from surrounding brine. Modified from **paper 2**.

3.3 Permeability of Sedimentary Gas Hydrates

The results of the dissociation experiments highlighted the importance of the hydrate saturation on the rate of CH_4 gas recovery during depressurization. The coupling between CO_2 hydrate saturation and CO_2 flow rates are also paramount when considering the applicability of CO_2 hydrate sealing in saline aquifers. In both cases, there is a need to identify the CH_4 (or CO_2) saturation at which the fluids become immobile. This was the aim of the work presented in **paper 4** and is summarized in the following sections.

3.3.1 CH_4 Hydrates Permeability

Effective permeability to CH_4 gas was measured in Bentheim sandstone cores with CH_4 hydrate saturations ranging between 0.29 and 0.61 and CH_4 gas saturations ranging between 0.18 and 0.60. The remaining water saturation after hydrate formation was considered immobile during flow of CH_4 gas. The permeability to CH_4 gas when hydrate was present in the pore space (three phases) was compared to the permeability to CH_4 gas without hydrates (two phases). The three-phase permeability values were consistently lower than the two-phase permeability values for all gas saturations (**Fig. 14**). The presence of solid hydrates in the pores reduced the CH_4 gas permeability even for constant saturation of CH_4 gas. A transition zone in the CH_4 gas saturation equal to 0.33 - 0.38 (frac.) was identified where the permeability to CH_4 gas dropped from mD- to μD-values. Scaled fluid saturations were also calculated based on treating hydrate as part of the solid grains. The reduction in absolute permeability inflicted by the effective porosity reduction was calculated by **eq. 3**. The resulting relative permeability to CH_4 gas relation (**Fig. 15**) was fitted with a modified Brooks-Corey curve (**eq. 4**). The scatter in permeability values for similar CH_4 gas saturations were attributed to heterogeneities in the initial water distribution, which gave heterogeneous final hydrate distributions in some of the experiments.

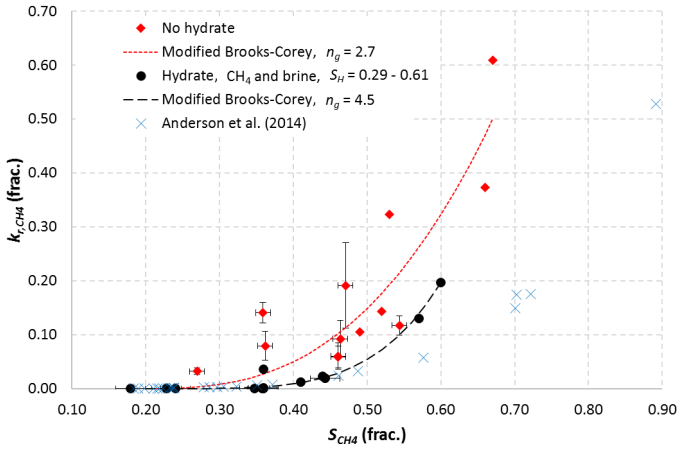

Figure 14. Relative permeability values for CH_4 gas as a function of CH_4 gas saturation. Two-phase permeability (diamonds) was obtained on individual cores at room temperature and $P = 8.30$ MPa prior to hydrate formation. Three-phase permeability (circles) was measured on the same cores at 4.0°C after hydrate formation. The CH_4 hydrate saturation varied from 0.29 to 0.61 in the different cores. The permeability values were fitted with modified Brooks-Corey curves based on least squares regression. One data set from Anderson et al. (2014) was included for comparison. Error bars reflect instrumental uncertainties. From **paper 4**.

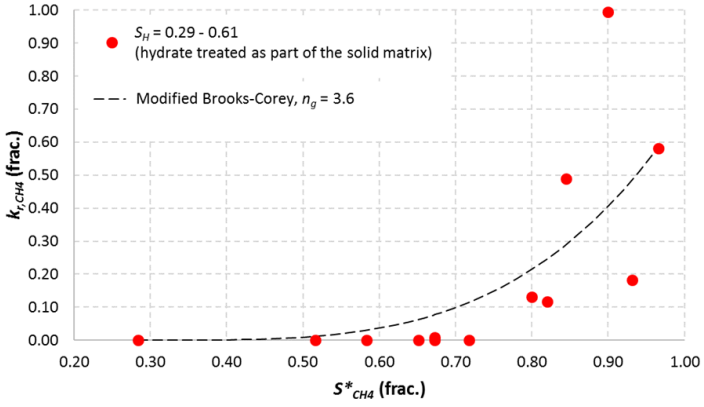

Figure 15. Relative permeability to CH_4 gas when hydrate is treated as part of the solid rock. The saturation of CH_4 (and brine) is scaled according to the reduction in porosity and the absolute permeability is scaled according to Eq. 3 with a fitting parameter $n = 1.7$. The permeability values were fitted with a modified Brooks-Corey curve based on least squares regression. From **paper 4**.

3.3.2 CO_2 Hydrates Permeability

The CO_2 hydrate saturation ranged between 0.18 and 0.32 (frac.) and the CO_2 liquid saturation ranged between 0.37 – 0.70 (frac.) in the different Bentheim sandstone cores. The relative permeability to CO_2 was consistently lower for the three-phase system than for the two-phase system for similar CO_2 saturations (**Fig. 16**). The effective permeability to CO_2 was unmeasurable at a CO_2 saturation of 0.37 (frac.) when the CO_2 hydrate saturation was 0.30 (frac.). In comparison, the relative permeability to CO_2 was 0.034 (frac.) at the same CO_2 saturation and no hydrates present. Scaled relative permeability values were calculated based on the effective reduction in absolute permeability (eq. 3) and fitted with modified Brooks-Corey curves (**Fig. 17**).

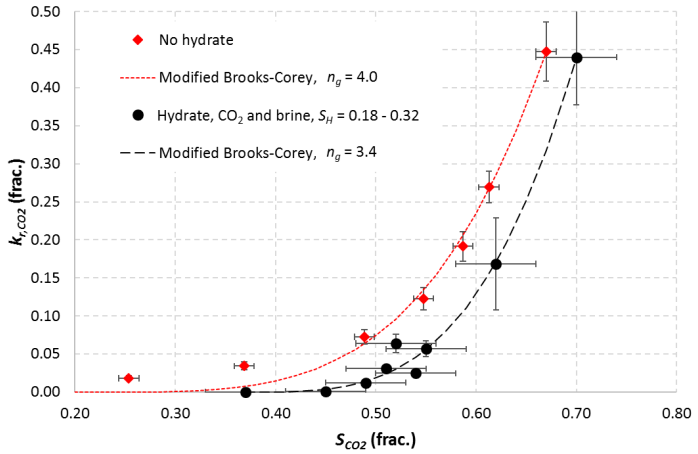

Figure 16. Relative permeability values for liquid CO_2 as a function of liquid CO_2 saturation. Two-phase permeability (diamonds) was obtained by draining brine at different flow rates in a single core at room temperature and P = 7.00 MPa. Three-phase permeability values (circles) represent individual cores where the hydrate saturation ranged from 0.18 to 0.32 (frac.) and the temperature was 4.0°C. The permeability values were fitted with modified Brooks-Corey curves based on least squares regression. Error bars reflect instrumental uncertainties. Modified from **paper 4**.

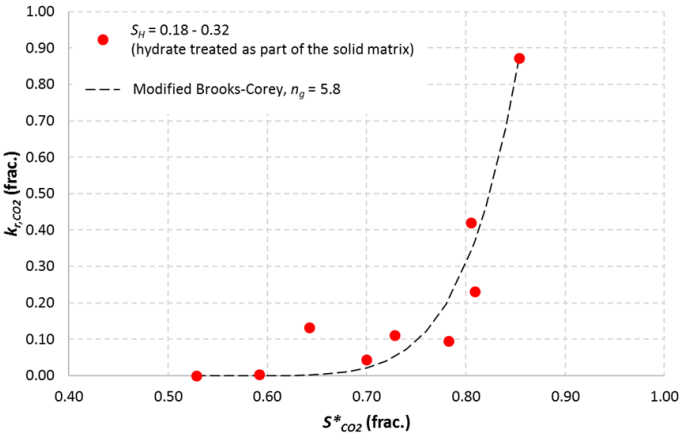

Figure 17. Relative permeability to liquid CO_2 when hydrate is treated as part of the rock. The saturation of CO_2 (and brine) is scaled according to the reduction in porosity and the absolute permeability is scaled according to Eq. 3 with a fitting parameter $n = 2.3$. The permeability values were fitted with a modified Brooks-Corey curve based on least squares regression. From **paper 4**.

3.3.3 Permeability Discussion

The addition of solid hydrates in the pore space reduced the effective permeability to both CH_4 and CO_2 at constant CH_4 (or CO_2) saturation. The blockage of fluid flow provided by the combination of brine and hydrate was greater than the blockage exerted by brine alone. In the two-phase case, the CH_4 (or CO_2) flowed in the middle of the pores with brine residing next to the water-wet grain surface. In the three-phase case, when hydrate was present, some of the CH_4 (or CO_2) was encapsulated and immobilized by the formed porous hydrate, ref. **paper 2**. A higher degree of the gaseous CH_4 (or liquid CO_2) present in the pores did not contribute to the CH_4 (or CO_2) flow in the three-phase system compared to the two-phase system. The fitting exponent, n in the modified Brooks-Corey curve increased during hydrate growth for both CH_4 and CO_2. It increased from 2.7 to 3.6 when CH_4 hydrates formed in the pores and from 4.0 to 5.8 when CO_2 hydrates formed. The increase in the slope of the relative permeability function was due to precipitation of solid hydrates in the pore space which altered the tortuosity of the rock and effectively transformed the rock into a new porous medium. Simulation results showed a similar continuous increase in n with increasing hydrate saturation (Mahabadi et al., 2016). This implies that a unique Brooks-Corey

curve should be used for every hydrate saturation in a given rock sample. During hydrate dissociation when the hydrate saturation changes continuously, a set of relative permeability correlations should be used to map the flow of gas and water. The increase in *n* with increasing hydrate saturation demonstrated that the relative permeability to gas is more sensitive to changes in the gas saturation when the hydrate saturation is high. The difference in relative permeability between the two-phase system and the three-phase system was also evident by plotting the permeability ratio as a function of fluid saturation (**Fig. 18**). The permeability ratio is defined as the relative permeability to CH_4 (or CO_2) when hydrate is present (three phases) divided by the relative permeability to CH_4 (or CO_2) without hydrate present (two phases) for equal CH_4 (or CO_2) saturation in each ratio. The value of the permeability ratio increased linearly with increasing CH_4 (or CO_2) saturation, indicating a limit at $S_{CH4\ (or\ CO2)} \sim 0.80$ (frac.) where the relative permeability of the three-phase system equaled the relative permeability of the two-phase system. The effective permeability to CH_4 (or CO_2) was more sensitive to inclusion of hydrates in the pores at low CH_4 (or CO_2) saturations, most likely because the limited CH_4 (or CO_2) phase was more prone to become disconnected and capillary immobilized.

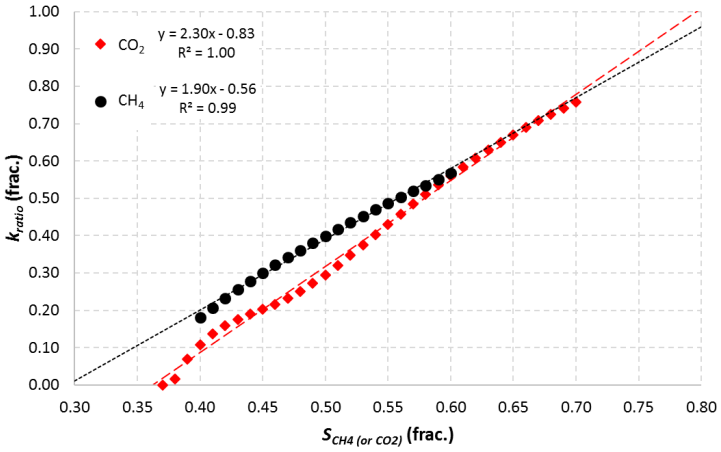

Figure 18. Permeability ratios for CH_4 gas (circles) and liquid CO_2 (diamonds) as a function of CH_4 (or CO_2) saturation. The permeability ratio is here defined as the relative permeability to CH_4 (or CO_2) when hydrate is present (three phases) divided by the relative permeability to CH_4 (or CO_2) without hydrate present (two phases), for equal CH_4 (or CO_2) saturation in each ratio. The hydrate saturation ranged between 0.18 and 0.32 for the CO_2 measurements and 0.29 and 0.56 for the CH_4 measurements in this figure. From **paper 4**.

3.4 CO_2 Hydrate Storage and Sealing

The screening of CO_2 permeability in hydrate-saturated porous media demonstrated the feasibility of using CO_2 hydrates as seal during geological CO_2 storage. The effective permeability to liquid CO_2 dropped to zero at a CO_2 saturation of around 0.40 (frac.) in **paper 4**. The next step in assessing the potential of CO_2 hydrate sealing was to evaluate the growth pattern of CO_2 hydrate in water-filled pores.

3.4.1 CO_2 Hydrate Growth

The same multiscale approach was used to characterize the growth habit of CO_2 hydrates in **paper 5** as was used to map the growth of CH_4 hydrates. The CO_2 hydrate growth was initiated by injecting liquid CO_2 into water-filled porous media at a pore pressure of 7.00 MPa and a temperature of 1-2°C. Direct visual observation of CO_2 injection in a micromodel revealed that the CO_2 hydrate formed within minutes after

the liquid CO_2 displaced some of the unsaturated distilled water (**Fig. 19**). Initial CO_2 hydrate formed at the interface between liquid CO_2 and liquid water, similar to the CH_4 hydrate nucleation at the interface between CH_4 gas and liquid water. The CO_2 hydrate growth was then temporarily halted and CO_2 injection was sustained for another 14 minutes without loss of injectivity. An abrupt hydrate crystallization of the water phase followed and the injectivity dropped to zero. The CO_2 hydrate formed simultaneously in the entire water phase within the field of view; no front-movement was observed. Additional hydrate growth continued into the stationary CO_2 phase until the growth ceased because of lack of water supply. The pore space was ultimately left with pore-filling liquid CO_2 that was completely immobilized by surrounding CO_2 hydrates. The same immobilization was observed at a larger scale when liquid CO_2 was injected in a water-filled Bentheim sandstone core plug. The water saturation was explicitly mapped by MR imaging during CO_2 injection and subsequent CO_2 hydrate growth (**Fig. 20**). A total of 0.27 PV (frac.) of water were displaced by injecting 0.97 PV (frac.) of liquid CO_2 before the injectivity was hampered by CO_2 hydrate growth. Continued CO_2 injection led to buildup of the injection pressure and the injection was stopped when the differential pressure reached 1.0 MPa across the core. The CO_2 hydrate saturation leveled off at 0.49 (frac.) after 24 hours of formation. The combined stored amount of CO_2 as liquid and hydrate was equivalent to 0.34 PV (frac.) of liquid CO_2, an increase of 0.07 PV (frac.) compared to the stored amount of liquid CO_2 after drainage only. No water nor CO_2 were produced during this period. The results demonstrated the effective flow restriction offered by CO_2 hydrate formation along with the increased storage capacity of CO_2.

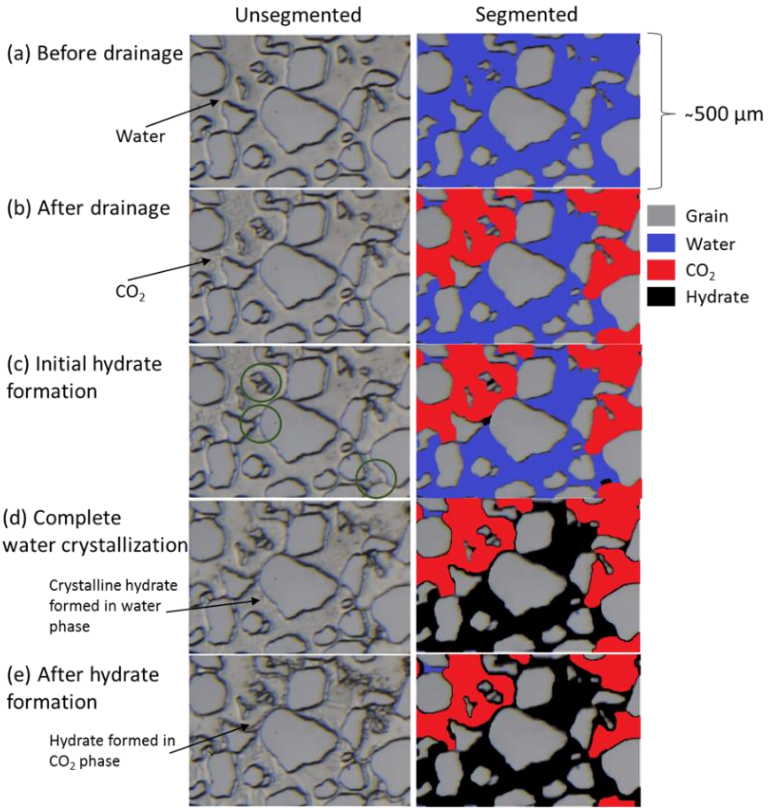

Figure 19. Pore-scale visualization of CO_2 hydrate growth during liquid CO_2 injection into a water-filled micromodel sandstone analog. The initial pressure was 7.00 MPa and the temperature was equal to 1.3°C. Segmented images are added for clarity. CO_2 drained approximately 50% of the pore space in the field of view (b) which originally was filled with water (a). Hydrate started forming at the CO_2-water interface after ~2 minutes of injection (c). Nonporous hydrate formed in the water phase after ~14 minutes and the injectivity dropped to zero (d). The hydrate growth advanced toward the liquid CO_2 phase but ceased after ~40 minutes (e). From **paper 5**.

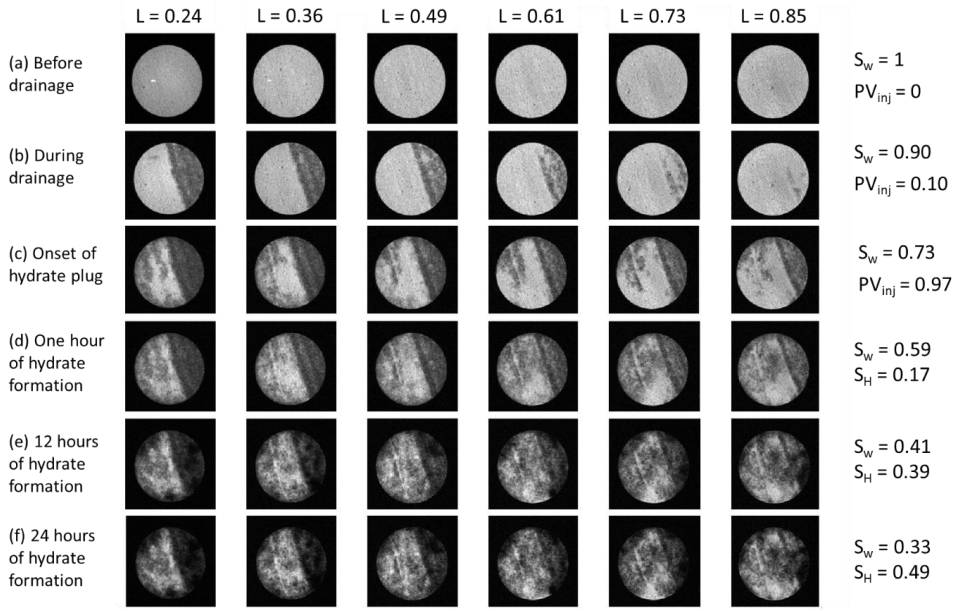

Figure 20. Core-scale visualization of CO_2 hydrate growth during liquid CO_2 injection into a water-filled Bentheim sandstone core plug. Signal intensity (grey scale) relates to water saturation. Saturation values (right) reflect global fluid phase saturations in the entire core based on PVT data, where S_w denotes water saturation and S_H denotes hydrate saturation. The initial pressure was 7.00 MPa and the temperature was approximately 2°C. The drainage of water by CO_2 was highly heterogeneous (b) and led to a water saturation of 0.73 (frac.) after injecting 0.97 PV (frac.) of CO_2 (c). The hydrate plug initiated in the outlet end-piece (not shown) and eliminated the production of CO_2 and water. Continued hydrate growth throughout the pore network (d-f) resulted in a final hydrate saturation of 0.49 (frac.). From **paper 5**.

3.4.2 Effect of Porous Media

A series of long-term experiments were conducted in **paper 6 and 7** to investigate the effect of porous media on the sealing capability of CO_2 hydrates. The rock material ranged from high permeability sandstone to low permeability limestone with specifics of each material detailed in **Table 1**. The pore pressure and temperature were kept constant to 7.00 MPa and 4.0°C, respectively, in each experiment, except from the tight reservoir rock from Svalbard where the pore pressure was 2.00 MPa and the temperature was 0.1°C. Initial hydrate formation occurred after approximately 0.2 PV

(frac.) of CO_2 injected for every core material (**Fig. 21**). The pore space was initially not completely blocked and the differential pressure fluctuated as the CO_2 injection continued. The amount of CO_2 that was injected before complete blockage of the pore space varied significantly in the different core materials. The volume of injected CO_2 before complete plugging of the pore space was 0.4 PV (frac.) in the Svalbard core, 0.5 PV (frac.) in the unconsolidated silica sand, 1.4 PV (frac.) in the Bentheim sandstone, and 7.0 PV (frac.) in the Edwards limestone (Fig. 21). The time delay from initial hydrate formation until complete plugging stemmed from the CO_2 hydrate growth process described in **paper 5**: The initial CO_2 hydrate formation at the CO_2-water interface obstructed the flow of CO_2 incompletely. Some hydrate films formed and others broke during the start of hydrate formation. The flow of CO_2 was fully halted when the water phase crystallized into massive hydrates that encapsulated and immobilized the CO_2 phase. The time needed to obtain full blockage of the pore space varied according to mineralogy, porosity and permeability. For the quartz-dominated core materials, the injected amount of CO_2 before complete blockage increased with increasing absolute permeability. CO_2 hydrate sealing is thus expected to be faster in tight sandstone rocks compared to high permeability sandstone. Narrow pore throats in tight rocks are more easily obstructed by thin hydrate films forming early in the nucleation process. The absolute permeability of the silica sand pack was measured to 360 mD which is lower than the typical permeability of unconsolidated sand. The low permeability was probably caused by clogging of the sand filters that were used on each end of the sand pack. The rapid CO_2 hydrate sealing observed in the sand pack was then a consequence of CO_2 hydrate formation in or near the sand filters. The limestone core did not fit into the same permeability relation as the sandstone material. In fact, the limestone core had the largest throughput of CO_2 before the core was fully sealed. More experiments should be conducted in order to formulate any conclusive effect of the mineralogy. However, the limestone, consisting of predominantly calcite, is prone to dissolution by the carbonic acid formed by CO_2 in contact with water. The initial acidification of the pore water may affect the growth pattern of CO_2 hydrate and thereby the time needed to seal of the core plug.

Table 1. Core material used in the CO_2 hydrate sealing experiments. *Approximate average permeability of Bentheim sandstone.

	Edwards limestone	Silica sand pack	Bentheim sandstone	Svalbard sandstone
Porosity (frac.)	0.25	0.40	0.22	0.06
Permeability (mD)	80	360	1500*	0.04
Brine composition	3.5 wt% ($CaCl_2$ and NaCl)	3.5 wt% (NaCl)	3.5 wt% (NaCl)	1.0 wt% (NaCl)
Pore pressure (MPa)	7.00	7.00	7.00	2.00
Pore temperature (°C)	4.0	4.0	4.0	0.1
CO_2 injection rate (mL/min)	0.05	0.5	0.005	0.1

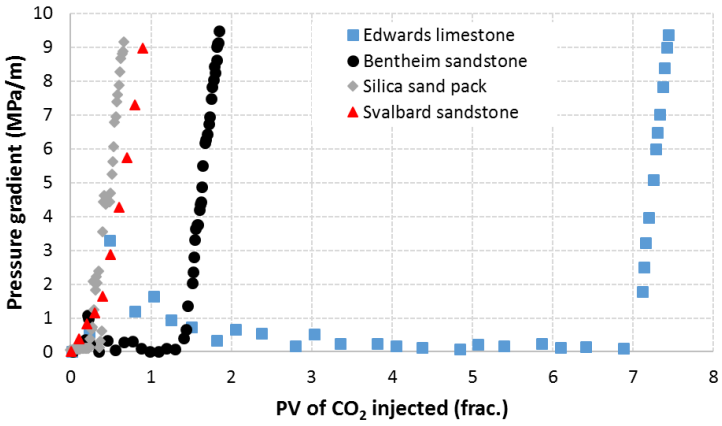

Figure 21. Development of physical flow barriers in silica sand (diamonds), Svalbard sandstone (triangles), Bentheim sandstone (circles), and Edwards limestone (squares) from CO_2 hydrate formation during CO_2 injection. Modified from **paper 6 and 7**.

The long-term integrity of the formed CO_2 hydrate seal was tested in each core material except from the silica sand pack. A differential pressure of 1.8 MPa was exerted across the length of the Svalbard sandstone core for 10 days without any water or CO_2 production. The CO_2 hydrate plug formed before the CO_2 broke through at the end of the core and hindered any CO_2 from reaching the production pump. In the Bentheim sandstone and Edwards limestone cores, CO_2 was produced for some time before the CO_2 hydrate plug formed. After sealing of the pore space, the outlet production line and production pump were emptied for CO_2. Accumulation of CO_2 at the outlet after

this point was quantified regularly for 71 days in the Bentheim sandstone and 40 days in the Edwards limestone. The amount of CO_2 escaping through the core plugs was significantly different when the same differential pressure of 1.5 MPa was imposed on each core plug. The average leakage rate of CO_2 was 0.01 mL/day during a 21 days period in the Bentheim sandstone whereas it was 0.1 mL/day in the Edwards limestone. The CO_2 hydrate plug was not just forming slower in the limestone compared to quartz-dominated porous media; the ability of the CO_2 hydrate plug to hinder CO_2 leakage was also lower in the limestone core plug. Increased fluid-rock interaction in the limestone may explain parts of the dissimilarity. The limestone core plug was visualized by MRI before and after the experiment was conducted, and parts of the core plug had clearly increased porosity because of rock dissolution and formation of vuggs. There might also be a wettability effect as calcite is observed to turn weakly CO_2-wet at high pressure and low temperature (Arif et al., 2017). In any case, the CO_2 hydrate self-sealing was less effective in carbonate rock compared to quartz-dominated rock.

4. Conclusions and Future Work

4.1 Conclusions

A multiscale approach was used to characterize gas hydrates in porous media. Observations made in micromodels at pore-scale linked with magnetic resonance imaging and pressure-volume-temperature measurements at core-scale have provided new insight in hydrate phase transitions in sediments. These learnings provide important contributions toward realizing production of CH_4 gas from CH_4 hydrate reservoirs and safe geological storage of CO_2 assisted by CO_2 hydrate formation.

The main conclusions related to production of CH_4 gas by pressure depletion of CH_4 hydrate-saturated porous media are:

- The growth pattern of CH_4 hydrates was highly affected by the initial distribution of water and CH_4 gas in the pore space. A porous hydrate with encapsulated CH_4 gas surrounded by a shell of CH_4 hydrate formed in regions with high CH_4 gas saturation and low water saturation. A solid nonporous hydrate formed and consumed all CH_4 gas in regions with low CH_4 gas saturation and high water saturation. The final CH_4 hydrate distribution was generally reflecting the initial water distribution.
- The CH_4 gas recovery rate during pressure depletion was highly affected by the CH_4 hydrate distribution in the pore space. The porous hydrate with encapsulated CH_4 gas dissociated fast while the solid nonporous hydrate dissociated slower because of ineffective pressure transmission through the pore network and low relative permeability of the liberated CH_4 gas. The maximum rate of CH_4 gas recovery was highest in the CH_4 hydrate saturation interval of 0.30 – 0.50 (frac.). The gas hydrate saturation and distribution are thus critical parameters that need to be assessed in order to forecast gas production rates and the potential lifetime of a specific hydrate accumulation.
- Solid CH_4 hydrates in the pore space reduced the effective permeability to CH_4 gas for constant CH_4 gas saturation. The effective permeability to CH_4 gas dropped from mD- to μD-values in the CH_4 gas saturation interval of 0.33 –

0.38 (frac.). The fitting exponent, *n,* in the modified Brooks-Corey curve increased from 2.7 to 3.6 when CH_4 hydrates formed in the pores.

The main conclusions related to storage and sealing of CO_2 by CO_2 hydrate formation in saline aquifers are:

- Solid CO_2 hydrates in the pore space reduced the effective permeability to liquid CO_2 for constant liquid CO_2 saturation. The effective permeability to liquid CO_2 dropped to zero at a liquid CO_2 saturation of around 0.40 (frac.) when CO_2 hydrates were present in the pores. The fitting exponent, *n,* in the modified Brooks-Corey curve increased from 4.0 to 5.8 when CO_2 hydrates formed in the pore network.
- Liquid CO_2 was quickly immobilized by the formation of CO_2 hydrates during liquid CO_2 injection in water-saturated rock. The CO_2 hydrate formed initially at the CO_2-water interface and then later crystallized the water phase into nonporous CO_2 hydrates. The formed CO_2 hydrate immobilized and trapped the excess liquid CO_2 effectively and demonstrated the viability of CO_2 hydrate self-sealing during CO_2 storage.
- In quartz-dominated rock core plugs, the CO_2 hydrate plug formed faster as the absolute permeability of the core plugs decreased. Narrow pore throats in tight rocks were more easily obstructed by thin CO_2 hydrate films that formed early in the nucleation process.
- The long-term leakage rate of CO_2 through the CO_2 hydrate plug was higher in an Edwards limestone core plug compared to a Bentheim sandstone core plug. The CO_2 hydrate self-sealing was slower and less robust in carbonate rock compared to quartz-dominated rock.

4.2 Future Work

The experience that was gained in this experimental work on CH_4 hydrate phase transitions in Bentheim sandstone core plugs should be extended to porous media that is more representative for gas hydrate accumulations in nature. This would include sediments like unconsolidated sand and silt with additions of clay minerals. The

interplay between gas hydrate phase transitions and the stress regime of the sediment is crucial during production of CH_4 gas from hydrate deposits.

The micromodels that were employed to visualize gas hydrate growth and dissociation at the pore-scale have unrealized potential to aid other aspects of gas hydrates research. Fundamental research on CH_4-CO_2 exchange in porous media saturated with CH_4 hydrate should benefit from direct pore-scale visualization. Phase transitions involving formation and melting of ice could also be studied in the micromodels and would shed light on the CH_4 gas production characteristics in permafrost sediments.

A more comprehensive investigation should be undertaken to reveal the differences between CO_2 hydrate self-sealing in sandstone and carbonate rocks. CO_2 storage in carbonates would benefit from *in situ* MR imaging to resolve possible formation of vuggs that might alter the sealing capability of the CO_2 hydrate.

Abbreviations

BP	British Petroleum (Beyond Petroleum)
CCS	Carbon capture and storage
CH_4	Methane
CO_2	Carbon dioxide
EIA	U.S. Energy Information Administration
Frac.	Fraction
GMGS	Guangzhou Marine Geological Survey
GtC	Gigatonnes of carbon
$GtCO_2$	Gigatonnes of carbon dioxide
H_2O	Water
IEA	International Energy Agency
IPCC	Intergovernmental Panel on Climate Change
JOGMEC	Japan Oil, Gas and Metals National Corporation
kWh	Kilowatt hour
Mtoe	Millions of tonnes of oil equivalent
MRI	Magnetic resonance imaging
NGHP	India National Gas Hydrate Program
NRCan	Natural Resources Canada
PV	Pore volume
PVT	Pressure volume temperature
UBGH	Ulleung Basin Gas Hydrate
UN	United Nations
USGS	U.S. Geological Survey
Wt%	Weight percent

Nomenclature

Φ	Porosity (frac.)
K	Permeability (D)
k_r	Relative permeability (frac.)
k^0_r	End-point relative permeability (frac.)
k_{ratio}	Relative permeability to gas when hydrate is present (three phases) divided by the relative permeability to gas without hydrate present (two phases), for equal gas saturation (frac.)
L	Dimensionless length (frac.)
n	Fitting exponent (-)
N	Fitting exponent (-)
n_g	Fitting exponent (-)
P	Pressure (MPa)
R_{CH4}	Recovery of CH_4 gas (frac.)
S^*	Fluid saturation scaled according to hydrate saturation (frac.)
S_{CH4}	Saturation of CH_4 (frac.)
S_{CO2}	Saturation of CO_2 (frac.)
S_H	Saturation of hydrate (frac.)
S_r	Residual saturation (frac.)
S_w	Saturation of water (frac.)
t	Time (s)
T	Temperature (°C)
T_2	Transverse relaxation time constant (ms)

References

Alpak, F.O., Lake, L.W. and S.M. Embid. *Validation of a Modified Carman-Kozeny Equation To Model Two-Phase Relative Permeabilities*. SPE Annual Technical Conference and Exhibition, Houston, Texas, USA, October 3-6, 1999.

Anderson, B.J., Boswell, R., Collett, T.S., Farrell, H., Ohtsuka, S. and M.D. White. *Review of the findings of the Ignik Sikumi CO2-CH4 gas hydrate exchange field trial.* Proceedings of the 8th International Conference on Gas Hydrates, Beijing, China, July 28-August 1, 2014.

Archer, D., Buffett, B. and V. Brovkin, 2009. Ocean methane hydrates as a slow tipping point in the global carbon cycle. *Proceedings of the National Academy of Sciences* **106**(49): 20596-20601.

Arif, M., Lebedev, M., Barifcani, A. and S. Iglauer, 2017. CO2 storage in carbonates: Wettability of calcite. *International Journal of Greenhouse Gas Control* **62:** 113-121.

Bachu, S, 2000. Sequestration of CO2 in geological media: criteria and approach for site selection in response to climate change. *Energy Conversion and Management* **41**(9): 953-970.

Bachu, S, 2015. Review of CO2 storage efficiency in deep saline aquifers. *International Journal of Greenhouse Gas Control* **40:** 188-202.

Beaudoin, Y.C., Waite, W.F., Boswell, R. and S.R. Dallimore (eds), 2014. *Frozen Heat: A UNEP Global Outlook on Methane Gas Hydrates*. Volume 1. United Nations Environment Programme, GRID-Arendal.

Boswell, R. and T.S. Collett, 2011. Current perspectives on gas hydrate resources. *Energy & Environmental Science* **2011**(4)**:** 1206-1215.

Boswell, R., Schoderbek, D., Collett, T.S., Ohtsuki, S., White, M. and B.J. Anderson, 2017. The Iġnik Sikumi Field Experiment, Alaska North Slope: Design, Operations, and Implications for CO2–CH4 Exchange in Gas Hydrate Reservoirs. *Energy & Fuels* **31**(1)**:** 140-153.

BP, 2019. *BP Energy Outlook 2019 edition* [Online]. Available: https://www.bp.com/en/global/corporate/energy-economics/energy-outlook.html [Accessed 19/8 2019].

Chaouachi, M., Falenty, A., Sell, K., Enzmann, F., Kersten, M., Haberthür, D. and W.F. Kuhs, 2015. Microstructural evolution of gas hydrates in sedimentary matrices observed with synchrotron X-ray computed tomographic microscopy. *Geochemistry, Geophysics, Geosystems* **16**(6)**:** 1711-1722.

Circone, S., Kirby, S.H. and L.A. Stern, 2005. Direct Measurement of Methane Hydrate Composition along the Hydrate Equilibrium Boundary. *The Journal of Physical Chemistry B* **109**(19)**:** 9468-9475.

Collett, T.S., Johnson, A.H., Knapp, C.C. and R. Boswell, 2009. Natural Gas Hydrates: A Review. *AAPG Memoir* **89:** 146-219.

Cook, A.E. and W.F. Waite, 2018. Archie's Saturation Exponent for Natural Gas Hydrate in Coarse-Grained Reservoirs. *Journal of Geophysical Research: Solid Earth* **123**(3): 2069-2089.

CSMGem, 2015. *Publicly available software* [Online]. Colorado: Colorado School of Mines, Center for Hydrate Research. Available: http://hydrates.mines.edu/CHR/Software.html [Accessed 2/3 2016].

Dvorkin, J., Nur, A. and H. Yin, 1994. Effective properties of cemented granular materials. *Mechanics of Materials* **18**(4): 351-366.

EIA, U.S., 2018. *International Energy Outlook 2018 (IEO2018)* [Online]. Washington, DC: U.S. Energy Information Administration. Available: https://www.eia.gov/outlooks/ieo/ [Accessed 19/8 2019].

EIA, U.S., 2019. *How much carbon dioxide is produced when different fuels are burned?* [Online]. Washington, DC: U.S. Energy Information Administration. Available: https://www.eia.gov/tools/faqs/faq.php?id=73&t=11 [Accessed 4/9 2019].

Graue, A., Kvamme, B., Baldwin, B., Stevens, J., Howard, J.J., Aspenes, E., Ersland, G., Husebo, J. and D. Zornes, 2008. MRI Visualization of Spontaneous Methane Production From Hydrates in Sandstone Core Plugs When Exposed to CO2. *SPE Journal* **13**(2): 146-152.

Hancock, S.H., Collett, T.S., Dallimore, S.R., Satoh, T., Inoue, T., Huenges, E., Henninges, J. and B. Weatherill, 2005. Overview of thermal-stimulation production-test results for the JAPEX/JNOC/GSC et al. Mallik 5L-38 gas hydrate production research well. In: Dallimore, S.R. and Collett, T.S. (eds.) *Scientific Results from the Mallik 2002 Gas Hydrate Production Research Well Program, Mackenzie Delta, Northwest Territories,* Canada, Geological Survey of Canada, Bulletin 585, 15 p.

Helgerud, M.B., Dvorkin, J., Nur, A., Sakai, A. and T.S. Collett, 1999. Elastic-wave velocity in marine sediments with gas hydrates: Effective medium modeling. *Geophysical Research Letters* **26**(13): 2021-2024.

Henning, R.W., Schultz, A.J., Thieu, V. and Y. Halpern, 2000. Neutron Diffraction Studies of CO2 Clathrate Hydrate: Formation from Deuterated Ice. *The Journal of Physical Chemistry A* **104**(21): 5066-5071.

Hu, G.W., Ye, Y.G., Zhang, J., Liu, C.L., Diao, S.B. and J.S. Wang, 2010. Acoustic properties of gas hydrate–bearing consolidated sediments and experimental testing of elastic velocity models. *Journal of Geophysical Research: Solid Earth* **115**(B2): 11 p.

IEA, 2018a. *Key World Energy Statistics (KWES) 2018* [Online]. France: International Energy Agency. Available: https://webstore.iea.org/key-world-energy-statistics-2018 [Accessed 19/8 2019].

IEA, 2018b. *World Energy Outlook 2018* [Online]. France: OECD/IEA. Available: https://webstore.iea.org/world-energy-outlook-2018 [Accessed 19/8 2019].

Inui, M. and T. Sato. *Economical feasibility study on CO2 sequestration in the form of gas hydrate under seafloor*. Proc. 25th Int. Conf. Offshore Mech. Arctic Eng., Hamburg, Germany, 2006.

IPCC, 2005. IPCC Special Report on Carbon Dioxide Capture and Storage. Prepared by Working Group III of the Intergovernmental Panel on Climate Change [Metz, B., O. Davidson, H.C. de Coninck, M. Loos and L.A. Meyer (eds.)]. Cambridge, United Kingdom and New York, U.S.A.

IPCC, 2014. Climate Change 2014: Synthesis Report. Contribution of Working Groups I, II and III to the Fifth Assessment Report of the Intergovernmental Panel on Climate Change [Core Writing Team, R.K. Pachauri and L.A. Meyer (eds.)]. Geneva, Switzerland.

IPCC, 2018. Summary for Policymakers. In: *Global Warming of 1.5°C. An IPCC Special Report on the impacts of global warming of 1.5°C above pre-industrial levels and related global greenhouse gas emission pathways, in the context of strengthening the global response to the threat of climate change, sustainable development, and efforts to eradicate poverty* [Masson-Delmotte, V., P. Zhai, H.-O. Pörtner, D. Roberts, J. Skea, P.R. Shukla, A. Pirani, W. Moufouma-Okia, C. Péan, R. Pidcock, S. Connors, J.B.R. Matthews, Y. Chen, X. Zhou, M.I. Gomis, E. Lonnoy, T. Maycock, M. Tignor, and T. Waterfield (eds.)]. World Meteorological Organization, Geneva, Switzerland, 32 p.

Kerkar, P.B., Horvat, K., Jones, K.W. and D. Mahajan, 2014. Imaging methane hydrates growth dynamics in porous media using synchrotron X-ray computed microtomography. *Geochemistry, Geophysics, Geosystems* **15**(12): 4759-4768.

Klauda, J.B. and S.I. Sandler, 2005. Global Distribution of Methane Hydrate in Ocean Sediment. *Energy & Fuels* **19**(2): 459-470.

Kleinberg, R.L., Flaum, C., Griffin, D.D., Brewer, P.G., Malby, G.E., Peltzer, E.T. and J.P. Yesinowski, 2003. Deep sea NMR: Methane hydrate growth habit in porous media and its relationship to hydraulic permeability, deposit accumulation, and submarine slope stability. *Journal of Geophysical Research: Solid Earth* **108**(B10): 17 p.

Koide, H., Takahashi, M., Shindo, Y., Tazaki, Y., Iijima, M., Ito, K., Kimura, N. and K. Omata, 1997. Hydrate formation in sediments in the sub-seabed disposal of CO2. *Energy* **22**(2-3): 279-283.

Koide, H., Takahashi, M., Tsukamoto, H. and Y. Shindo, 1995. Self-trapping mechanisms of carbon dioxide in the aquifer disposal. *Energy Conversion and Management* **36**(6-9): 505-508.

Konno, Y., Fujii, T., Sato, A., Akamine, K., Naiki, M., Masuda, Y., Yamamoto, K. and J. Nagao, 2017. Key Findings of the World's First Offshore Methane Hydrate Production Test off the Coast of Japan: Toward Future Commercial Production. *Energy & Fuels* **31**(3): 2607-2616.

Kretschmer, K., Biastoch, A., Rüpke, L. and E. Burwicz, 2015. Modeling the fate of methane hydrates under global warming. *Global Biogeochemical Cycles* **29**(5): 610-625.

Kumar, A., Maini, B., Bishnoi, P.R., Clarke, M., Zatsepina, O. and S. Srinivasan, 2010. Experimental determination of permeability in the presence of hydrates and its effect on the dissociation characteristics of gas hydrates in porous media. *Journal of Petroleum Science and Engineering* **70**(1-2): 114-122.

Lee, J.Y., Francisca, F.M., Santamarina, J.C. and C. Ruppel, 2010. Parametric study of the physical properties of hydrate-bearing sand, silt, and clay sediments: 2. Small-strain mechanical properties. *Journal of Geophysical Research: Solid Earth* **115**(B11): 11 p.

Lee, M.W. and T.S. Collett, 2008. Integrated analysis of well logs and seismic data to estimate gas hydrate concentrations at Keathley Canyon, Gulf of Mexico. *Marine and Petroleum Geology* **25**(9): 924-931.

Li, B., Li, X.S., Li, G., Jia, J.L. and J.C. Feng, 2013. Measurements of Water Permeability in Unconsolidated Porous Media with Methane Hydrate Formation. *Energies* **6**(7): 3622-3636.

Li, J.F., Ye, J.L., Qin, X.W., Qiu, H.J., Wu, N.Y., Lu, H.L., Xie, W.W., Lu, J.A., Peng, F., Xu, Z.Q., Lu, C., Kuang, Z.G., Wei, J.G., Liang, Q.Y., Lu, H.F. and B.B. Kou, 2018. The first offshore natural gas hydrate production test in South China Sea. *China Geology* **1**(1): 5-16.

Liang, Y.P., Liu, S., Wan, Q.C., Li, B., Liu, H. and X. Han, 2018. Comparison and Optimization of Methane Hydrate Production Process Using Different Methods in a Single Vertical Well. *Energies* **12**(1): 124.

Mahabadi, N., Dai, S., Seol, Y., Sup Yun, T. and J. Jang, 2016. The water retention curve and relative permeability for gas production from hydrate-bearing sediments: pore-network model simulation. *Geochemistry, Geophysics, Geosystems* **17**(8): 3099-3110.

Masuda, Y., Naganawa, S., Ando, S. and K. Sato. *Numerical calculation of gas production performance from reservoirs containing natural gas hydrates*. SPE Annual Technical Conference, San Antonio, Texas, USA, 1997.

Milkov, A.V. 2004. Global estimates of hydrate-bound gas in marine sediments: how much is really out there? *Earth-Science Reviews* **66**(3-4): 183-197.

Moridis, G., Collett, T.S., Pooladi-Darvish, M., Hancock, S.H., Santamarina, C., Boswell, R., Kneafsey, T.J., Rutqvist, J., Kowalsky, M.B., Reagan, M.T., Sloan, E.D., Sum, A. and C. Koh, 2011. Challenges, Uncertainties, and Issues Facing Gas Production From Gas-Hydrate Deposits. *SPE Reservoir Evaluation & Engineering* **14**(1): 76-112.

Moridis, G.J., Kowalsky, M.B. and K. Pruess, 2007. Depressurization-Induced Gas Production From Class-1 Hydrate Deposits. *SPE Reservoir Evaluation & Engineering* **10**(5): 458-481.

Moridis, G.J. and K. Pruess, 2014. User's Manual of the Tough+ Core Code v1.5: A General-Purpose Simulator of Non-Isothermal Flow and Transport Through Porous and Fractured Media, Report LBNL-6871E. Berkeley, California: Lawrence Berkeley National Laboratory.

Moridis, G.J. and M.T. Reagan. *Gas Production From Oceanic Class 2 Hydrate Accumulations*. Offshore Technology Conference, Houston, Texas, USA, April 30-May 3, 2007.

Priest, J.A., Best, A.I. and C.R.I. Clayton, 2005. A laboratory investigation into the seismic velocities of methane gas hydrate-bearing sand. *Journal of Geophysical Research: Solid Earth* **110**(B4): 13 p.

Priest, J.A., Rees, E.V.L. and C.R.I. Clayton, 2009. Influence of gas hydrate morphology on the seismic velocities of sands. *Journal of Geophysical Research: Solid Earth* **114**(B11): 13 p.

Reagan, M.T., Moridis, G.J. and K. Zhang. *Sensitivity Analysis of Gas Production From Class 2 and Class 3 Hydrate Deposits*. Offshore Technology Conference, Houston, Texas, USA, May 5-8, 2008.

Rochelle, C.A., Camps, A.P., Long, D., Milodowski, A., Bateman, K., Gunn, D., Jackson, P., Lovell, M.A. and J. Rees, 2009. Can CO2 hydrate assist in the underground storage of carbon dioxide? *Geological Society, London, Special Publications* **319**: 171-183.

Ruppel, C.D. and J.D. Kessler, 2017. The interaction of climate change and methane hydrates. *Reviews of Geophysics* **55**(1): 126-168.

Sloan, E.D. and C. Koh, 2008. *Clathrate Hydrates of Natural Gases,* Boca Raton, Florida, USA, CRC Press.

Teng, Y. and D. Zhang, 2018. Long-term viability of carbon sequestration in deep-sea sediments. *Science Advances* **4**(7): 8 p.

Udachin, K.A., Ratcliffe, C.I. and J.A. Ripmeester, 2001. Structure, Composition, and Thermal Expansion of CO2 Hydrate from Single Crystal X-ray Diffraction Measurements. *The Journal of Physical Chemistry B* **105**(19): 4200-4204.

United Nations, 2015. *Paris Agreement* [Online]. France: United Nations. Available: https://unfccc.int/process-and-meetings/the-paris-agreement/the-paris-agreement [Accessed 20/8 2019].

United Nations, 2019. *The Sustainable Development Goals Report 2019* [Online]. New York: United Nations. Available: https://www.un.org/sustainabledevelopment/energy/ [Accessed 19/8 2019].

Waite, W.F., Winters, W.J. and D.H. Mason, 2004. Methane hydrate formation in partially water-saturated Ottawa sand. *American Mineralogist* **89**(8-9): 1202-1207.

Yamamoto, K. and S. Dallimore, 2008. Aurora-JOGMEC-NRCan Mallik 2006-2008 Gas Hydrate Research Project Progress. *Fire in the Ice, Methane Hydrate Newsletter* **8**(3): 1-5.

Yamamoto, K., Wang, X.X., Tamaki, M. and K. Suzuki, 2019. The second offshore production of methane hydrate in the Nankai Trough and gas production behavior from a heterogeneous methane hydrate reservoir. *RSC Advances* **9**(45): 25987-26013.

You, K., Flemings, P.B., Malinverno, A., Collett, T.S. and K. Darnell, 2019. Mechanisms of Methane Hydrate Formation in Geological Systems. *Reviews of Geophysics* **57**: 51 p.

Scientific Papers

1) **Almenningen, S.**, Fotland, P. and G. Ersland, 2019. Magnetic Resonance Imaging of Methane Hydrate Formation and Dissociation in Sandstone with Dual Water Saturation. *Energies* **12**(17): 3231.

2) **Almenningen, S.**, Iden, E., Fernø, M.A. and G. Ersland, 2018. Salinity Effects on Pore-Scale Methane Gas Hydrate Dissociation. *J. Geophys. Res. Solid Earth* **123**(7): 5599-5608.

3) **Almenningen, S.**, Fotland, P., Fernø, M.A. and G. Ersland, 2019. An Experimental Investigation of Gas Production Rates During Depressurization of Sedimentary Methane Hydrates. *SPE J.* **24**(2): 1-9.

4) **Almenningen, S.**, Gauteplass, J., Hauge, L.P., Barth, T., Fernø, M.A. and G. Ersland, 2019. Measurements of CH_4 and CO_2 relative permeability in hydrate-bearing sandstone. *J. Petrol. Sci. Eng.* **177**: 880-888.

5) **Almenningen, S.**, Gauteplass, J., Fotland, P., Aastveit, G.L., Barth, T. and G. Ersland, 2018. Visualization of hydrate formation during CO_2 storage in water-saturated sandstone. *Int. J. Greenh. Gas Con.* **79**: 272-278.

6) Gauteplass, J., **Almenningen, S.**, Ersland, G., Barth, T., Yang, J. and A. Chapoy, 2020. Multiscale investigation of CO_2 hydrate self-sealing potential for carbon geo-sequestration. *Chem. Eng. J.* **381**: 122646.

7) **Almenningen, S.**, Betlem, P., Hussain, A., Roy, S., Senger, K. and G. Ersland, 2019. Demonstrating the potential of CO_2 hydrate self-sealing in Svalbard, Arctic Norway. *Int. J. Greenh. Gas Con.* **89**: 1-8.

I

energies

MDPI

Article

Magnetic Resonance Imaging of Methane Hydrate Formation and Dissociation in Sandstone with Dual Water Saturation

Stian Almenningen [1,*], Per Fotland [2] and Geir Ersland [1]

[1] Department of Physics and Technology, University of Bergen, 5007 Bergen, Norway
[2] Equinor ASA, 5020 Bergen, Norway
* Correspondence: stian.almenningen@uib.no

Received: 9 July 2019; Accepted: 19 August 2019; Published: 22 August 2019

Abstract: This paper reports formation and dissociation patterns of methane hydrate in sandstone. Magnetic resonance imaging spatially resolved hydrate growth patterns and liberation of water during dissociation. A stacked core set-up using Bentheim sandstone with dual water saturation was designed to investigate the effect of initial water saturation on hydrate phase transitions. The growth of methane hydrate (P = 8.3 MPa, T = 1–3 °C) was more prominent in high water saturation regions and resulted in a heterogeneous hydrate saturation controlled by the initial water distribution. The change in transverse relaxation time constant, T_2, was spatially mapped during growth and showed different response depending on the initial water saturation. T_2 decreased significantly during growth in high water saturation regions and remained unchanged during growth in low water saturation regions. Pressure depletion from one end of the core induced a hydrate dissociation front starting at the depletion side and moving through the core as production continued. The final saturation of water after hydrate dissociation was more uniform than the initial water saturation, demonstrating the significant redistribution of water that will take place during methane gas production from a hydrate reservoir.

Keywords: methane hydrates in sandstone; phase transitions; magnetic resonance imaging

1. Introduction

Natural gas hydrates are crystalline compounds consisting of structured water stabilized by guest molecules. In nature, methane is the typical hydrate former and subsurface methane hydrates constitute a currently untapped global energy resource. The estimates of methane bound in hydrates vary between 10^{14} and 10^{18} m^3 at STP [1], where around 99% of the hydrates exist in submarine sediments [2]. Several short-term field pilots have been undertaken to prove the concept of methane gas production from methane hydrates: depressurization and associated hydrate dissociation onshore [3], depressurization offshore [4], and CO_2 injection and subsequent methane production onshore [5]. Important parameters for all production schemes are the hydrate saturation and distribution within the pore space. The hydrate, water, and gas saturation in the reservoir govern the rate of methane recovery during depressurization-induced hydrate dissociation [6]. Understanding the growth pattern of methane hydrate within pores is thus considered important to be able to predict the production response in different hydrate accumulations based on the local saturation distribution.

Magnetic resonance imaging (MRI) is a powerful tool to characterize natural sediments [7] and to measure and visualize flow and reactions in porous media [8–10]. MRI is based on aligning nuclear spins, usually hydrogen-nuclei, in a magnetic field and recording the response of the nuclei as they are exposed to radiofrequency pulses. The recorded response is used to map the amount of nuclei

inside the porous media. The non-invasive imaging technique is particularly useful for hydrate phase transitions in sedimentary core plugs. The spin-spin relaxation of hydrogen-nuclei in liquid water is slower than the relaxation of hydrogen-nuclei in solid hydrates, making the liquid water detectable during MR scans, in contrast to solid hydrates. The onset of hydrate formation is detected as a loss of signal when liquid water converts to hydrates, and hydrate dissociation is recognized as a signal increase when liquid water re-appears during hydrate dissociation. This technique has previously been reported to track the amount of water in sediments both spatially and temporally during hydrate growth and dissociation [11–13]. MRI has also been used to prove the concept of CO_2–CH_4 exchange when methane hydrate in sandstone is exposed to CO_2 [8,14].

This paper reports the spatial growth pattern of methane hydrates in sandstone cores at sub-cm scale. A dual water saturation system created by aligning two cores with different initial water saturation was used to identify the effect of water saturation. MRI spatially visualized methane hydrate growth and subsequent hydrate dissociation with respect to initial water saturation. Interpretation of T_2 measurements during hydrate phase transitions improved the understanding of hydrate growth and dissociation patterns at pore-scale.

2. Materials and Methods

2.1. Experimental Set-Up

Cylindrical Bentheim sandstone cores with an average porosity and permeability of 22–24% and 1–2 D, respectively, were used as host sediment for the hydrate phase transitions. The sandstone was fairly clean and consisted of around 96% quartz sand [15]. The specialized core holder was made from polyether ether ketone (PEEK) and titanium materials to ensure the compatibility with the MR instrument (Figure 1). Floating end-pieces (PEEK) were positioned on each side of the core inside a rubber sleeve and uniaxial core confinement was provided by pressurized fluorinert (liquid containing no hydrogen). Both flow lines leading into the core were connected to a high-pressure, high-precision pump (Quizix Q6000, Chandler Engineering, Tulsa, USA), which controlled the pore pressure. A custom-made cooling jacket was fitted around the core holder and the temperature was regulated by throughput of precooled air. A temperature sensor (TMQIN-062U-12, Omega, Manchester, United Kingdom) located in the confining fluorinert next to the inlet end-piece monitored the system temperature. The entire core holder was placed inside the MR instrument for real-time image acquisition. The superconductive magnet (BioSpec 47/40 USR, Bruker, Rheinstetten, Germany) had a magnetic field strength of 4.7 T (200 MHz) and could accommodate cylindrical core holders with diameters up to 19 cm. The longitudinal field of view limited the total length of the cores to 12 cm.

2.2. Experimental Procedure

Two cylindrical core samples with equal diameters of 6.31 cm and lengths of 7.93 and 3.93 cm were stacked and mounted in the core holder (Figure 2). In the first experiment (Exp. 1), the short core was completely saturated by 0.1 wt% NaCl brine and the long core was dry (air-filled). In the second experiment (Exp. 2), the cores were reassembled with opposite saturation with the long core completely saturated by brine, while the short core remained dry. However, the dry core was partly saturated with brine in both of the experiments when the cores were mounted in the core holder. Spontaneous imbibition and compression by the confining pressure moved some water from the wet core into the dry core. The resulting stacked cores acted as a composite core with dual water saturation (Figure 2), enabling investigation of the effect of initial water saturation on methane hydrate growth. One pump filled with water (0.1 wt% NaCl) was connected to the water-filled core, whereas another pump filled with methane gas provided pressure control to the low water saturation core. The pore pressure was subsequently increased to 8.30 MPa by injecting gas from one side, while the effective overburden pressure was continuously kept at 3.00 MPa. The system was left for five days to saturate the pore water completely with dissolved methane.

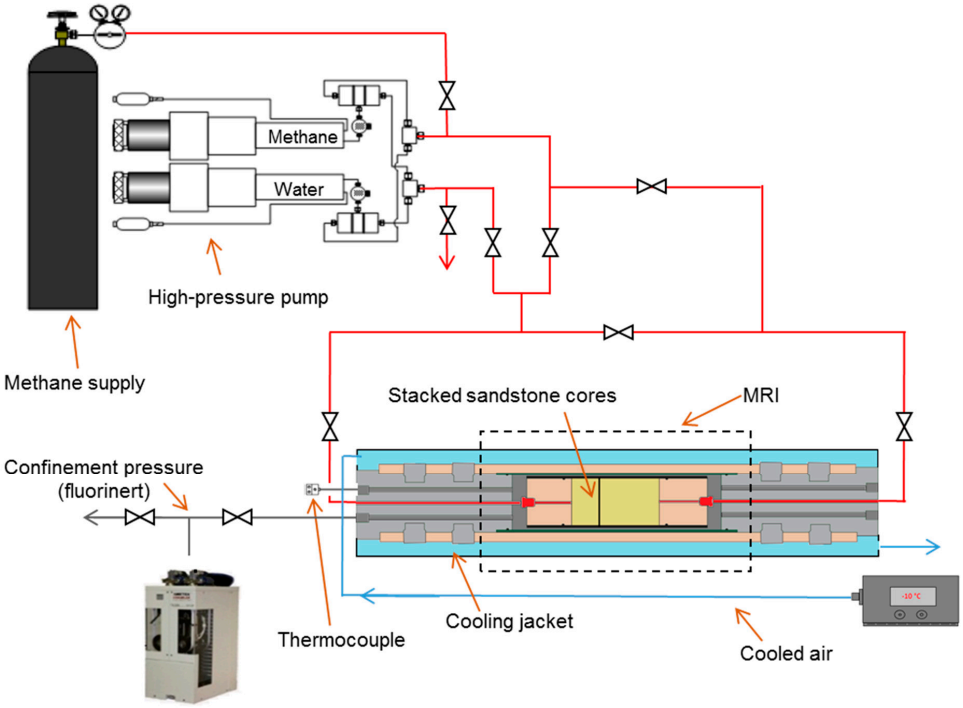

Figure 1. Schematic of experimental set-up. High-pressure flow lines for methane gas and water in red, cooled air for temperature control in light blue, and pressurized fluorinert for confinement pressure in gray.

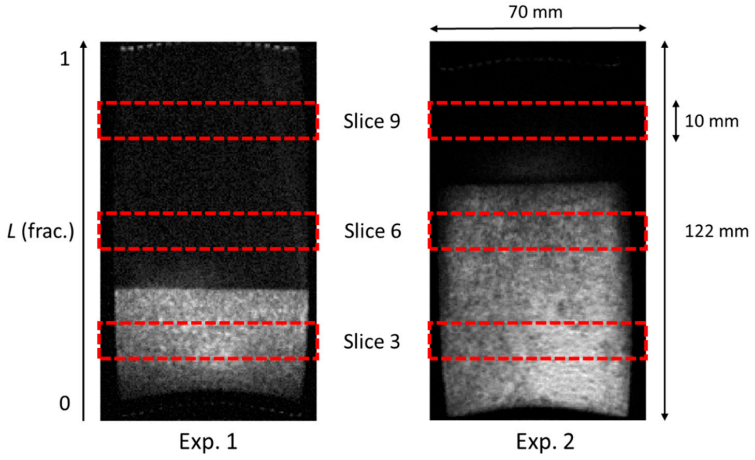

Figure 2. Sagittal view of the initial water saturation in the composite core. Exp. 1 (**left**) started with a short water-filled core stacked together with a long air-filled core. Exp. 2 (**right**) started with the opposite saturation in the cores. The red dashed rectangles mark the position of the three axial slices that are used to visualize hydrate growth throughout the results section.

Hydrate formation initiated after reducing the temperature to approximately 1–3 °C. The pore pressure remained constant at 8.30 MPa throughout the growth process, and the amount of methane gas consumed by hydrate formation determined the hydrate saturation. The change in water saturation was in sequence monitored by two different MR scan protocols: (1) The distribution of water was visualized and quantified by RAREst 2D scans (rapid acquisition with relaxation enhancement with short echo time). The echo time was set to 5.84 ms and the voxel resolution was 0.5 × 0.5 × 1.0 mm. Twelve axial slices with a thickness of 10 mm and a slice gap of 0.5 mm covered the entire length of the composite core sample. A short scan time of 4 min 5 s was enabled by a Rare factor of two and no signal averaging. (2) The pore-scale water distribution measurements (T_2 mapping) were inferred by MSME 2D scans (multi slice-multi echo). An echo time of 6.25 ms was used with 100 echo images in each echo train. Axial slices with the same resolution as for the RAREst scans were used and the scan time was 17 min 39 s. The slices obtained by RAREst scans were cropped circularly with the same diameter as the core, and the average background noise was subtracted from the signal intensity of each voxel in the core. The water saturation was found by correlating the average signal intensity of the entire core with volume logs from the pump. Local hydrate saturation was calculated assuming changes in water saturation corresponded to hydrate growth and no redistribution of water between voxels. The MSME slices were cropped and an average T_2 decay curve was extracted from each cross-section of the core. Application of inverse Laplace transform converted the decay curve to a T_2 distribution curve. The local average T_2 value was calculated throughout the hydrate growth process.

Two different approaches were used to dissociate the hydrate in the two experiments. In Exp. 1, the gas permeability was nonzero after hydrate formation and the gas permeability was estimated by constant volumetric gas injection and application of Darcy's law. The pressure was then reduced from one side of the core by constant volumetric gas extraction (0.5 mL/min) until complete dissociation. In Exp. 2, the apparent gas permeability was zero, indicating complete blockage of pores. In this case, the pressure reduction was initiated from both ends of the core and the pressure was lowered until approximately 0.8 MPa above the dissociation pressure. Hydrate dissociation followed by constant volumetric gas production (1.0 mL/min) from one side of the core while monitoring the differential pressure across the core. The production pressure was later set constant to 4.00 MPa when the differential pressure reached 1.00 MPa, and was maintained constant throughout the rest of the dissociation process. The same MR scans as for hydrate formation were acquired during hydrate dissociation.

3. Results and Discussions

3.1. Intensity vs. Water Saturation

The signal intensity in each voxel obtained by the RAREst scan is a relative measure of the amount of liquid water in each voxel. However, spin-echo based sequences (e.g., RAREst) are sensitive to the applied echo time as the transverse relaxation of hydrogen-nuclei in liquid water residing close to solid grains may be too fast for signal capture. The effect is more prominent for high surface relaxivity (paramagnetic ions) and low water saturation in water-wet porous media as the surface-to-volume ratio increases. Additionally, the transverse relaxation is enhanced as the water molecules diffuse through internal gradients in the pores that arise from magnetic susceptibility differences between the water and solid grains [16]. The relationship between signal intensity and water saturation during hydrate growth was thus investigated, and is shown for both experiments in Figure 3. The average water saturation during hydrate growth was calculated based on the amount of consumed methane gas at a constant pressure [17]. A hydration number of 5.99 was used [18]. As seen from Figure 3, the measured signal intensity (average) deviates from the linear trend for water saturations lower than 0.5. A polynomial correlation (dotted lines) was used to estimate local water saturations.

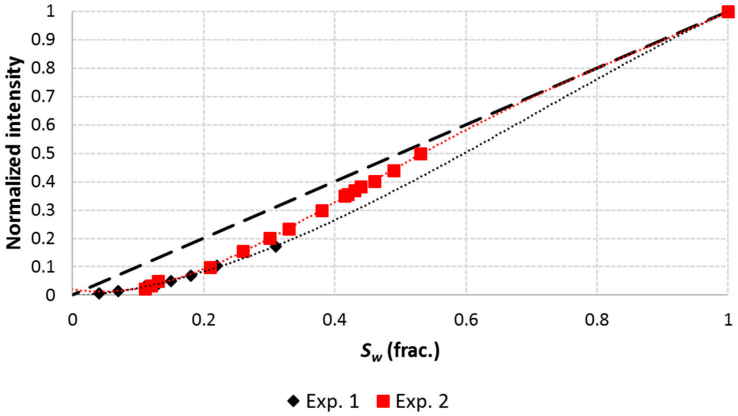

Figure 3. Correlation between average voxel intensity and average water saturation for both experiments. A linear trend line based on the end-point measurement (S_w = 1) is added for comparison. Notice that the measured intensity values are lower than the linear correlation for S_w of less than approximately 0.5.

3.2. Methane Hydrate Growth

The initial condition for the first experiment was a dual water saturation system where one-third of the composite sandstone core had high water saturation and two-thirds had low water saturation (detailed saturation in Figure 4). The methane hydrate growth initiated throughout the length of the core, but most of the hydrate formed in the high water saturation region. Here, the initial water saturation of 0.7 was converted to a hydrate saturation of 0.8 after three days of formation. During the same time, the low water saturation region ($S_w \approx 0.2$) yielded a final hydrate saturation of 0.1–0.2. Most of the pore water formed hydrate and a uniform water saturation of less than 0.1 remained after formation. The high degree of water conversion to hydrate is believed to be facilitated by a combination of the following: (1) The initial saturation of 0.7 water and 0.3 methane gas ensured a large interfacial area between water and gas. Methane gas, being the non-wetting phase, was distributed as connected channels in the middle of the pore space. The large interface between water and gas promoted methane diffusion into the water phase and provided an extensive interfacial area for nucleation of hydrate. (2) The effect of salt inhibition during hydrate growth was minor because the initial water salinity was only 0.1 wt% NaCl.

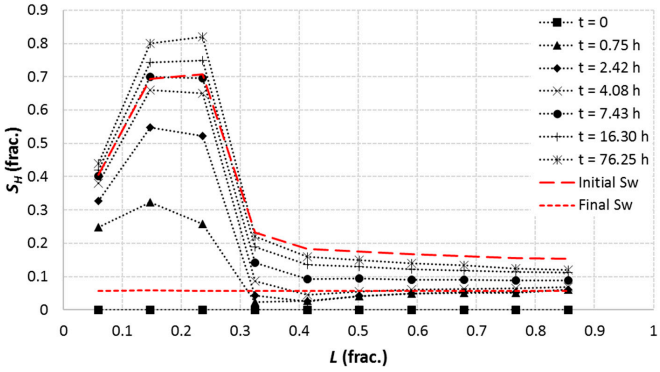

Figure 4. Methane hydrate saturation profiles during hydrate growth in Exp. 1. The pressure and temperature were kept constant at 8.30 ± 0.03 MPa and 2.3 ± 0.5 °C, respectively.

Axial imaging of the core revealed that the initial water saturation was distributed in transverse bands in the high water saturation region as a result of laminations in the Bentheim sandstone (Figure 5). These high water saturation bands likely reflected areas with smaller pore sizes than the adjacent areas where the water was displaced by gas. The initial fast hydrate growth in these bands containing tighter pores is similar to the increased growth rate observed for smaller grain sizes [11,19]. Preferred formation of hydrate in high water saturation regions was also observed by Seol & Kneafsey [20]. The nature of nucleation and number of nucleation sites [19] was not resolved with the sampling frequency used. However, the hydrate growth was not observed to propagate like a front in either of the directions, which have been observed previously [13].

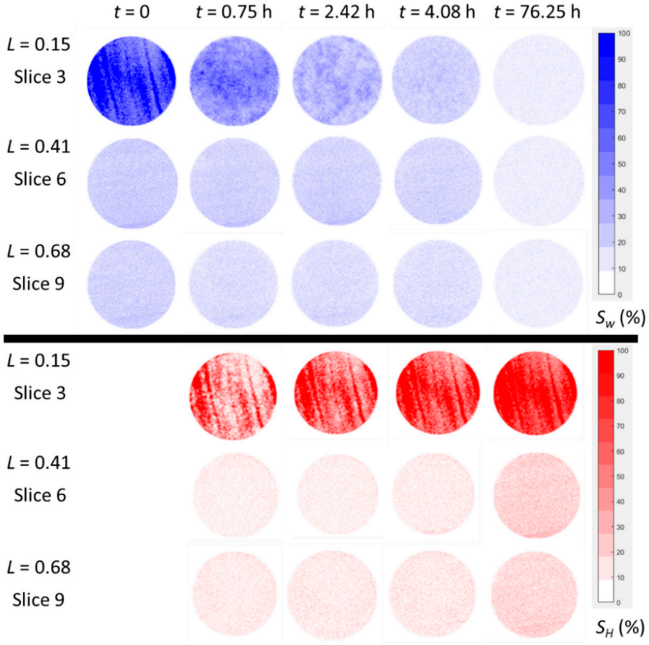

Figure 5. Water distribution (**top**) and methane hydrate distribution (**bottom**) in three different cross-sections of the composite core during hydrate growth in Exp. 1. The pressure and temperature were kept constant at 8.30 ± 0.03 MPa and 2.3 ± 0.5 °C, respectively.

The initial water saturation in Exp. 2 was close to unity in one end of the composite core and decreasing towards 0.1–0.2 in the other end (Figure 6). The resulting hydrate saturation followed the same distribution and decreased from 0.9 to 0 along the length of the core. The local amount of water limited the final amount of hydrate that was generated, similar to that observed in Exp. 1. The overall hydrate formation ceased at a uniform water saturation of around 0.1. The growth of hydrate in the low water saturation region ($L > 0.65$) started after more than one day of growth in the high water saturation region ($L < 0.65$). The trend was that the growth of hydrate started and continued in the high water saturation region until the water saturation dropped to similar values as in the low water saturation region. At this point, the hydrate growth also started in the low water saturation region. The location of water in relation to the grain surfaces may affect the hydrate formation and will be discussed later in this section. The formation of hydrate was faster in the high water saturation areas within each cross-section of the core (Figure 7). However, the growth pattern had no clear direction within the high water saturation areas, for example, radially inwards from the core perimeter or from one side to the other [12]. The growth pattern was spatially heterogeneous, as observed by Bagherzadeh et al. [19].

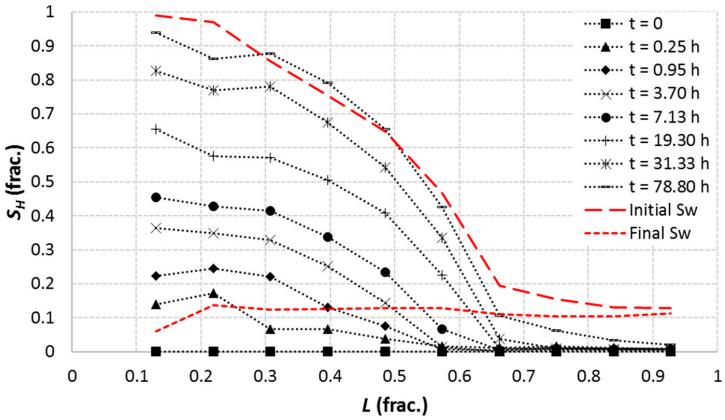

Figure 6. Methane hydrate saturation profiles during hydrate growth in Exp. 2. The pressure and temperature were kept constant at 8.30 ± 0.03 MPa and 3 ± 1 °C, respectively.

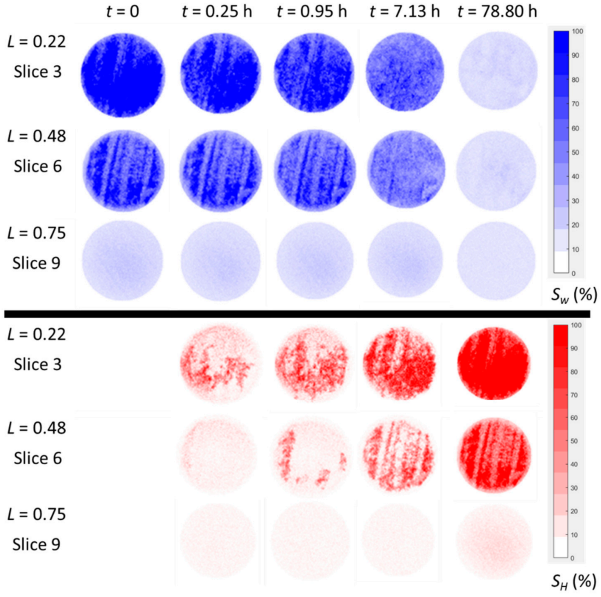

Figure 7. Water distribution (**top**) and methane hydrate distribution (**bottom**) in three different cross-sections of the composite core during hydrate growth in Exp. 2. The pressure and temperature were kept constant at 8.30 ± 0.03 MPa and 3 ± 1 °C, respectively.

The different saturation regions yielded different T_2 distribution curves, as the area under the T_2 distribution curve for a given slice is proportional to the water saturation in that slice (Figure 8). In addition, the response of the average T_2 was clearly different for the high- and low-saturation regions (Figures 9 and 10). The average T_2 was initially high and decreased nearly linearly with the increase in hydrate saturation as hydrate formed in the high water saturation regions. The reduction in average T_2 implies that the surface-to-volume ratio of the liquid water increased, which would be the result independent of how the hydrate nucleated in a water-filled pore. Nucleation in the middle of the pore or at the grain surface would both lead to an increase of the surface-to-volume ratio. However,

the rapid decline in average T_2 suggests that the hydrate formed in the middle of the pores in the high water saturation regions. The same decrease in average T_2 was not observed for the low water saturation regions, where the initial average T_2 already was low as a result of water residing at the grain surfaces (Figures 9 and 10). Here, the limited amount of hydrate growth was accompanied with an unaltered average T_2 value. Pore-scale methane hydrate growth has previously been shown to follow the gas–water interface in an excess gas system [21]. A similar growth pattern here was probably the reason that only small amounts of hydrate formed in the low water saturation regions. Thin layers of hydrate formed between gas occupying the center of pores and water residing close to grains. The average T_2 ended at approximately the same value (5–10 ms) throughout the whole core after hydrate formation independent of the initial water saturation. This implies that the amount and configuration of remaining water were the same after hydrate formation in regions with both high and low initial water saturation. The only difference between the regions was the extent to which the rest of the pore space was filled with hydrate compared with gas. In either way, the remaining water was likely bound to the grain surfaces and could not convert to hydrate because of the low activity associated with bound water [22] and/or lack of methane supply. In another study, a submicron to micron thick water film was always present between gas hydrate and the hydrophilic quartz surface [23].

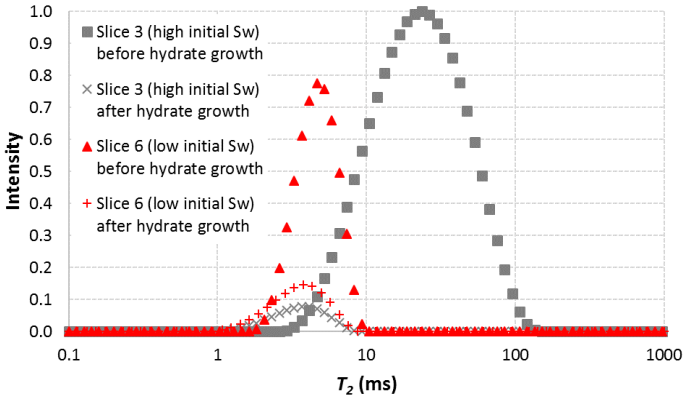

Figure 8. Distribution of transverse relaxation time constant, T_2, for Exp. 1. In slice 3 (high initial S_w), the intensity of the distribution decreases and shifts leftwards as the hydrate grows. The intensity of the distribution in slice 6 (low initial S_w) decreases as the hydrate grows, but the average T_2 remains constant.

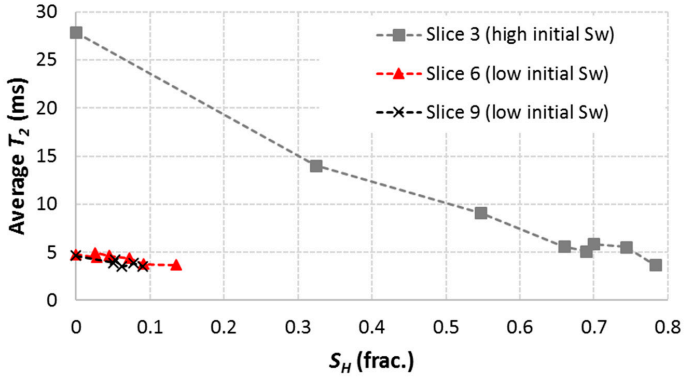

Figure 9. Average T_2 in three different cross-sections of the core during hydrate growth in Exp. 1.

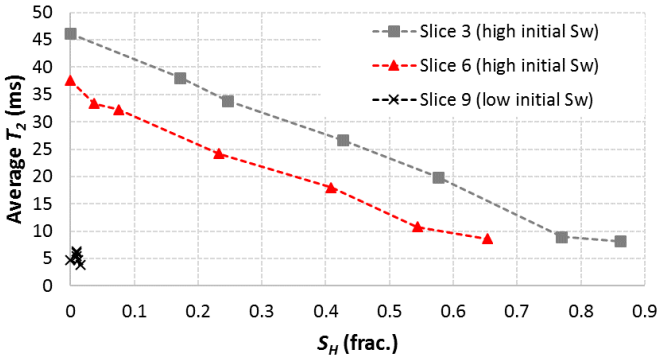

Figure 10. Average T_2 in three different cross-sections of the core during hydrate growth in Exp. 2.

3.3. Methane Hydrate Dissociation

The permeability of the core in Exp. 1 was significantly reduced after hydrate formation and the effective gas permeability was measured to 0.8 mD. In comparison, the absolute permeability of Bentheim sandstone is 1–2 D. The relatively low, but significant permeability suggests that the pressure reduction transmitted throughout the core during gas production from one side, that is, no differential pressure was introduced across the core during the production period. Producing gas with constant volumetric flow rate of 0.5 mL/min triggered hydrate dissociation at the production side (L = 1) when the pressure reached 3.74 MPa (Figure 11). The dissociation started at the production side and propagated through the core as a front, even though the differential pressure was zero. It should be noted that the cooling of the core holder was configured in a way that introduced the cooling medium (air) into the cooling jacket at L = 0, and then it flowed along the length of the core holder and exited at L = 1. This cooling set-up would induce a minor temperature gradient along the length of the core. The start of the hydrate dissociation at the production side may thus be a result of a slightly elevated temperature compared to the far (cooler) end of the core. The initial dissociation at P = 3.74 MPa implies that the temperature was 3.6 °C based on the stability pressure of methane hydrate [24], which is close to the 3.0 ± 0.6 °C that was measured in the confining liquid during the dissociation process. The dissociation pattern within each axial slice was also different from the observed hydrate growth pattern (Figure 12). The dissociation seemed to start at one place and then spread transversally from there.

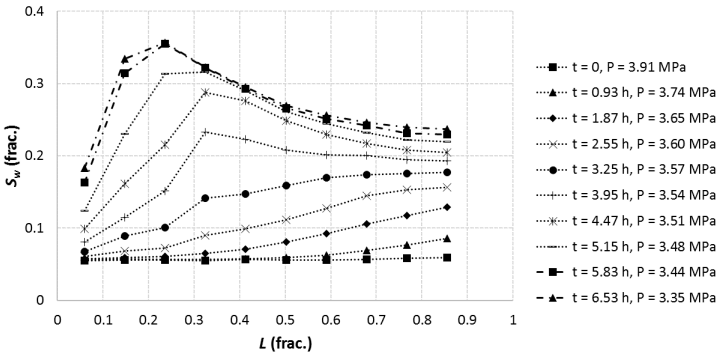

Figure 11. Water saturation profiles during hydrate dissociation in Exp. 1. Methane gas was produced with constant volumetric flow rate of 0.5 mL/min. The change in production pressure with time is denoted in the legend. Temperature was kept constant at 3.0 ± 0.6 °C.

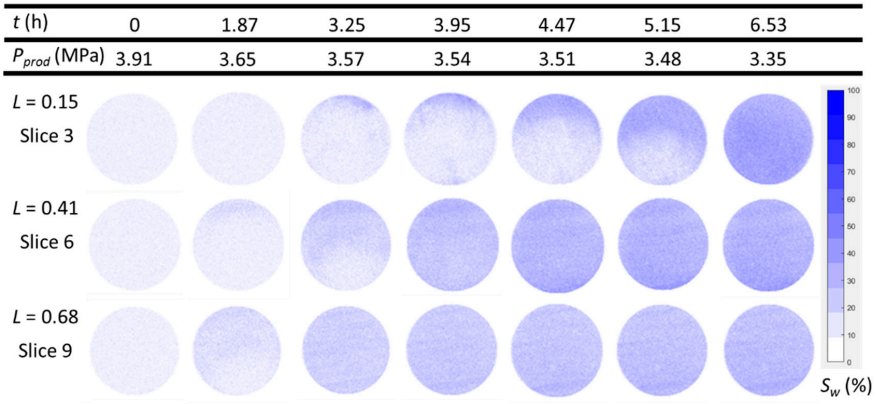

Figure 12. Water distribution in three different cross-sections of the core during hydrate dissociation in Exp. 1. Methane gas was produced with constant volumetric flow rate of 0.5 mL/min. The change in production pressure with time is denoted in the heading. Temperature was kept constant at 3.0 ± 0.6 °C.

Explicit mapping of the hydrate saturation was not possible during dissociation, in contrast to the growth process. The quantification of hydrate saturation during formation was based on the premise that all reduction in water saturation corresponded to formation of hydrate, not because of flow of water inside the core. This assumption is reasonable for hydrate growth at a constant pressure, but not for gas production at a constant flow rate. The final average water saturation after complete dissociation was 0.27 compared with the initial water saturation before hydrate formation, which was 0.31. Furthermore, 13% of the water originally in place was produced (into tubing) during the dissociation process.

Production of gas from one side of the core in Exp. 2 caused an immediate build-up of differential pressure across the core, and the effective gas permeability could not be measured. The average saturation of gas after hydrate formation was 0.36, contrary to Exp. 1 where the average gas saturation was 0.61. In some cross-sections of the core ($L < 0.3$), the gas saturation was close to zero. The pressure was thus reduced to 5.00 MPa from both ends of the core. The production of methane gas was then started by a constant volumetric flow rate of 1.0 mL/min from one side of the core ($L = 1$), and hydrate dissociation was triggered at the production side when the pressure reached 4.17 MPa (Figure 13). The dissociation front moved from the production side towards the other end of the core ($L = 0$). At the time when the production pressure reached 4.00 MPa and was set to a constant pressure, a differential pressure of 1.00 MPa was obtained and sustained while the hydrate continued to dissociate. The gas permeability of the core became measurable again three hours later when the dissociation front reached the end of the core ($t = 3.70$ h, Figure 13). The slow hydrate dissociation in the region with highest hydrate saturation ($L < 0.3$) demonstrates the impact of hydrate and gas saturation on the rate of methane recovery [6]. The dissociation was finished after approximately ten hours and left the core with an average water saturation of 0.30. Furthermore, 43% of the water originally in place was produced during the dissociation process.

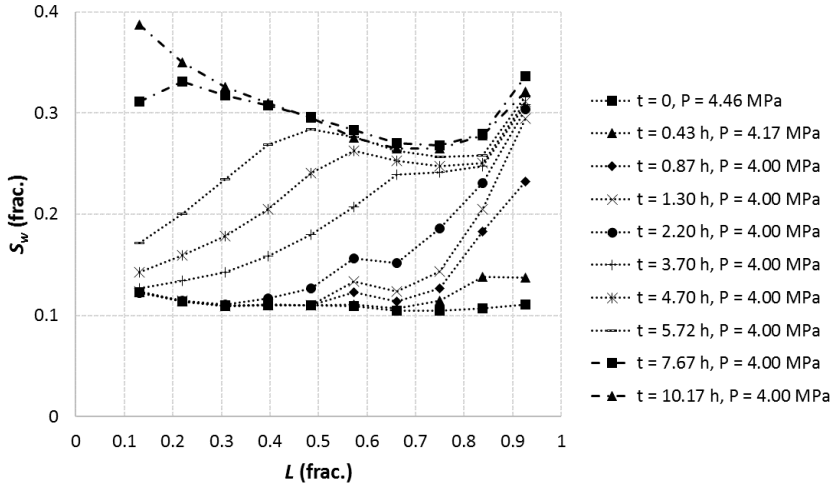

Figure 13. Water saturation profiles during hydrate dissociation in Exp. 2. Methane gas was initially produced with constant volumetric flow rate of 1.0 mL/min. The production pressure was set to constant when the pressure reached 4.00 MPa. Temperature was kept constant at 4.2 ± 0.5 °C.

The dissociation seemed to start at the perimeter of the core and proceeded radially inwards to the core center (Figure 14), similar to the pattern that was observed for thermally-induced hydrate dissociation [19]. The effect of heat transfer from the boundary of the core is believed to dictate the dissociation pattern. Gas expansion during production causes a depression of the core temperature. The temperature drop is less at the perimeter of the core close to the surrounding temperature control, contrary to the center of the core where the temperature drop is largest. The resulting temperature gradient with slightly elevated temperature at the perimeter of the core causes the hydrate dissociation to start at the boundary; for example, slice 9, Figure 14.

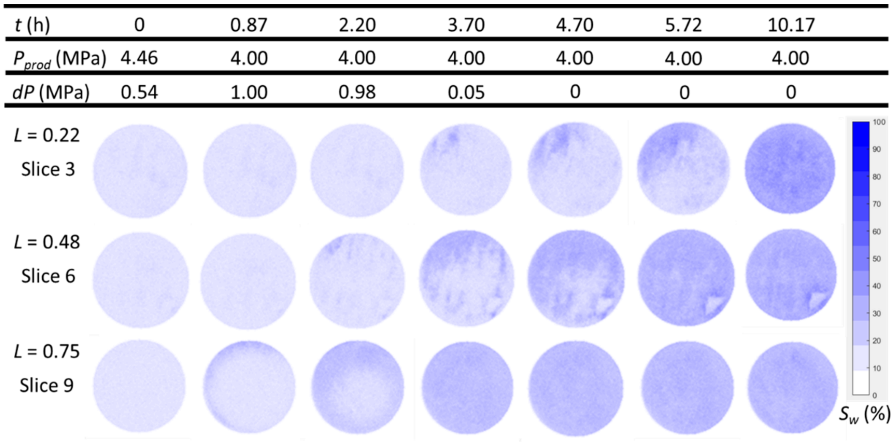

Figure 14. Water distribution in three different cross-sections of the core during hydrate dissociation in Exp. 2. Methane gas was initially produced with constant volumetric flow rate of 1.0 mL/min. The production pressure was set to constant when the pressure reached 4.00 MPa. The change in production pressure and differential pressure across the length of the core are denoted in the heading. Temperature was kept constant at 4.2 ± 0.5 °C.

The dissociation of hydrate was accompanied by an increase in average T_2 for every cross-section of the core in both experiments (Figures 15 and 16). The magnitude of the average T_2 was mainly a function of water saturation and was independent of the longitudinal location in the core. This means that the liberated water during dissociation had approximately the same surface-to-volume ratio throughout the length of the core. The water that was not produced out from the core during dissociation distributed itself towards pore walls with gas residing in the middle of the pores, giving a more uniform saturation of gas and water than prior to the hydrate formation. The formation and subsequent dissociation of hydrate is clearly an effective method to homogenize the fluid saturation in a core sample with heterogeneous initial fluid saturation.

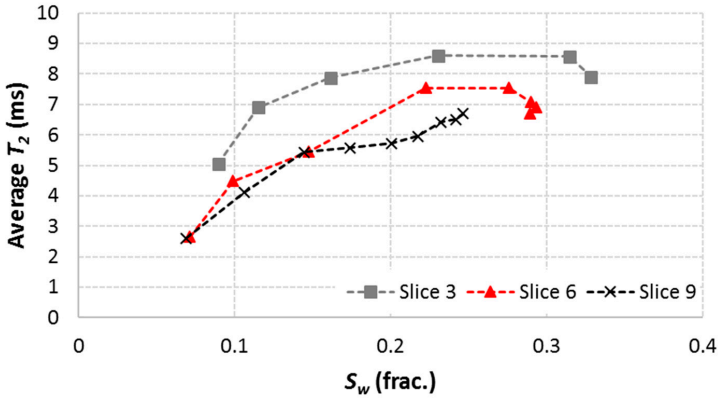

Figure 15. Average T_2 in three different cross-sections of the core during hydrate dissociation in Exp. 1.

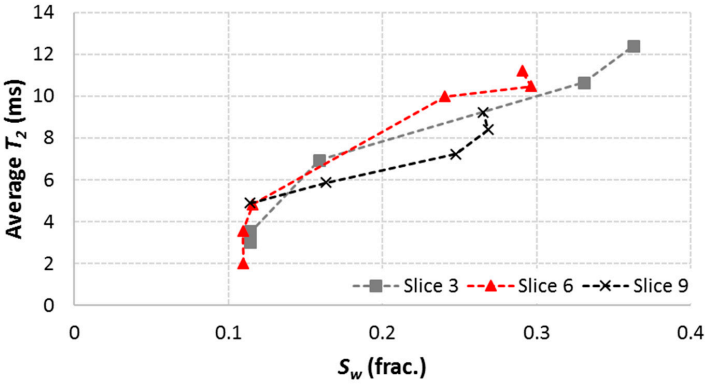

Figure 16. Average T_2 in three different cross-sections of the core during hydrate dissociation in Exp. 2.

4. Conclusions

Magnetic resonance imaging was successfully used to map the water saturation during methane hydrate formation and dissociation in Bentheim sandstone cores. The visualization showed that the growth of hydrate was more prominent in regions of the core with high water saturation. The final hydrate distribution was controlled by the initial water distribution, giving a uniform remaining water saturation of around 0.1 after hydrate formation. The average transverse relaxation time constant, T_2, decreased significantly during growth in high water saturation regions and remained unchanged during limited growth in low water saturation regions. Pressure depletion from one end of the core led to a dissociation front starting at the production side and moving through the length of the core.

The concomitant flow of water and gas during dissociation led to a final water saturation that was more uniform than the initial water saturation.

Author Contributions: Conceptualization, S.A., P.F. and G.E.; methodology, S.A., P.F. and G.E.; software, S.A., P.F. and G.E.; validation, S.A., P.F. and G.E.; formal analysis, S.A.; investigation, S.A.; resources, S.A., P.F. and G.E.; data curation, S.A., P.F. and G.E.; writing—original draft preparation, S.A.; writing—review and editing, S.A., P.F. and G.E.; visualization, S.A.; supervision, P.F. and G.E.; project administration, P.F. and G.E.; funding acquisition, P.F. and G.E.

Funding: This research was funded by Equinor through the Academia Agreement with the University of Bergen, Norway.

Acknowledgments: The authors would like to acknowledge Equinor for financial support and the use of the MRI facility at Equinor's laboratories in Bergen, Norway.

Conflicts of Interest: The authors declare no conflict of interest.

References

1. Milkov, A.V. Global Estimates of Hydrate-Bound Gas in Marine Sediments: How Much Is Really Out There? *Earth-Sci. Rev.* **2004**, *66*, 183–197. [CrossRef]
2. Ruppel, C.D.; Kessler, J.D. The Interaction of Climate Change and Methane Hydrates. *Rev. Geophys.* **2017**, *55*, 126–168.
3. Kurihara, M.; Sato, A.; Funatsu, K.; Ouchi, H.; Yamamoto, K.; Numasawa, M.; Ebinuma, K.; Narita, H.; Masuda, Y.; Dallimore, S.; et al. Analysis of Production Data for 2007/2008 Mallik Gas Hydrate Production Tests in Canada. In Proceedings of the International Oil and Gas Conference and Exhibition, Beijing, China, 8–10 June 2010.
4. Konno, Y.; Fujii, T.; Sato, A.; Akamine, K.; Naiki, M.; Masuda, Y.; Yamamoto, K.; Nagao, J. Key Findings of the World's First Offshore Methane Hydrate Production Test off the Coast of Japan: Toward Future Commercial Production. *Energy Fuels* **2017**, *31*, 2607–2616. [CrossRef]
5. Schoderbek, D.; Martin, K.L.; Howard, J.J.; Silpngarmlert, S.; Hester, K. North Slope Hydrate Fieldtrial: CO2/CH4 Exchange. In Proceedings of the OTC Arctic Technology Conference, Houston, TX, USA, 3–5 December 2012.
6. Almenningen, S.; Fotland, P.; Fernø, M.A.; Ersland, G. An Experimental Investigation of Gas-Production Rates During Depressurization of Sedimentary Methane Hydrates. *SPE J.* **2019**, *24*, 522–530. [CrossRef]
7. Kleinhans, M.G.; Jeukens, C.R.L.P.N.; Bakker, C.J.G.; Frings, R.M. Magnetic Resonance Imaging of Coarse Sediment. *Sediment. Geol.* **2008**, *208*, 69–78. [CrossRef]
8. Ersland, G.; Husebø, J.; Graue, A.; Baldwin, B.A.; Howard, J.J.; Stevens, J. Measuring Gas Hydrate Formation and Exchange with CO2 in Bentheim Sandstone Using MRI Tomography. *Chem. Eng. J.* **2010**, *158*, 25–31. [CrossRef]
9. Fernø, M.A.; Haugen, Å.; Wickramathilaka, S.; Howard, J.J.; Graue, A.; Mason, G.; Morrow, N.R. Magnetic Resonance Imaging of the Development of Fronts During Spontaneous Imbibition. *J. Petrol. Sci. Eng.* **2013**, *101*, 1–11.
10. Oswald, S.E.; Spiegel, M.A.; Kinzelbach, W. Three-Dimensional Saltwater-Freshwater Fingering in Porous Media: Contrast Agent MRI as Basis for Numerical Simulations. *Magn. Reson. Imaging* **2007**, *25*, 537–540. [CrossRef] [PubMed]
11. Zhao, J.; Lv, Q.; Li, Y.; Yang, M.; Liu, W.; Yao, L.; Wang, S.; Zhang, Y.; Song, Y. In-Situ Visual Observation for the Formation and Dissociation of Methane Hydrates in Porous Media by Magnetic Resonance Imaging. *Magn. Reson. Imaging* **2015**, *33*, 485–490. [CrossRef] [PubMed]
12. Baldwin, B.A.; Moradi-Araghi, A.; Stevens, J. Monitoring Hydrate Formation and Dissociation in Sandstone and Bulk with Magnetic Resonance Imaging. *Magn. Reson. Imaging* **2003**, *21*, 1061–1069. [CrossRef] [PubMed]
13. Baldwin, B.A.; Stevens, J.; Howard, J.J.; Graue, A.; Kvamme, B.; Aspenes, E.; Ersland, G.; Husebø, J.; Zornesb, D.R. Using Magnetic Resonance Imaging to Monitor CH4 Hydrate Formation and Spontaneous Conversion of CH4 Hydrate to CO2 Hydrate in Porous Media. *Magn. Reson. Imaging* **2009**, *27*, 720–726. [CrossRef] [PubMed]

14. Graue, A.; Kvamme, B.; Baldwin, B.; Stevens, J.; Howard, J.J.; Aspenes, E.; Ersland, G.; Husebo, J.; Zornes, D. MRI Visualization of Spontaneous Methane Production From Hydrates in Sandstone Core Plugs When Exposed to CO_2. *SPE J.* **2008**, *13*, 146–152. [CrossRef]
15. Ramstad, T.; Rueslåtten, H. *Pore Scale Numerical Analysis for Geological Sequestration of CO_2*; Technical Report from Task 1, 1–63; Numerical Rocks: Trondheim, Norway, 2013.
16. Mitchell, J.; Chandrasekera, T.C.; Johns, M.L.; Gladden, L.F.; Fordham, E.J. Nuclear Magnetic Resonance Relaxation and Diffusion in the Presence of Internal Gradients: The Effect of Magnetic Field Strength. *Phys. Rev. E* **2010**, *81*, 026101. [CrossRef] [PubMed]
17. Almenningen, S.; Flatlandsmo, J.; Fernø, M.A.; Ersland, G. Multiscale Laboratory Verification of Depressurization for Production of Sedimentary Methane Hydrates. *SPE J.* **2017**, *22*, 138–147. [CrossRef]
18. Circone, S.; Kirby, S.H.; Stern, L.A. Direct Measurement of Methane Hydrate Composition along the Hydrate Equilibrium Boundary. *J. Phys. Chem. B* **2005**, *109*, 9468–9475. [CrossRef] [PubMed]
19. Bagherzadeh, S.A.; Moudrakovski, I.L.; Ripmeester, J.A.; Englezos, P. Magnetic Resonance Imaging of Gas Hydrate Formation in a Bed of Silica Sand Particles. *Energy Fuels* **2011**, *25*, 3083–3092. [CrossRef]
20. Seol, Y.; Kneafsey, T.J. Methane Hydrate Induced Permeability Modification for Multiphase Flow in Unsaturated Porous Media. *J. Geophys. Res. Solid Earth* **2011**, *116*, 1–15. [CrossRef]
21. Almenningen, S.; Iden, E.; Fernø, M.A.; Ersland, G. Salinity Effects on Pore-Scale Methane Gas Hydrate Dissociation. *J. Geophys. Res. Solid Earth* **2018**, *123*, 5599–5608. [CrossRef]
22. Clennell, M.B.; Hovland, M.; Booth, J.S.; Henry, P.; Winters, W.J. Formation of Natural Gas Hydrates in Marine Sediments: 1. Conceptual Model of Gas Hydrate Growth Conditioned by Host Sediment Properties. *J. Geophys. Res. Solid Earth* **1999**, *104*, 22985–23003.
23. Chaouachi, M.; Falenty, A.; Sell, K.; Enzmann, F.; Kersten, M.; Haberthür, D.; Kuhs, W.F. Microstructural Evolution of Gas Hydrates in Sedimentary Matrices Observed with Synchrotron X-Ray Computed Tomographic Microscopy. *Geochem. Geophys.* **2015**, *16*, 1711–1722. [CrossRef]
24. Colorado School of Mines. Center for Hydrate Research. 2015. Available online: http://hydrates.mines.edu/CHR/Software.html (accessed on 2 March 2016).

II

Journal of Geophysical Research: Solid Earth

RESEARCH ARTICLE
10.1029/2017JB015345

Special Section:
Gas Hydrate in Porous Media: Linking Laboratory and Field Scale Phenomena

Salinity Effects on Pore-Scale Methane Gas Hydrate Dissociation

Stian Almenningen[1], Eirik Iden[1], Martin A. Fernø[1], and Geir Ersland[1]

[1]Department of Physics and Technology, University of Bergen, Bergen, Norway

Key Points:
- Micromodel pore-level visualization was used to study methane gas hydrate dissociation in sediments
- A conceptual model of methane gas hydrate dissociation based on new experimental pore-scale data is presented
- Pore water salinity resulted in multiple dissociation pressures due to local pore water freshening during methane gas hydrate dissociation

Correspondence to:
M. A. Fernø,
martin.ferno@ift.uib.no

Citation:
Almenningen, S., Iden, E., Fernø, M. A., & Ersland, G. (2018). Salinity effects on pore-scale methane gas hydrate dissociation. *Journal of Geophysical Research: Solid Earth*, *123*, 5599–5608. https://doi.org/10.1029/2017JB015345

Received 28 DEC 2017
Accepted 5 JUN 2018
Accepted article online 20 JUN 2018
Published online 25 JUL 2018

Abstract Methane gas hydrate may become a significant source of methane gas in the global energy mix for the next decades. The widespread distribution of methane gas hydrate, primarily in subsea sediments on continental margins, makes the crystalline compound attractive for countries with shorelines that seek self-sustainable energy. Fundamental understanding of pore-level methane gas hydrate distribution and dissociation pattern in reservoirs is important to anticipate the methane production rate and overall efficiency. Specifically, the local salinity gradients occurring during methane gas hydrate dissociation, and its impact on local dissociation characteristics, must be understood as the aqueous phase in most reservoirs is saline. We experimentally evaluate the salinity effect on methane gas hydrate dissociation using high-pressure silicon-wafer micromodels with realistic sandstone grain characteristics. Methane gas hydrate was formed for a range of brine salinities (0–5 wt% NaCl), and we report variations in dissociation patterns during depressurization and thermal stimulation as a function of brine salinity. A strong correlation between initial methane gas hydrate distribution and dissociation characteristic, and subsequent release and mobilization of methane gas, was observed. Local water salinities affected the methane gas hydrate structure leading to distinct dissociation patterns of self-preservation due to water freshening.

Plain Language Summary Methane gas hydrates have the potential to become the next big energy resource, and high-end estimates suggest an energy equivalent to conventional fossil fuels combined. The potential in full-scale commercialization drives research and industry to better understand hydrates in natural sedimentary systems, and several short-term field pilots investigating production by depressurization have been undertaken the last decades. This study investigates the link between brine salinity and hydrate melting inside the microsized pores in sedimentary rocks where the hydrates occur.

1. Introduction

Methane gas hydrate has the potential to become the next big energy resource. Estimates vary between 10^{14} and 10^{18} Sm^3 of methane gas compressed within methane gas hydrate in the Earth (Milkov, 2004), either in regions of permafrost or in subsea sediments below water columns of at least 400 m. The high-end estimates suggest an energy content equivalent to conventional fossil fuels combined (Kvenvolden, 1988). The environmental impact of consumption of methane gas is less than the other fossil fuels as methane gas produce less carbon dioxide (CO_2) upon combustion compared to oil and coal (U.S. EIA, 2017). Proposed gas production schemes are commonly based on methane gas hydrate dissociation—by either depressurization, thermal stimulation, injection of chemical inhibitors, or a combination of these (Moridis et al., 2011). We have previously demonstrated an alternative strategy for replacement of methane molecules in hydrate with CO_2 (Graue et al., 2008; Kvamme et al., 2007), which later resulted in a field trial on the North Slope of Alaska where more than half of the injected CO_2 was sequestered in the reservoir (Schoderbek et al., 2012). Carbon dioxide is the thermodynamically preferred guest molecule and this production scheme enables an option for carbon capture, utilization and storage. Still, methane gas production by depressurization of sedimentary basins with methane gas hydrate is the most attractive methodology because it does not require fluid injection. The potential in full-scale commercialization drives research and industry to better understand methane gas hydrate in natural sedimentary systems and several short-term field pilots investigating gas production by depressurization has been undertaken the last decades both onshore (Collett, 2008) and offshore (Yamamoto et al., 2014). One concern related to depressurization as a production method is the reduced fluid flow by reformation of gas hydrate (and formation of ice) during the endothermic dissociation process (Moridis et al., 2007). The stability of methane gas hydrate is also influenced by brine salinity, with a reduction in dissociation temperature (Dickens & Quinby-Hunt, 1994) and methane solubility

with increasing salinity (Tishchenko et al., 2005). Submarine sediments in vicinity of salt diapirs and mud volcanos exhibit heterogeneous methane gas hydrate distributions caused by spatial variations in heat and mass transfer, brine salinities, and gas compositions (Ruppel et al., 2005). The overall effect of pore-level salinity changes on gas hydrate dissociation patterns and subsequent fluid mobilization in sediments are not well described. Salt is not included when water molecules take part in the gas hydrate structure, and gas hydrate reservoirs will likely contain water pockets with varying degree of salinity. In turn, freshwater released from gas hydrate dissociation will yield local salinity gradients that will work as a self-preservation mechanism.

This study investigates the nature of pore-level methane gas hydrate dissociation influenced by changes in brine salinity. Growth and dissociation of gas hydrate have previously been studied at the pore-scale using micromodels (Almenningen et al., 2017; Hauge et al., 2016; Katsuki et al., 2007; Tohidi et al., 2001), but only with guest molecules (methane or CO_2) interacting with distilled water. We present real-time observations of pore-level methane hydrate in equilibrium with methane gas and brines with varying salinity. Different dissociation patterns arising from thermal stimulation and depressurization are discussed, with emphasize on the role of salinity on methane gas hydrate dissociation behavior.

2. Methodology

2.1. Porous Material

The porous media used was a silicon micromodel (Figure 1), where a glass plate (silica, SiO_2) was anodically bonded to an etched silicon wafer. Pore shape and size were based on thin-section analysis and resembled pore network in quartz sandstone with an average pore diameter of approximately 100 μm. A constant vertical height (25 μm) and sharp edges were achieved with deep reactive ion etching. Reproduction of actual pore bodies, pore necks, and coordination numbers made the model suitable for flow and equilibria studies related to natural sediments (Song et al., 2014). The wettability of the solid grains was strongly water-wet because of the anodic bonding procedure (Buchgraber et al., 2012). The water-wet nature of grains induced a curved interface between water and gas (Figure 1) and made it possible to differentiate between fluid phases. Segmented images were used to calculate two-dimensional fluid saturations, but pixel counting does not necessarily reflect the true volumetric saturation in the pore space because multiple phases can coexist in the same location in the vertical depth of 25 μm (Almenningen et al., 2017b). Pixel counting assumes that each pixel is saturated with only one fluid phase and is an approximation to the volumetric saturation.

2.2. Experimental Procedure

The rectangular micromodel has ports for injection/production in each corner and was mounted in a holder to connect high-pressure pumps through nanotube polyether ether ketone fittings (Figure 1). A water pump was connected to one port, and a methane gas pump was connected to a port in the opposite corner, whereas the two remaining ports were used for venting. The initially air-filled pore space was flushed with water to displace air and fill all pores with water, before methane gas was injected at ambient conditions (room temperature and 1 bar) to establish a gas saturation of ~0.50 (confirmed visually). The pore pressure was then increased to 83 bar by injecting methane gas keeping the remaining ports closed. Increasing the pore pressure using the gas pump ensured that no water was located in the flow line prior to hydrate formation and injectivity impairment because of hydrate plugging was avoided. The pore pressure was kept at 83 bar for 24 hr to fully saturate the pore water with dissolved methane and verify a sealed system. Methane gas hydrate formation was then triggered by reducing the temperature to 4 °C using a dual chamber: antifreeze liquid was circulated in an insulated, outer chamber adjacent to the inner chamber where the micromodel was submerged in stagnant distilled water. The temperature was monitored continuously with a temperature sensor located directly below the model. Pore-level images were recorded with a camera connected to a microscope, with optical access through the still water and the transparent glass plate on top of the pore network.

Methane gas hydrate growth started usually within 24 hr after the pressure and temperature were set or was otherwise triggered by a temporary flow of methane gas through the model. This temporary agitation resulted in methane gas hydrate growth within minutes after the system returned to static conditions (constant pressure, no flow). When no further methane gas hydrate formation was observed (generally

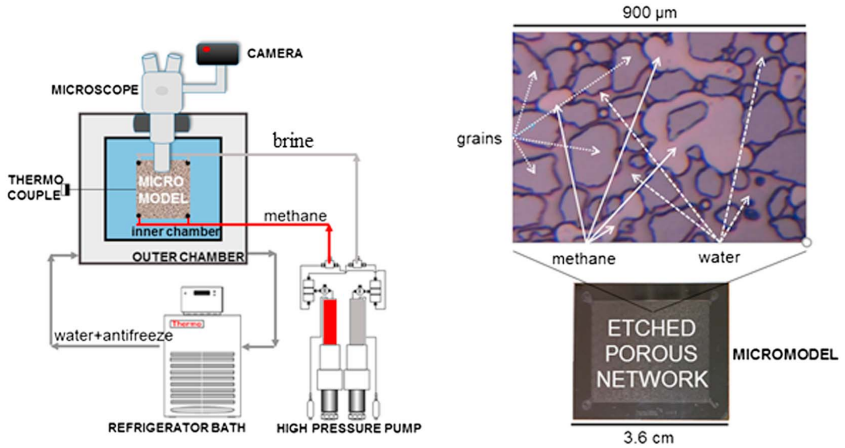

Figure 1. Experimental setup (left) and close-up image of micromodel saturated with water and gas (right; Almenningen et al., 2017).

after 24–48 hr from initial growth was observed), the pore pressure was stepwise reduced by retracting the piston in the methane gas pump. The pore pressure was set to 10 bar above the expected dissociation pressure and then decreased in decrements of 0.7 bar; each reduction step in pressure was followed by several hours of constant pressure to identify methane gas hydrate dissociation and phase changes. The pore pressure was decreased until complete methane gas hydrate dissociation was achieved. This stepwise pressure reduction procedure was applied for brines with different salinities: 0.0, 2.0, 3.5, and 5.0 wt% NaCl. In some tests, the methane gas hydrate dissociation was triggered by increasing the temperature to investigate differences in pore-level methane gas hydrate dissociation between pressure- and temperature-induced dissociation.

3. Results and Discussion

3.1. Methane Gas Hydrate Dissociation With Distilled Water

The dynamics of methane gas hydrate dissociation during depressurization correlated strongly to the initial pore-scale hydrate distribution, which was determined by the former hydrate formation pattern (see conceptual model in Figure 2). Grain surfaces in the micromodel are coated with a thin water layer, for both gas- and hydrate-filled pores, due to the water-wet nature of the pore network. The water accumulation was larger in the pore corners where the capillary force was high due to geometry. Methane gas hydrate growth typically started in the pore corners because brine and methane gas were readily available there; see Figure 2. Two methane gas hydrate growth patterns were observed: shell-like growth along the gas-water interface resulting in a porous hydrate with encapsulated methane gas in a shell of methane gas hydrate (column a, Figure 2) or crystalline growth where all the free methane gas was consumed and the pore was filled with solid nonporous methane gas hydrate (column b, Figure 2). The resulting hydrate configuration (porous or nonporous) was inferred from color analysis of the hydrate phase (Almenningen et al., 2017b). The former shell-type growth was most frequently observed, with methane gas inside the methane gas hydrate shell, presumably because of lack of water transport across the hydrate shell and/or insufficient pressure in the gas phase to maintain further growth (Almenningen et al., 2017a; Peng et al., 2007). The methane gas hydrate layer thickness varied accordingly and seemed to depend on mass transfer of water across the hydrate layer at the gas-water interface; isolated gas bubbles in small pores were more likely converted to nonporous hydrate than isolated gas bubbles in large pores. The thickness of the resulting methane gas hydrate layer could not be quantified due to insufficient resolution. For comparison, the thickness of a gas hydrate layer growing on a planar interface between water and gas is estimated to be 10–20 μm at given pressure and temperature

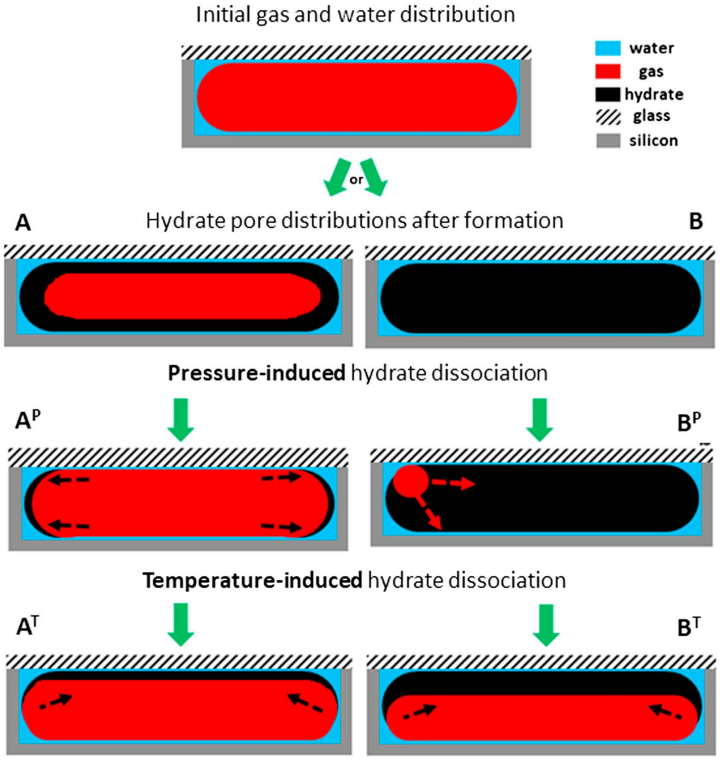

Figure 2. Conceptual model (not to scale) of pore-level methane gas hydrate growth and dissociation by depressurization or thermal stimulation. Each image represents a cross section of an average pore with diameter 100 μm. The pore is initially filled with methane gas surrounded by a water film coating the water-wet solid boundaries. When methane gas hydrate forms, growth initiates in the corners due to availability of water. Further growth follows the gas-water interface until the methane gas is either encapsulated (a) or consumed (b). (a^P) Dissociation of shell-like methane gas hydrate by depressurization starts in the middle of pores (seen from above) where the methane gas hydrate layer is thin. The dissociation pattern follows a reverse growth evolution and terminates in the pore corners. (b^P): Dissociation of nonporous methane gas hydrate surrounded by a water film by depressurization starts in the pore corners because the pressure reduction propagates through the water accumulated there. The gas bubble expands as methane gas hydrate dissociation continues. (a^T and b^T) Dissociation of methane gas hydrate by thermal stimulation starts at the bottom (floor) and sides (wall) of the pore space due to the favorable heat conductivity offered by the silicon wafer compared to the glass plate on top (roof). Methane gas hydrate dissociates from the grain walls and inward (seen from above) to the pore center.

(Mochizuki & Mori, 2006). A thin water layer (5–50 nm) was probably present between the grains and the formed hydrate shell because of the low water activity of grain-coating water (Clennell et al., 1999).

During depressurization of porous methane gas hydrate, the pressure response transmitted through the gas phase and liberated gas from gas hydrate dissociation could escape via the connected gas phase. The porous gas hydrate started to dissociate in the pore center (column a, Figure 2) resulting in a dissociation pattern moving from pore center to pore walls (see Figure 3a). If, however, all of the methane gas was consumed during methane gas hydrate growth, resulting in nonporous gas hydrate filling the pores (column b, Figure 2), the methane gas hydrate dissociation started close to the pore corners. In this case, the pressure response was transmitted through the water phase in the pore corners and liberated methane gas first appeared close to grains (see Figure 3b). The methane gas bubble grew as the nonporous methane gas hydrate dissociated and was eventually mobilized when the methane gas hydrate saturation had decreased to the extent where gas formed a critical saturation.

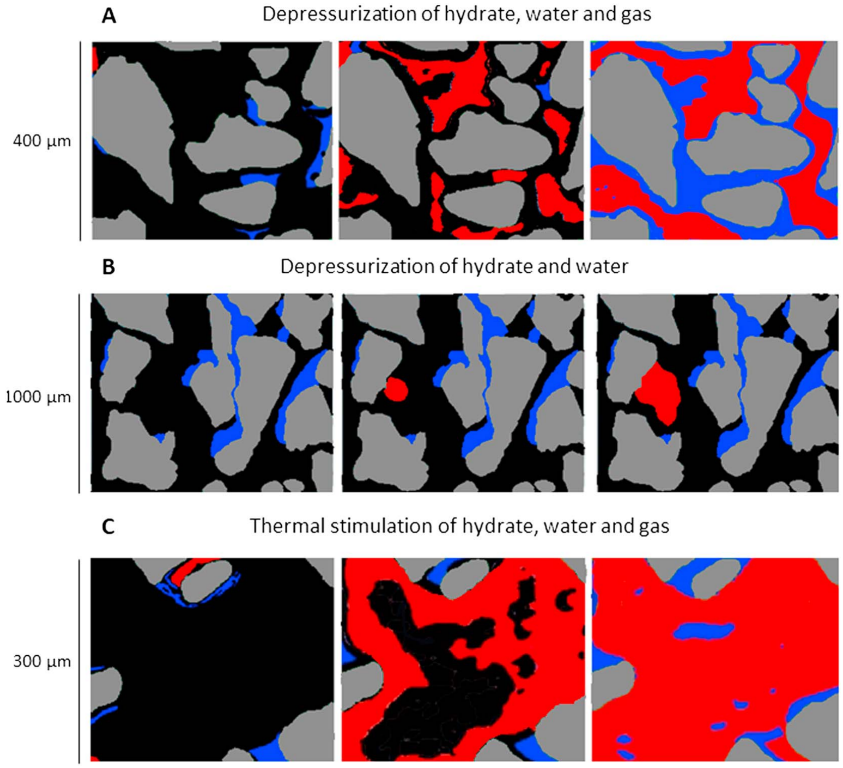

Figure 3. Comparison of methane gas hydrate dissociation induced by depressurization (a and b) and thermal stimulation (c) with distilled water. Silicon grains are gray, methane gas is red, water is blue, and hydrate is black. (a) Hydrate dissociation by decreasing the pressure from 43.5 to 38.3 bar at constant temperature 4.0 °C. Porous hydrate started to dissociate in the pore center and moved toward the grain walls. (b) Nonporous hydrate dissociation by decreasing the pressure from 42.0 to 39.0 bar at constant temperature 4.1 °C. A methane gas bubble first appeared adjacent to the grain wall. (c) Hydrate dissociation by increasing the temperature from 7.0 to 8.2 °C at constant pressure 60 bar. Hydrate started to dissociate close to grains and continued toward the center of pores.

A third methane gas hydrate dissociation pattern was observed during thermal stimulation resulting from the favorable heat transfer close to grains. The heat conductivity of silicon (pore floor and wall) is higher than the heat conductivity of silica glass (pore roof); see Figure 4. Methane gas hydrate dissociation started at the pore floor and the vertical grain walls (bottom row, Figure 2) and moved toward the center and pore roof (Figure 3c). The methane gas hydrate layer at the gas-water interface close to the roof required more time to equilibrate the temperature compared to pore floor and walls, leading to slower dissociation.

3.2. Effect of Salinity on Methane Gas Hydrate Dissociation

Salt ions are not included in the methane gas hydrate structure and remain in the liquid water phase during formation. This local increase in water salinity inhibit further hydrate formation and leads to high-saline water pockets within the gas hydrate saturated porous media (Wright & Dallimore, 2004). The salinity gradient between high-saline water pockets and surrounding water will equilibrate with time through film flow and ion diffusion in the continuous water phase wetting the grains. In systems with fixed amount of brine, the salinity of liquid water after gas hydrate formation is higher than the initial brine salinity, as the total

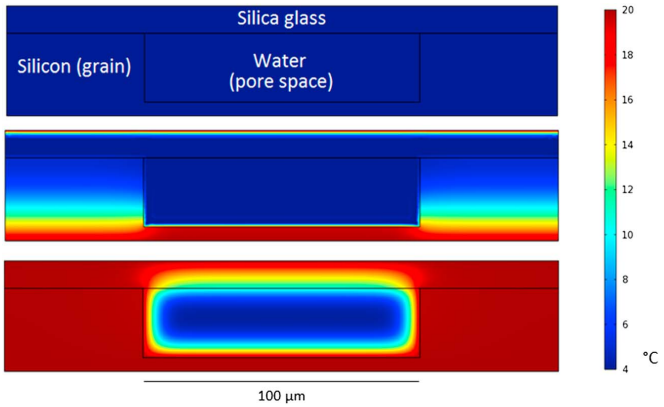

Figure 4. Numerical simulation of heat propagation in a water-filled pore (Comsol Multiphysics). The system is initially at 4 °C and is heated by the surroundings at constant temperature 20 °C. The simulation shows that the pore space is heated from below and from the sides (silicon wafer has a higher heat conductivity than silica glass) and supports the proposed dissociation schematic in Figure 2. The simulation does not include hydrate phase dynamics nor temperature-induced convection of the water phase.

amount of liquid water decreases during hydrate growth and the total amount of salt is constant. However, because the pore volume (in the order of µl) was much less compared to the brine-filled tube volume (in the order or ml) connected to the model, allowing ions to equilibrate in the large water volume, the average salinity-increase in the pore water is reduced. This assumption was evaluated in a series of depressurization tests with different initial brine salinities (2.0, 3.5 and 5.0 wt% NaCl). With 5.0 wt% initial brine salinity at 3.9 °C, the methane gas hydrate started to dissociate at 49.1 bar (Figure 5), which corresponds to a salinity of 5.6 wt% NaCl according to CSMgem (Colorado School of Mines, 2015).

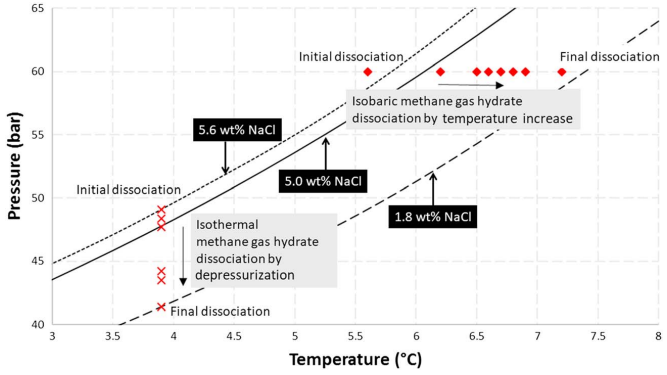

Figure 5. Comparison between simulated (Colorado School of Mines, 2015) and experimentally observed methane gas hydrate dissociation when formed with initial brine salinity of 5.0 wt% NaCl. Simulation of three salinities are shown (5.6, 5.0, and 1.8 wt% NaCl) and methane gas hydrate is stable above these lines at the corresponding salinity. Experimental methane gas hydrate dissociation by depressurization (red crosses) required 11 additional pressure reduction steps (each 0.7 bar) after initial dissociation at 49.1 bar, corresponding to a salinity of 5.6 wt% NaCl. Only the pressure steps where dissociation was observed are shown. Final dissociation during depressurization was observed at 41.4 bar, corresponding to a salinity of 1.8 wt% NaCl. Similarly, experimental methane gas hydrate dissociation by temperature increase (red diamonds) required seven additional temperature increase steps after initial dissociation at 5.6 °C, corresponding to a salinity of 6.1 wt% NaCl. Final dissociation during temperature increase was observed at 7.2 °C, corresponding to a salinity of 2.5 wt% NaCl.

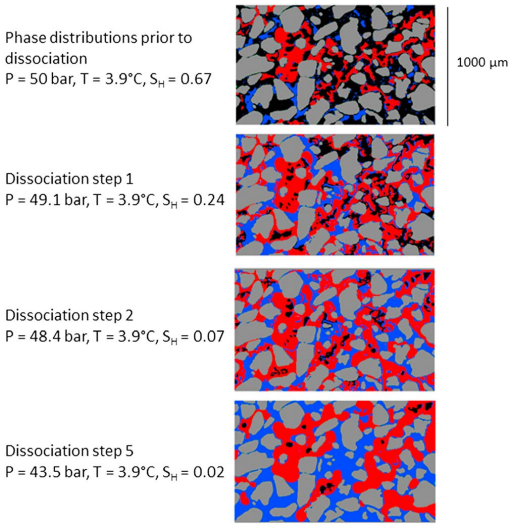

Figure 6. Methane gas hydrate dissociation by depressurization with 5.0 wt% NaCl initial brine salinity at 3.9 °C. Silicon grains are colored gray, methane gas is red, brine is blue, and hydrate is black. The methane gas hydrate saturation was 0.67 prior to initial dissociation, with methane gas and brine present in the pore space. Initial dissociation started at 49.1 bar, corresponding to a brine salinity of 5.6 wt% NaCl (Colorado School of Mines, 2015), and reached a stable methane gas hydrate saturation of 0.24 after 26 min. After 60 min with constant saturation, the pressure was reduced to 48.4 bar and the methane gas hydrate saturation was reduced to 0.07. The system was again kept at constant pressure for 1 h without further phase changes. Reducing the pressure 0.7 bar at the time led to small hydrate saturation reductions at each pressure step. When the pressure was lowered to 43.5 bar, the hydrate saturation had contracted to 0.02. All the hydrate dissociated with a pore pressure of 41.4 bar, 7.7 bar below the initial dissociation pressure.

Similarly, during temperature-induced dissociation, the methane gas hydrate dissociation temperature was 5.6 °C at 60 bar at 5.0 wt% NaCl initial brine salinity (Figure 5), corresponding to 6.1 wt% NaCl salinity (Colorado School of Mines, 2015). These observations confirm the assumption of a slight increase in salinity during hydrate formation in our system.

Only a fraction of the methane gas hydrate dissociated during the initial pressure reduction (or temperature increase) below equilibrium. Further depressurization (or thermal stimulation) steps were needed to completely dissociate the methane gas hydrate (Figure 5). The number of depressurization steps needed for complete dissociation increased with increasing initial brine salinity. The liberated water from the initial methane gas hydrate dissociation caused pore water freshening that lowered the hydrate phase equilibrium line, and further pressure reduction was needed to recommence dissociation. Each pressure reduction (or temperature increase) step was allowed to equilibrate for 1 hr before further pressure reduction, leading to a drawdown of the stability pressure for all salinity values investigated (see example of initial salinity of 5.0 wt% NaCl in Figure 5). With uniform brine salinity in the pore space, achieved through slow salt diffusion in the thin water films, the expected result is complete dissociation when the pressure is set slightly below the stability pressure corresponding to the initial brine salinity. However, final dissociation was not observed until the pressure was reduced to 41.4 bar, corresponding to a salinity of 1.8 wt% NaCl (CSMgem, Colorado School of Mines, 2015). Hence, the kinetics of salt diffusion was clearly not adequate to counteract temporary salt contrasts in the water phase during dissociation using this approach.

The methane gas hydrate that dissociated at the final pressure step was always located in the middle of pores with brine of initial salinity 5.0 wt% NaCl (Figure 6), in contrast to distilled water (Figure 3). This suggests that the multiple dissociation pressures needed to completely dissociate the methane gas hydrate in Figure 6 during depressurization, where methane hydrate surrounded by water dissociated at a higher pressure compared with methane hydrate surrounded by methane gas, are due to pore water freshening and not local endothermic effects. In fact, previous methane gas hydrate depressurization experiments with distilled water show that the rate of dissociation is higher when hydrate is surrounded by gas because of increased mobility of the liberated gas (Almenningen et al., 2017b). In addition, the observed dissociation pattern is influenced by surface roughness on the pore floor, where discrete brine droplets resided below the methane gas phase after drainage (Figure 7). When the methane gas hydrate, formed at the gas/water interface at these sites, dissociated, water freshening led to self-preservation due to local reduction in salinity and thereby decreased local dissociation pressure. The drawdown of the dissociation pressure and the change in dissociation pattern are therefore believed to be caused by temporary salinity differences.

Local gas hydrate reformation was observed during dissociation of methane gas hydrate formed with brine salinities above zero (Figure 8) and is believed to be promoted by local salinity gradients. Simultaneous dissociation and reformation were not observed with distilled water in this depressurization scheme (Figure 3), suggesting that the endothermic absorbed heat during dissociation was insufficient to initiate reformation of hydrate when salt was not present. Observed reformation of hydrate during stepwise depressurization with saline brine was likely caused by salinity gradients. Dissociation of solid methane gas hydrate induced gas and water flow in the pore network, leading to reconfiguration of the saturation distribution (red rectangle in Figure 8), where mobilized gas invaded water-filled pores followed by rapid local methane gas hydrate growth. The existence of salinity gradients resulted in a broadening of the hydrate stability region (Wright & Dallimore, 2004), and temporarily growth could occur in pores filled with low salinity water. The reformed

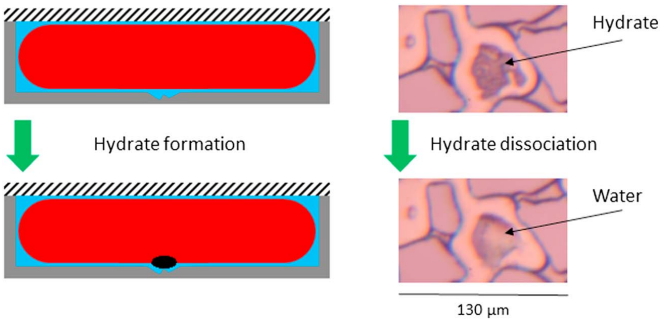

Figure 7. Effect of salinity and surface roughness on methane gas hydrate dissociation during depressurization at 3.9 °C. (left) Conceptual model (not to scale) of methane gas hydrate growth from brine located in the roughness in the pore floor. Grain walls are gray, gas is red, water is blue, hydrate is black, and the glass plate on top in stripes. (right) Unsegmented images of methane gas hydrate dissociation in the pore center of a gas-filled pore. The ion content of the center water film in equilibrium with the hydrate layer is continuously decreasing as the hydrate layer dissociates and the local dissociation pressure decreases accordingly. The water film thickness decreases over time as the water drains laterally, and the brine salinity in the film increases slowly as salt ions diffuse from surrounding brine.

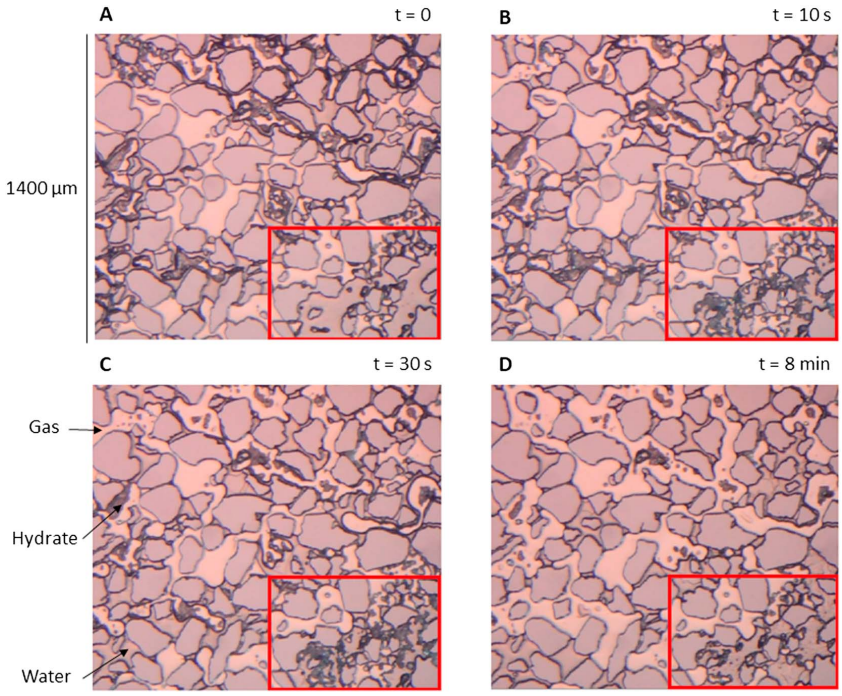

Figure 8. Local reformation of methane gas hydrate during dissociation by depressurizaton. Pressure and temperature were set to 41.6 bar and 4.2 °C, and the initial water salinity prior to hydrate formation was 3.5 wt% NaCl. (a) Dissociation occurs immediately after the pressure was lowered to 41.6 bar. (b, c) The hydrate saturation decreases globally in the field of view, except from in the lower right corner (red rectangle), where methane gas hydrate reformation is observed. (d) The reformed hydrate dissociates after approximately 8 min.

methane gas hydrate dissociated several minutes later after the concentration of salt ions had locally increased to the same value as the rest of the water in the pore space.

3.3. Key Observations and Implications

This paper reports pore-scale mechanisms that clarify hydrate dissociation patterns and how fluids are mobilized in hydrate-bearing sediments with saline pore water. The provided results emphasize the importance of salinity modeling to increase the accuracy of production forecasting by numerical simulation. The production of methane gas will be delayed or reduced as the phase line shifts when the salinity of the pore water decreases. Hydrate reformation will take place during production when liberated gas reforms to hydrate when contacting water of lower salinity. The field-scale consequence of the effect of self-preservation due to pore water freshening is that more time would be required for full dissociation and methane production from hydrate reservoirs. The effect of self-preservation and salinity gradients will depend on the initial pore water salinity and likely the geological setting but should be considered in the development of gas hydrate deposits. Especially the start of hydrate dissociation will be affected when the pressure is only slightly below the stability pressure, and at the same time the hydrate saturation is high and mobility of fluids is low. The preservation effect due to pore water freshening will not be as significant if the production pressure is set substantially below the equilibrium pressure. However, reformation of hydrate may also be triggered by the endothermic nature of the dissociation process. A field-scale gas production system from hydrate-bearing sediments would lead to temperature gradually cooling in the near-wellbore region where the pressure drop is highest, which may cause the secondary hydrate formation to begin near the production well and reduce the well productivity. The effect of self-conservation requires an increase in temperature and a decrease in well pressure, which can further enhance rock failure and sand production (Makogon & Ghassemi, 2010). An optimal gas production rate during depressurization should balance the effect of both hydrate reformation from temperature depression and reformation of hydrate caused by pore water freshening, and at the same time be compatible with the geological constraints affecting the degree of sand production and well integrity.

4. Conclusions

1. A conceptual model of pore-scale hydrate growth and dissociation is developed. The resulting dissociation pattern was dependent on the initial hydrate distribution. Two distinct methane hydrate morphologies were observed: (1) porous methane gas hydrate shells with encapsulated gas and (2) nonporous crystalline methane hydrate.
2. Methane gas hydrate formed with brine (NaCl) dissociated over a range of pressure and temperature steps, and the number of required depressurization steps from initial hydrate dissociation to complete hydrate dissociation increased with increased initial brine salinity.
3. The effect of self-preservation due to pore water freshening contributes to the stability of gas hydrate in porous media and increases the energy needed for methane production through depressurization and thermal stimulation schemes.
4. Reformation of methane gas hydrate was observed during dissociation and seemed to be promoted in saline systems due to local salinity gradients.

Acknowledgments
The authors would like to acknowledge Equinor for financial support and the Academia-agreement between University of Bergen and Equinor. Experimental data are available at http://doi.org/10.5281/zenodo.1216586.

References

Almenningen, S., Flatlandsmo, J., Fernø, M. A., & Ersland, G. (2017a). *Direct pore-level visualization of methane hydrate growth in an authentic sandstone replicate*. Paper presented at the Proceedings of the 9th International Conference on Gas Hydrates, Denver, CO.

Almenningen, S., Flatlandsmo, J., Fernø, M. A., & Ersland, G. (2017b). Multiscale laboratory verification of depressurization for production of sedimentary methane hydrates. *SPE Journal*, *22*(01), 138–147. https://doi.org/10.2118/180015-PA

Almenningen, S., Flatlandsmo, J., Kovscek, A. R., Ersland, G., & Ferno, M. A. (2017). Determination of pore-scale hydrate phase equilibria in sediments using lab-on-a-chip technology. *Lab on a Chip*, *17*(23), 4070–4076. https://doi.org/10.1039/C7LC00719A

Buchgraber, M., Castanier, L. M., & Kovscek, A. R. (2012). *Microvisual investigation of foam flow in ideal fractures: Role of fracture aperture and surface roughness*. Paper presented at the SPE Annual Technical Conference and Exhibition, San Antonio, TX. SPE-159430-MS. https://doi.org/10.2118/159430-MS

Clennell, M. B., Hovland, M., Booth, J. S., Henry, P., & Winters, W. J. (1999). Formation of natural gas hydrates in marine sediments: 1. Conceptual model of gas hydrate growth conditioned by host sediment properties. *Journal of Geophysical Research*, *104*(B10), 22,985–23,003. https://doi.org/10.1029/1999JB900175

Collett, T. S. (2008). *Geology of marine gas hydrates and their global distribution*. Paper presented at the offshore technology Conference, Houston, TX. OTC-19241-MS. https://doi.org/10.4043/19241-MS

Colorado School of Mines (2015). Center for Hydrate Research, hydrate simulator CSMGem. Retrieved from http://hydrates.mines.edu/CHR/Software.html, Accessed March 2, 2016.

Dickens, G. R., & Quinby-Hunt, M. S. (1994). Methane hydrate stability in seawater. *Geophysical Research Letters*, *21*(19), 2115–2118. https://doi.org/10.1029/94GL01858

Graue, A., Kvamme, B., Baldwin, B., Stevens, J., Howard, J. J., Aspenes, E., et al. (2008). MRI visualization of spontaneous methane production from hydrates in sandstone Core plugs when exposed to CO_2. *SPE Journal*, *13*(02), 146–152. https://doi.org/10.2118/118851-PA

Hauge, L. P., Gauteplass, J., Høyland, M. D., Ersland, G., Kovscek, A., & Fernø, M. A. (2016). Pore-level hydrate formation mechanisms using realistic rock structures in high-pressure silicon micromodels. *International Journal of Greenhouse Gas Control*, *53*, 178–186. https://doi.org/10.1016/j.ijggc.2016.06.017

Katsuki, D., Ohmura, R., Ebinuma, T., & Narita, H. (2007). Methane hydrate crystal growth in a porous medium filled with methane-saturated liquid water. *Philosophical Magazine*, *87*(7), 1057–1069. https://doi.org/10.1080/14786430601021652

Kvamme, B., Graue, A., Buanes, T., Kuznetsova, T., & Ersland, G. (2007). Storage of CO_2 in natural gas hydrate reservoirs and the effect of hydrate as an extra sealing in cold aquifers. *International Journal of Greenhouse Gas Control, 1*(2), 236–246. https://doi.org/10.1016/S1750-5836(06)00002-8

Kvenvolden, K. A. (1988). Origins of methane in the Earth methane hydrate—A major reservoir of carbon in the shallow geosphere? *Chemical Geology*, *71*(1-3), 41–51. https://doi.org/10.1016/0009-2541(88)90104-0

Makogon, Y. F., & Ghassemi, A. (2010). *Effects of self-preservation of natural gas-hydrates*. Paper presented at the 44th U.S. Rock Mechanics Symposium and 5th U.S.-Canada Rock Mechanics Symposium, Salt Lake City, UT. ARMA-10-291.

Milkov, A. V. (2004). Global estimates of hydrate-bound gas in marine sediments: How much is really out there? *Earth-Science Reviews*, *66*(3–4), 183–197. https://doi.org/10.1016/j.earscirev.2003.11.002

Mochizuki, T., & Mori, Y. H. (2006). Clathrate-hydrate film growth along water/hydrate-former phase boundaries—Numerical heat-transfer study. *Journal of Crystal Growth*, *290*(2), 642–652. https://doi.org/10.1016/j.jcrysgro.2006.01.036

Moridis, G. J., Collett, T. S., Pooladi-Darvish, M., Hancock, S. H., Santamarina, C., Boswell, R., et al. (2011). Challenges, uncertainties, and issues facing gas production from gas-hydrate deposits. *SPE Reservoir Evaluation & Engineering*, *14*(01), 76–112. https://doi.org/10.2118/131792-PA

Moridis, G. J., Kowalsky, M. B., & Pruess, K. (2007). Depressurization-induced gas production from Class-1 hydrate deposits. *SPE Reservoir Evaluation & Engineering*, *10*(05), 458–481. https://doi.org/10.2118/97266-PA

Peng, B. Z., Dandekar, A., Sun, C. Y., Luo, H., Ma, Q. L., Pang, W. X., & Chen, G. J. (2007). Hydrate film growth on the surface of a gas bubble suspended in water. *The Journal of Physical Chemistry B*, *111*(43), 12,485–12,493. https://doi.org/10.1021/jp074606m

Ruppel, C., Dickens, G. R., Castellini, D. G., Gilhooly, W., & Lizarralde, D. (2005). Heat and salt inhibition of gas hydrate formation in the northern Gulf of Mexico. *Geophysical Research Letters*, *32*, L04605. https://doi.org/10.1029/2004GL021909

Schoderbek, D., Martin, K. L., Howard, J., Silpngarmlert, S., & Hester, K. (2012). *North slope hydrate fieldtrial: CO_2/CH_4 exchange*. Paper presented at the OTC Arctic Technology Conference, Houston, USA. OTC-23725-MS. https://doi.org/10.4043/23725-MS

Song, W., de Haas, T. W., Fadaei, H., & Sinton, D. (2014). Chip-off-the-old-rock: The study of reservoir-relevant geological processes with real-rock micromodels. *Lab on a Chip*, *14*(22), 4382–4390. https://doi.org/10.1039/C4LC00608A

Tishchenko, P., Hensen, C., Wallmann, K., & Wong, C. S. (2005). Calculation of the stability and solubility of methane hydrate in seawater. *Chemical Geology*, *219*(1-4), 37–52. https://doi.org/10.1016/j.chemgeo.2005.02.008

Tohidi, B., Anderson, R., Clennell, M. B., Burgass, R. W., & Biderkab, A. B. (2001). Visual observation of gas-hydrate formation and dissociation in synthetic porous media by means of glass micromodels. *Geology*, *29*(9), 867–870. https://doi.org/10.1130/0091-7613(2001)

U.S. Energy Information Administration (2017). How much carbon dioxide is produced when different fuels are burned? Retrieved from https://www.eia.gov/tools/faqs/faq.php? id=73&t=11, Accessed November 11, 2017.

Wright, J. F., & Dallimore, S. R. (2004). Pressure-temperature-salinity influences on gas hydrate stability in sediments of the Mallik Gas Hydrate Reservoir, Mackenzie Delta, Canada. Paper presented at the AAPG HEDBERG CONFERENCE "Gas Hydrates: Energy Resource Potential and Associated Geologic Hazards", Vancouver, BC, Canada.

Yamamoto, K., Terao, Y., Fujii, T., Ikawa, T., Seki, M., Matsuzawa, M., & Kanno, T. (2014). *Operational overview of the first offshore production test of methane hydrates in the Eastern Nankai Trough*. Paper presented at the Offshore Technology Conference, Houston, TX. OTC-25243-MS. https://doi.org/10.4043/25243-MS

III

IV

Journal of Petroleum Science and Engineering 177 (2019) 880–888

Contents lists available at ScienceDirect

Journal of Petroleum Science and Engineering

journal homepage: www.elsevier.com/locate/petrol

Measurements of CH_4 and CO_2 relative permeability in hydrate-bearing sandstone

Stian Almenningen[a,*], Jarand Gauteplass[b], Lars Petter Hauge[a], Tanja Barth[b], Martin Anders Fernø[a], Geir Ersland[a]

[a] Department of Physics and Technology, University of Bergen, Norway
[b] Department of Chemistry, University of Bergen, Norway

ARTICLE INFO

Keywords:
CH_4 and CO_2 hydrates
Relative permeability
Effect of hydrate saturation

ABSTRACT

This paper reports measurements of relative permeability to methane (CH_4) and carbon dioxide (CO_2) in hydrate-bearing sandstone core samples. The CH_4 (or CO_2) permeability was measured at reservoir conditions for different hydrate and brine saturations. The saturation span ranged from 0.18 to 0.60 (frac.) for CH_4 gas and from 0.37 to 0.70 (frac.) for liquid CO_2. The hydrate saturation ranged from 0.18 to 0.61 (frac.). The growth of hydrates within sandstone pores reduced the permeability for both the CH_4 and CO_2 system significantly, and the relative reduction was more pronounced for lower gas saturations. This effect is currently not included in numerical models of relative permeability in hydrate-bearing sediments and should be considered. The reported measurements are relevant to production-forecasting of methane gas from hydrate reservoirs and CO_2 storage schemes where CO_2 hydrates may provide self-sealing in cold aquifers.

1. Introduction

Natural gas hydrates can be a nuisance and hazard in gas production and pipeline transport but are also recognized as a promising energy resource for the future. The crystalline compound, formed by hydrogen-bonded water molecules and stabilized by methane (CH_4) molecules, is distributed worldwide in shallow marine sediments and onshore in and below permafrost. Global estimates range from 10^{14} – 10^{18} Sm^3 of entrapped CH_4 gas in natural gas hydrates (Milkov, 2004). Several short-term field pilots (Dallimore et al., 2012; Schoderbek et al., 2012; Yamamoto et al., 2014) have been undertaken but the longer term dynamics of CH_4 production from natural gas hydrate reservoirs remain unclear. Relative permeability functions in hydrate-bearing sediments are key input to model flow and assess the production performance in any production scheme (Moridis et al., 2007; Reagan et al., 2008). Understanding hydrate dissociation pattern and, in turn, the mobilization of gas and water in sedimentary systems is vital to predict long-term production rates (Jang and Santamarina, 2014).

Gas hydrates form with several other small non-polar guest molecules than CH_4 and carbon dioxide (CO_2) is particularly interesting. CO_2 hydrates are thermodynamically more stable than CH_4 hydrates which will induce a spontaneous exchange of the hydrate guest and release CH_4 gas to be produced (Graue et al., 2008). CO_2 hydrates may also aid as an extra sealing for CO_2 storage in cold aquifers (Kvamme et al., 2007). Fluxes of buoyant CO_2 will be significantly reduced by the formation of CO_2 hydrates in the pore space (Tohidi et al., 2010). In order to model the strength and effectiveness of the formed CO_2 hydrate seal, the relationship between CO_2 permeability and CO_2 hydrate saturation must be known. In this case, a critical CO_2 hydrate saturation will immobilize the injected CO_2, whereas from a production point of view a critical CH_4 hydrate saturation will determine when CH_4 gas starts flowing. In either way, it is important to identify the transition in hydrate saturation where the fluids become stationary (Seol and Kneafsey, 2011).

Measuring the permeability of hydrate-saturated porous media is not straightforward as opposed to conventional two-phase flow. The action of performing a permeability measurement will affect the stability of the hydrate system and thereby the permeability itself. When the pore space is partly occupied by gas hydrates, injection of gas or water are typically modelled as regular two-phase flow, where the effective porosity and absolute permeability are functions of the hydrate saturation (Moridis and Pruess, 2014). However, the solid hydrate phase is susceptible for changes during the flow measurement, e.g. hydrate may form, redistribute or dissociate as water and gas are mixed during two-phase flow (Johnson et al., 2011). In the case where the pore space is filled with hydrates and water (containing dissolved

* Corresponding author.
E-mail address: stian.almenningen@uib.no (S. Almenningen).

https://doi.org/10.1016/j.petrol.2019.02.091
Received 3 December 2018; Received in revised form 25 February 2019; Accepted 28 February 2019
Available online 05 March 2019
0920-4105/

hydrate former), injection of undersaturated water leads to scavenging of the dissolved guest molecule from the system (Delli and Grozic, 2014) and subsequent hydrate dissociation. Thermal non-equilibrium effects may also be significant if the injected fluid is not properly cooled before injection, depending on the applied flow rate and temperature control. The pore-scale distribution of hydrates affects the permeability severely independent of the hydrate saturation (Kleinberg et al., 2003). The permeability also depends on the macroscopic distribution of hydrates, as hydrates formed in large patchy clusters exhibit higher permeability compared to distributed hydrates (Mahabadi et al., 2019). The pore-scale hydrate distribution is often simply considered as either grain-coating or pore-filling depending on the initial fluid distribution and choice of hydrate formation method (Kleinberg et al., 2003). One study suggests that the hydrate distribution changes from mineral coating to pore center filling when the hydrate saturation is increased above 35% (Kumar et al., 2010). The effect of hydrate saturation on the relative permeability to gas is also shown to differ when different porous media is used (Jaiswal et al., 2009), and anisotropic permeability values were found when the effect of applied stress to the core sample was investigated, showing the importance of differentiating between horizontal and vertical permeability in the field (Dai et al., 2018). The abovementioned issues related to obtaining the permeability of hydrate-bearing sediments give rise to a scattered range of results in the literature. The end-point relative permeability to gas has been measured to be less than 0.01 ($S_H \approx 0.13$, $S_g \approx 0.26$ and $S_w \approx 0.61$) in one study (Johnson et al., 2011) and approximately 0.1 ($S_H \approx 0.15$, $S_g \approx 0.28$, $S_w \approx 0.57$) in another (Ahn et al., 2005). Johnson et al. (2011) used nitrogen gas to obtain gas-water relative permeability curves because of severe secondary hydrate formation when CH_4 was injected, contrary to Ahn et al. (2005) and Jaiswal et al. (2009) which did not experience plugging during unsteady state permeability measurements with CH_4 gas. The disadvantage with using nitrogen gas is that the displacement of CH_4 gas will likely destabilize the CH_4 hydrate.

The scope of this work is to compare the relative permeability to CH_4 gas in CH_4 hydrate saturated sandstone with the relative permeability to liquid CO_2 in CO_2 hydrate saturated sandstone. The solubility of CO_2 in water (Servio and Englezos, 2001) is approximately one order of magnitude higher than the solubility of CH_4 in water (Servio and Englezos, 2002), which may yield different hydrate growth patterns and possibly different relative permeability functions. The limiting CH_4 (or CO_2) saturation where the apparent permeability of the hydrate-filled pore space drops to zero is identified for both hydrate formers. The permeability values obtained in this study can be used as input to numerical simulators, especially in schemes trying to model the production of hydrate-bound CH_4 gas by CO_2 injection. The long-term prediction of CH_4 gas production from hydrate must incorporate the change in fluid permeability as the hydrate saturation decreases through dissociation.

2. Materials and methods

2.1. Establishing initial brine saturation

Cylindrical Bentheim sandstone core plugs with nominal porosity of 0.24 (frac.) and absolute permeability of 1.1–1.9 Darcy (detailed in Table 1) were used as analogues to reservoir rock. The core plugs were partially saturated with brine by one of three methods to create a range in initial water saturation and distribution in the core: A) a fully brine saturated core plug (initially air evacuated and filled with brine under vacuum) was partially saturated with gaseous CO_2 at ambient conditions by injecting at a constant pressure drop of ~0.3 MPa; B) a dry core plug was submerged in brine for a limited time (10–20 s) to allow brine to invade the pore space by spontaneous imbibition; or C) a fully brine saturated core plug was wrapped in wiping paper and subjected to a vacuum (P ~ 100 Pa) for 10–20 s to remove brine from the pore space. Average brine saturations were quantified by weight calculations and spatial distributions of brine were quantified and visualized using magnetic resonance imaging (MRI). The distribution of initial brine in the core was later used to aid the interpretation of the permeability measurements.

Table 1
Core plug properties and initial saturation of brine. Every core plug was ~15 cm long with a diameter of ~5 cm. Margin of errors reflect instrumental uncertainties. *The absolute permeability was not measured in this core plug and the given value is the midpoint of the other permeability values.

Core ID	Φ (frac.) ± 0.01	K_{abs} (D)	Saturation method	S_{wi} (frac.) ± 0.01	Brine salinity (wt% NaCl) ± 0.01
CO2_base	0.23	1.11 ± 0.07	–	1	3.50
CO2_1	0.24	*1.5 ± 0.1	A	0.27	0.10
CO2_2	0.24	1.45 ± 0.03	B	0.34	0.10
CO2_3	0.24	*1.5 ± 0.1	B	0.40	0.10
CO2_4	0.24	1.53 ± 0.04	B	0.40	0.10
CO2_5	0.24	*1.5 ± 0.1	B	0.43	0.10
CO2_6	0.24	*1.5 ± 0.1	B	0.44	0.10
CO2_7	0.24	*1.5 ± 0.1	A	0.45	0.10
CO2_8	0.24	1.53 ± 0.04	A	0.51	0.10
CO2_9	0.24	*1.5 ± 0.1	A	0.58	0.10
CH4_1	0.24	1.7 ± 0.2	C	0.46	3.50
CH4_2	0.24	1.9 ± 0.6	C	0.53	3.50
CH4_3	0.24	*1.5 ± 0.5	C	0.54	3.50
CH4_4	0.24	*1.5 ± 0.5	C	0.54	3.50
CH4_5	0.24	*1.5 ± 0.5	C	0.54	3.50
CH4_6	0.24	1.9 ± 0.6	C	0.64	3.50
CH4_7	0.24	1.3 ± 0.1	C	0.64	3.50
CH4_8	0.24	1.8 ± 0.2	C	0.73	3.50

2.2. Hydrate formation and permeability measurement

Brine-saturated cores were mounted into a rubber sleeve and placed inside a Hassler core holder (Fig. 1). All pump lines leading to the core (not the core itself) were purged under vacuum before filling the pumps with either CH_4 (> 99.5%) or CO_2 (> 99.999%) gas. The gas was introduced to the pore space at atmospheric pressure, and the pore pressure was then gradually increased by injecting gas from both ends: 8.3 MPa with CH_4 and 7.0 MPa with CO_2. The CH_4 remained gaseous throughout the experiments whereas the CO_2 was converted to liquid state during the pressure increase. The overburden pressure was continuously kept 3 MPa above the pore pressure. End-point relative permeability to CH_4 gas prior to hydrate formation was measured at steady-state (gas injection rate equal to gas production rate) with a maximum volumetric flow rate of 16 mL/min to avoid further de-saturation of the core. Injection pressure at the inlet, differential pressure across the core length, and core surface temperature at the inlet were recorded for three different flow rates to verify linearity between pressure drop and flow rate. The effective permeability to CH_4 was subsequently calculated by Darcy's law. The effective permeability to liquid CO_2 was not measured in each core prior to hydrate formation. Instead, CO_2-brine relative permeability curves were generated by draining a reference core initially saturated with brine. The core was gradually de-saturated with brine by incrementally increasing the volumetric flow rate of CO_2 and the effective permeability to liquid CO_2 was calculated by Darcy's law for each saturation step.

Hydrate formation was initiated by cooling the system to 4 °C by circulating antifreeze through a cooling jacket surrounding the core holder (Fig. 1). The volume of injected CH_4 or CO_2 needed to maintain constant pore pressure during hydrate formation was recorded and used to calculate the saturation of hydrate, see Almenningen et al. (2017) for details. A hydration number of 5.99 was used for CH_4 (Circone et al., 2005) and 6.4 for CO_2 (Henning et al., 2000). Less than a day of formation was typically required to complete CO_2 hydrate formation whereas CH_4 hydrate formation continued for up to ten days. The end-

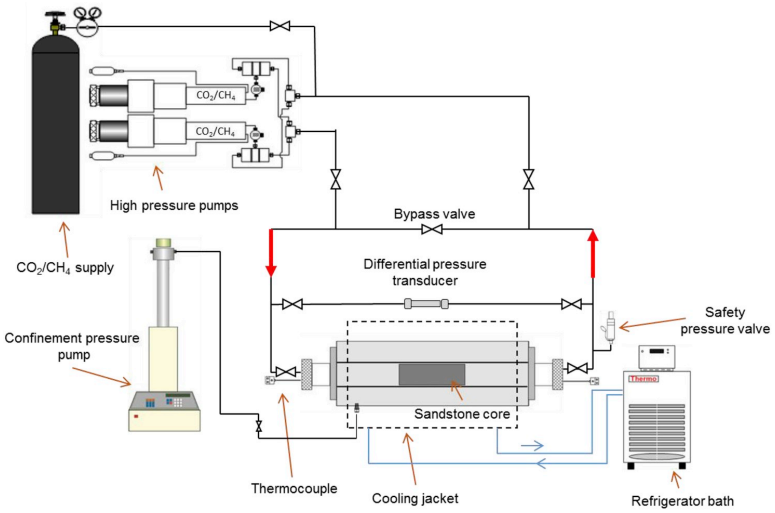

Fig. 1. Schematic of experimental design, modified from Hågenvik (2013). The core was mounted in a Hassler core holder and a net confinement pressure of 3 MPa was applied. The system temperature was maintained at 4 °C by circulating antifreeze through a cooling jacket surrounding the core holder. CH_4 or CO_2 were injected through the core from left to right, and the differential pressure was recorded and used to calculate the permeability.

point relative permeability (CH_4 or CO_2) was then measured by constant volumetric flow rate injection and a fixed outlet production pressure. Two separate high-pressure pumps were used for injection and production. The differential pressure used to calculate relative permeability was recorded at steady-state (gas injection rate equal to gas production rate), assuming constant fluid (hydrate, gas and water) saturations in the core. The differential pressure was monitored for several minutes after steady-state was achieved to verify the constant saturation assumption. No water production was observed during measurements. The injected CH_4 (or CO_2) was not precooled, but low volumetric injection rates allowed heat exchange between the CH_4 (or CO_2) and the cooled injection line leading into the core, and the inlet core temperature did not increase during the injection. Constant temperature at the inlet and outlet of the core also suggested no reformation or dissociation of hydrates during the flow period. However, localized hydrate phase transitions could not be ruled out without *in situ* monitoring of the pore space.

2.3. Calculation of fluid saturation

The fluid saturation (and water saturation) can be calculated either as a fraction of the original pore volume or as a fraction of the dynamic pore volume adjusted for hydrate growth. Both saturation definitions are used throughout the manuscript and are calculated as follow:

Constant pore volume

The fluid saturation is given as:

$$S_{CH4(or\ CO2)} = \frac{V_{CH4(or\ CO2)}}{V_{pore}} \quad (1)$$

where $V_{CH4\ (or\ CO2)}$ is the volume of gaseous CH_4 (or volume of liquid CO_2) and V_{pore} is the pore volume of the rock. The formation of hydrate is treated as an additional phase and the pore volume is saturated with the sum of three co-existing phases (CH_4 (or CO_2), water and hydrate):

$$V_{pore} = V_{CH4(or\ CO2)} + V_w + V_H \quad (2)$$

Dynamic pore volume

The solid hydrate is treated as an extension of the rock matrix and not as a separate phase in the pore space. The pore volume is then denoted as an effective pore volume and is given by the sum of two phases (CH_4 (or CO_2) and water):

$$V^*_{pore} = V_{pore} - V_H = V_{CH4(or\ CO2)} + V_w \quad (3)$$

The effective fluid saturation becomes

$$S^*_{CH4(or\ CO2)} = \frac{V_{CH4(or\ CO2)}}{V^*_{pore}} \quad (4)$$

3. Results and discussion

3.1. Initial brine distribution

The brine saturation and distribution in the core prior to hydrate formation were highly sensitive to the saturation method used (A, B or C), and the brine saturation varied along the length of the core as well as in the transverse direction (Figs. 2 and 3).

Saturation method A (De-saturation of a fully brine-saturated core by CO_2 injection at ambient conditions): This method resulted in a uniformly distributed brine saturation in every cross-section of the core (Fig. 2A). However, the brine saturation changed with the length of the core and was lowest at the inlet side where the CO_2 had been injected (Fig. 3). The brine saturation was increased at the outlet face of the core because of the capillary end-effect.

Saturation method B (Temporary spontaneous imbibition for 10–20 s): In this case, the longitudinal saturation values were consistent (Fig. 3), but the brine saturation varied in the transverse direction and was highest further away from the core center (Fig. 2B). The spontaneous imbibition took place radially inwards to the core center and the time-limited water supply resulted in a saturation gradient.

Saturation method C (Fully brine-filled core wrapped in paper and purged under vacuum for 10–20 s): This method yielded the most non-uniform saturation of brine. The brine saturation was highest in the center of the core and decreased radially outwards (Fig. 2C), opposite of the saturation gradient in method B. The saturation was also changing along the length of the core and the brine saturation was lowest in both ends of the core (Fig. 3).

The different outcome of brine saturation and distribution from the three methodologies highlights the difficulty associated with establishing a repeatable homogeneous initial saturation. The initial brine distribution is not of interest in itself, but a homogenous brine saturation will increase the likelihood of achieving a homogenous final hydrate saturation. This is desired to ensure consistency between runs and to correlate fluid permeability to hydrate and fluid saturation. The

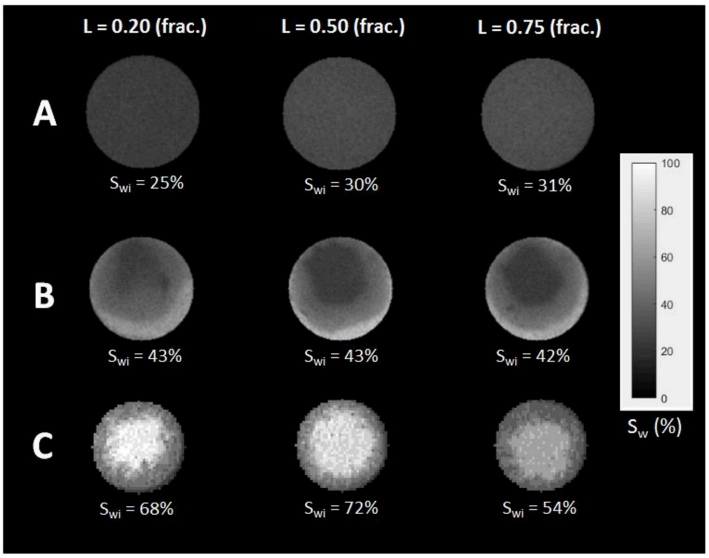

Fig. 2. Initial distribution of brine prior to pressurization by CH_4 (or CO_2) and subsequent hydrate formation. A: Core partially saturated with brine by CO_2 injection at ambient conditions into a 100% brine-filled core. B: Core partially saturated with brine by temporary (10–20 s) spontaneous imbibition. C: Core partially saturated with brine by vacuum-drainage of a 100% brine-filled core.

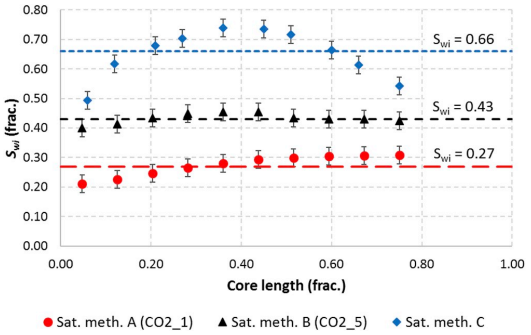

Fig. 3. Initial distribution of brine along the length of the core prior to pressurization by CH_4 (or CO_2) and subsequent hydrate formation. The average brine saturation is indicated with straight lines. Note that the core saturated by saturation method C (diamonds) are not part of the permeability experiments in this study (not included in Table 1).

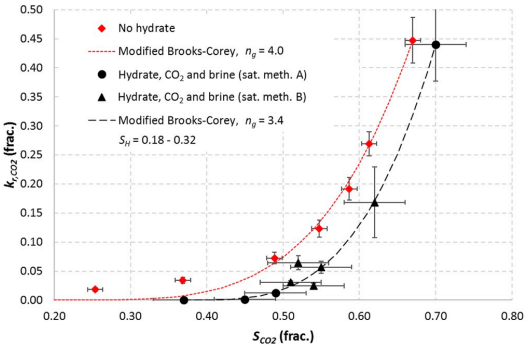

Fig. 4. Relative permeability values for liquid CO_2 as a function of CO_2 saturation. Two-phase permeability (diamonds) was obtained by draining brine at different flow rates in a single core. Three-phase permeability values represent individual cores where the hydrate saturation ranged from 0.18 to 0.32: Saturation method A in circles and saturation method B in triangles. The permeability values are fitted with modified Brooks-Corey curves based on least squares regression. Error bars reflect instrumental uncertainties.

extent of hydrate saturation heterogeneity within each core is not quantified in this experimental work, but discrepancies in measured permeability between experiments with the same fluid saturation may be attributed to changes in saturation distribution between runs.

3.2. Carbon dioxide relative permeability

CO_2 relative permeability values in Bentheim sandstone (Fig. 4) were measured with and without CO_2 hydrate present in the pore space. The former case is henceforth referred to as a three-phase system (CO_2 hydrate, liquid CO_2 and brine) whereas the latter case is referred to as a two-phase system (liquid CO_2 and brine). End-point $k_{r,CO2}$ measurements without CO_2 hydrate present used a single core plug (CO2_base) with different CO_2 flow rates to achieve a range in saturations (S_{CO2} = 0.25–0.67). End-point $k_{r,CO2}$ with CO_2 hydrate present were measured using different core plugs (see Table 2) with a range in CO_2 saturations (S_{CO2} = 0.37–0.70) and CO_2 hydrate saturations (S_H = 0.18–0.32). The relative permeability to CO_2 was consistently lower for the three-phase system than for the two-phase system for similar saturations of CO_2. The presence of solid hydrates clearly reduce the CO_2 permeability even if the CO_2 saturation is kept constant. The effect of the initial brine saturation method was limited as all of the three-phase permeability values follow the saturation consistently (Fig. 4), meaning that saturation method A and B can both be used as a starting point for hydrate formation experiments. The radial brine saturation gradient resulting from saturation method B did not influence the final hydrate distribution and thereby the permeability significantly compared to the hydrate distribution and permeability resulting from saturation method A.

The permeability curves were fitted with modified Brooks-Corey curves (Alpak et al., 1999):

$$k_{r,CO2} = k^0_{r,CO2}\left(\frac{S_{CO2} - S_{CO2r}}{1 - S_{CO2r} - S_{wr}}\right)^{n_g} \quad (5)$$

Table 2
List of every CO_2 permeability experiment. The core pressure and temperature were kept constant at 7.0 MPa and 4 °C, respectively, during hydrate formation and permeability measurements. Margin of errors reflect instrumental uncertainties.

Core ID	S_H (frac.) ± 0.04	S_{CO2} (frac.)	$k_{r,CO2}$ (frac.)
CO2_base	0	0.25 ± 0.01	0.018 ± 0.003
CO2_base	0	0.37 ± 0.01	0.034 ± 0.005
CO2_base	0	0.49 ± 0.01	0.07 ± 0.01
CO2_base	0	0.55 ± 0.01	0.12 ± 0.01
CO2_base	0	0.59 ± 0.01	0.19 ± 0.02
CO2_base	0	0.61 ± 0.01	0.27 ± 0.02
CO2_base	0	0.67 ± 0.01	0.45 ± 0.04
CO2_1	0.18	0.70 ± 0.04	0.44 ± 0.06
CO2_2	0.23	0.62 ± 0.04	0.17 ± 0.06
CO2_3	0.31	0.54 ± 0.04	0.025 ± 0.004
CO2_4	0.32	0.55 ± 0.04	0.06 ± 0.01
CO2_5	0.30	0.51 ± 0.04	0.031 ± 0.003
CO2_6	0.19	0.52 ± 0.04	0.06 ± 0.01
CO2_7	0.30	0.49 ± 0.04	0.012 ± 0.001
CO2_8	0.24	0.45 ± 0.04	0.00111 ± 0.00003
CO2_9	0.30	0.37 ± 0.04	0

where $k^0_{r,CO2}$ is end-point relative permeability to CO_2 at residual brine saturation S_{wr}, S_{CO2r} is residual saturation of CO_2, and n_g is a fitting parameter controlling the slope of the curve. A residual CO_2 saturation of 0.20 was assumed for the two-phase case and 0.37 when hydrate was present, based on the measured residual CO_2 saturations in this study. The best fit was achieved with $n_g = 4.0$ for the two-phase permeability values and $n_g = 3.4$ for the three-phase permeability values (Fig. 4). The corresponding normalized mean square error (NMSE) (Poli and Cirillo, 1993) was 0.23 and 0.02, respectively. Another form of the Brooks-Corey model that has previously been fitted to experimental CO_2-brine permeability data with $N_{CO2} = 2$–5 (Krevor et al., 2012), could not be fitted to the relative permeability values in this study. Notice that the hydrate phase was treated as an extension of the brine phase for the three-phase calculations, meaning that the sum of the brine and hydrate saturations were treated as one phase. Alternatively, the hydrate saturation is considered as a part of the solid matrix, giving scaled CO_2 and brine saturations according to the reduction of the pore volume. The absolute permeability of the porous medium is then a function of the dynamic porosity (Moridis and Pruess (2014) and references therein):

$$K = K_0\left(\frac{\Phi-\Phi_c}{\Phi_0-\Phi_c}\right)^n \quad (6)$$

where K_0 is the absolute permeability when the porosity is Φ_0 (no hydrate), Φ_c is a nonzero critical porosity where the absolute permeability becomes zero, and n is a fitting parameter that is dependent on where hydrate accumulates in the pore space. A value of n equal to 2.3 was chosen to calculate the absolute permeability of each core after hydrate formation, and the critical porosity was assumed to be 0.10 (frac.). The fitting parameter n was chosen as the maximum value that preserved the end-point relative permeability to CO_2 less than one (Fig. 5). A critical porosity of 0.10 corresponded to a critical hydrate saturation of 0.60, which was chosen since the CO_2 permeability became zero at a CO_2 saturation of 0.37. Now, the modified Brooks-Corey model gave the best fit to the measured relative permeability to CO_2 when n_g was set to 5.8 (Fig. 5) with a NMSE value of 0.15.

3.3. Methane relative permeability

The CH_4 permeability was measured as end-point permeability in different cores with different combinations of hydrate and fluid saturation (Table 3). The range in permeability values for the three-phase case was obtained for the CH_4 saturation interval of 0.18–0.44 and the CH_4 hydrate saturation ranged between 0.37 and 0.61. These measurements were first presented in Almenningen et al. (2016). Additional permeability values

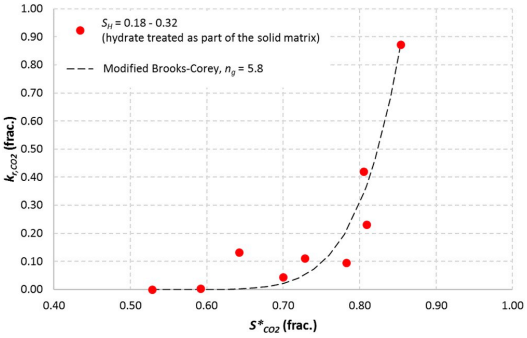

Fig. 5. Relative permeability to liquid CO_2 when hydrate is treated as part of the rock. The saturation of CO_2 (and brine) is scaled according to the reduction in porosity and the absolute permeability is scaled according to Eq. (6) with a fitting parameter $n = 2.3$. The permeability values are fitted with a modified Brooks-Corey curve based on least squares regression.

Table 3
List of all CH_4 permeability experiments. The core pressure and temperature were kept constant at 8.3 MPa and 4 °C, respectively, during hydrate formation and permeability measurements. Margin of errors reflect instrumental uncertainties.

Core ID	No hydrate		Hydrate		
	S_{CH4} (frac.) ± 0.01	$k_{r,CH4}$ (frac.)	S_H (frac.) ± 0.02	S_{CH4} (frac.) ± 0.02	$k_{r,CH4}$ (frac.)
CH4_1	0.54	0.12 ± 0.02	0.46	0.44	1.9E-2 ± 0.3E-2
CH4_2	0.47	0.19 ± 0.08	0.47	0.36	1.2E-3 ± 0.4E-3
CH4_3	0.46	0.09 ± 0.03	0.45	0.36	1.7E-6 ± 0.6E-6
CH4_4	0.46	0.06 ± 0.02	0.47	0.36	4E-6 ± 1E-6
CH4_5	0.46	0.06 ± 0.02	0.51	0.35	1.4E-4 ± 0.5E-4
CH4_6	0.36	0.08 ± 0.03	0.61	0.23	4E-7 ± 1E-7
CH4_7	0.36	0.14 ± 0.02	0.53	0.24	9.9E-7 ± 0.8E-7
CH4_8	0.27	0.032 ± 0.006	0.37	0.18	7.1E-7 ± 0.8E-7

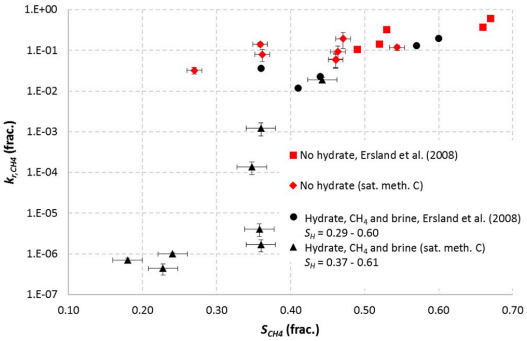

Fig. 6. Relative permeability values for CH_4 gas (logarithmic scale) as a function of CH_4 saturation. Two-phase permeability (diamonds and squares) was obtained on individual cores at room temperature prior to hydrate formation. Three-phase permeability values (triangles and circles) were measured on the same cores at 4 °C after hydrate formation. The hydrate saturation varied from 0.29 to 0.61 in the different cores. This plot was first presented in Almenningen et al. (2016), and some of the data points (squares and circles) are obtained from Ersland et al. (2008) (not included in Table 3). Error bars reflect instrumental uncertainties.

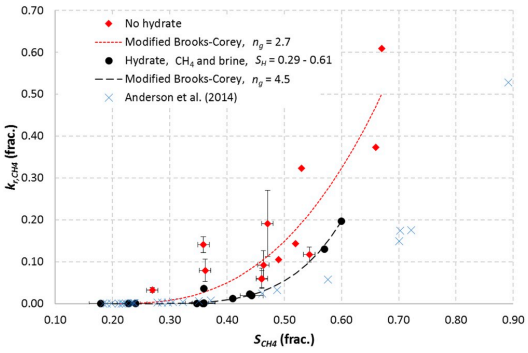

Fig. 7. Relative permeability values for CH_4 gas as a function of CH_4 saturation. Two-phase permeability (diamonds) was obtained on individual cores at room temperature prior to hydrate formation. Three-phase permeability values (circles) were measured on the same cores at 4 °C after hydrate formation. The hydrate saturation varied from 0.29 to 0.61 in the different cores. The permeability values are fitted with modified Brooks-Corey curves based on least squares regression. One data set from Anderson et al. (2014) is included for comparison. Error bars reflect instrumental uncertainties.

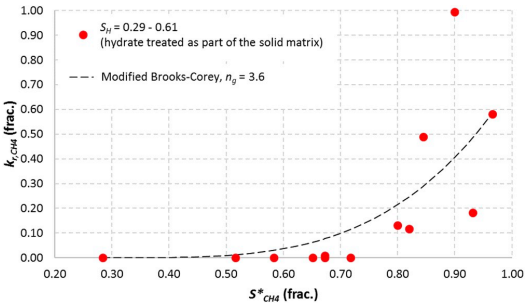

Fig. 8. Relative permeability to CH_4 gas when hydrate is treated as part of the rock. The saturation of CH_4 (and brine) is scaled according to the reduction in porosity and the absolute permeability is scaled according to Eq. (6) with a fitting parameter n = 1.7. The permeability values are fitted with a modified Brooks-Corey curve based on least squares regression.

from Ersland et al. (2008) were included to increase the size of the permeability sample (Fig. 6). A transition of significant loss of CH_4 relative permeability was observed in the CH_4 saturation range equal to 0.33–0.38 when the permeability values were plotted on a logarithmic scale (Fig. 6). In this saturation interval, the effective CH_4 permeability dropped from mD-scale to μD-scale. The three-phase permeability values were also consistently lower than the two-phase permeability values for gas saturations greater than 0.40 (Fig. 7). The addition of solid hydrates lowered the CH_4 permeability at constant CH_4 saturation, similar as for the CO_2 hydrate measurements. The permeability values were scattered, especially for the two-phase flow prior to hydrate formation (Fig. 7). Every core was initially saturated with brine by saturation method C, which was observed to give variations in brine saturation both radially and along the length of the core (Figs. 2 and 3). The scatter in permeability for the two-phase system could therefore be attributed to heterogeneities in the brine distribution. Permeability values obtained during the Iġnik Sikumi field trial (Anderson et al., 2014) are included for comparison in Fig. 7. The reported values from Anderson et al. (2014) are measure of the fluid mobility at given hydrate saturation, and the permeability values are included based on the assumption that the rest of the pore space was filled with CH_4 gas. If immobile water was present in addition to gas, the gas saturation would be less than what is assumed in Fig. 7 and the data points should shift leftwards.

Modified Brooks-Corey curves (Alpak et al., 1999) were compared with the permeability values based on a residual CH_4 saturation of 0.20 for both the two-phase case and when CH_4 hydrate was present. The best fit was achieved with n_g = 2.7 for the two-phase values and n_g = 4.5 for the three-phase values (Fig. 7). The corresponding normalized mean square error (NMSE) was 0.20 and 0.09, respectively. If the CH_4 hydrate saturation was treated as a part of the solid matrix, giving scaled fluid saturation and absolute permeability according to the reduction of available pore space, the permeability values were best matched with n_g = 3.6 (Fig. 8). A fitting parameter n = 1.7 and a critical porosity Φ_0 = 0.07 were used in Eq. (6). The increased scatter of the data points for CH_4 hydrate compared to CO_2 hydrate was reflected by the NMSE value which was equal to 1.09.

3.4. Comparison of results

The relative permeability to CH_4 was higher than the relative permeability to CO_2 in the saturation interval of $0.40 < S_{CH4\ (or\ CO2)} < 0.60$, both for two-phase flow and when hydrate resided in the pores. CO_2 was in liquid state at the operating pressure and temperature of 7.0 MPa and 4 °C, respectively, while CH_4 was a gas at 8.3 MPa and 4 °C. The CO_2 had consequently a much higher density and viscosity (ρ = 932 kg/m^3 and μ = 0.0001 Pa*s) compared to methane (ρ = 70 kg/m^3 and μ = 0.00001 Pa*s). The relative permeability to CO_2 became apparently zero at a CO_2 saturation of 0.37 (S_H = 0.30) as it was not possible to obtain any flow at this saturation. The relative permeability to CH_4 dropped significantly in the CH_4 saturation interval of 0.33–0.38, but not to the extent that the core became completely blocked. Low flow rates were measured down to a CH_4 saturation of 0.18 (S_H = 0.37). The different behavior between CH_4 and CO_2 may arise from the difference in physical state of the phases, and the low detectable flow rates of CH_4 at low CH_4 saturation could result from diffusive flow through the pore space.

The inclusion of solid hydrate in the pore space reduced the relative permeability to CH_4 and CO_2 compared to the two-phase system (no hydrate), at constant CH_4 (or CO_2) saturation. The combination of hydrate and brine in the pore space constituted more resistance to flow than brine alone. This may come of brine and hydrate occupying different parts of the pores. The residual water in the two-phase system will reside close to grain surfaces because of the water-wet grains in Bentheim sandstone, enabling CH_4 (or CO_2) to flow through the middle of the pores. Hydrate is previously shown to grow along the CH_4-water interface, encapsulating the gaseous CH_4 residing in the middle of pores (Almenningen et al., 2018). Many of the CH_4 flow paths are therefore blocked after hydrate has formed. The existence of completely immobile CH_4 (or CO_2) shielded by hydrates are likely the reason why the relative permeability is lower for the three-phase system compared to the two-phase system. A greater degree of the CH_4 (or CO_2) saturation is mobile when only CH_4 (or CO_2) and water are present in the pores. The same reduction in permeability is necessarily not true for other rock types with different wetting properties. If the rock was gas-wet, with water residing in the middle of pores, the hydrate layer formed at the interface would likely affect the gas permeability less than what is observed here. Caution should be exercised when comparing permeability values across rock samples with different mineralogy and unknown hydrate distribution.

The modified Brooks-Corey fitting exponent increased from 4.0 to 5.8 for CO_2 and from 2.7 to 3.6 for CH_4. Simulation results for CH_4 hydrate showed similarly that the fitting exponent increased from 2.6 for S_H = 0.2 to 3.5 for S_H = 0.6 (Mahabadi et al., 2016), and the fitting exponent in a modified Stone equation increased from 1.8 for S_H = 0.1 to 3.5 for S_H = 0.6 (Mahabadi and Jang, 2014). The reduction in relative permeability was quantified further by taking the ratio of the relative permeability to CH_4 (or CO_2) for the three-phase system and the relative permeability to CH_4 (or CO_2) for the two-phase system.

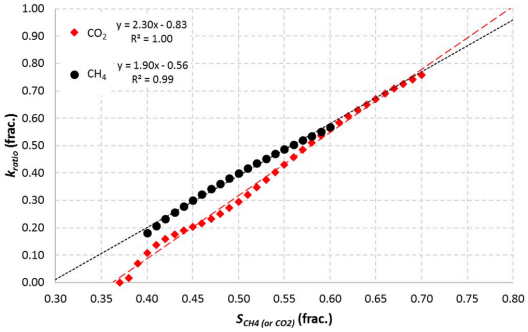

Fig. 9. Permeability ratios for CH_4 gas (circles) and liquid CO_2 (diamonds) as a function of CH_4 (or CO_2) saturation. The permeability ratio is here defined as the relative permeability to CH_4 (or CO_2) when hydrate is present (three-phase) divided by the relative permeability to CH_4 (or CO_2) without hydrate present (two-phase), for equal CH_4 (or CO_2) saturation for each ratio. The hydrate saturation ranged between 0.18 and 0.32 for the CO_2 measurements and 0.29 and 0.56 for the CH_4 measurements.

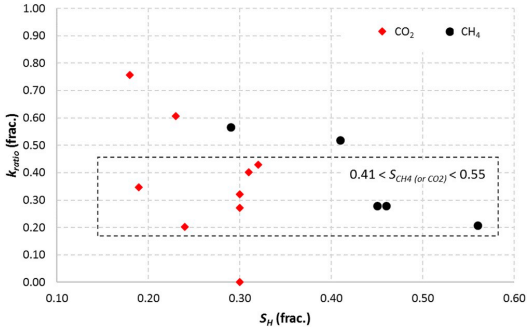

Fig. 10. Permeability ratios for CH_4 gas (circles) and liquid CO_2 (diamonds) as a function of hydrate saturation. The permeability ratio is here defined as the relative permeability to CH_4 (or CO_2) when hydrate is present (three-phase) divided by the relative permeability to CH_4 (or CO_2) without hydrate present (two-phase), for equal CH_4 (or CO_2) saturation for each ratio. The stapled rectangle highlights the limited effect of changing the hydrate saturation on the permeability ratio.

Each permeability ratio was calculated for the same CH_4 (or CO_2) saturation (Fig. 9):

$$k_{ratio}(S_{CH4(or\ CO2)}) = \frac{k_{r,CH4(or\ CO2)}(three-phase)}{k_{r,CH4(or\ CO2)}(two-phase)} \quad (7)$$

The relative permeability to CH_4 (or CO_2) was obtained for the entire saturation interval by interpolation between the measured relative permeability values. The resulting relation between the permeability ratio and CH_4 (or CO_2) saturation showed an increasing trend with saturation for both CH_4 and CO_2 (Fig. 9). The value of the ratio increased linearly with increasing CH_4 (or CO_2) saturation, demonstrating less difference between the two-phase system and the three-phase system for higher CH_4 (or CO_2) saturations. For instance, when the CO_2 saturation was higher than 0.62, the relative permeability of the three-phase system was within 60% of the relative permeability of the two-phase system. This means that the formed hydrate has impaired the CO_2 permeability with 40%, probably by a combination of complete immobilization of some of the CO_2 and by an increase in the tortuosity of the CO_2 flow path. When the CO_2 saturation was lower than 0.45, the relative permeability of the three phase system was at most 20% of the relative permeability of the two-phase system. The effective permeability of the CO_2 was more sensitive to hydrate formation at low CO_2 saturations, most likely because the limited CO_2 phase was more prone to become disconnected and capillary immobilized. The ratio between the two-phase and three-phase relative permeability to CH_4 was comparable to the CO_2 ratio and followed the same increasing trend with increasing CH_4 saturation.

The strong correlation between the ratio of relative permeability and CH_4 (or CO_2) saturation implicates that the actual hydrate saturation had limited effect on the permeability for a given CH_4 (or CO_2) saturation. This is highlighted when the permeability ratio was plotted against hydrate saturation (Fig. 10). The ratio of relative permeability did not change significantly when moving from a hydrate saturation of 0.19–0.56 as long as the CH_4 (or CO_2) saturation was fairly similar ($0.41 < S_{CH4\ (or\ CO2)} < 0.55$). For a given CH_4 (or CO_2) saturation, the presence of hydrate in addition to brine clearly reduced the effective permeability, but the mutual volumetric proportion between hydrate and brine was insignificant for the effective permeability for hydrate saturations lower than 0.56. The same conclusion is reached by investigating the effect of hydrate saturation on the relative permeability to CH_4 in the transitional CH_4 saturation zone between 0.33 and 0.38 (Fig. 11). The relative permeability to CH_4 was lower when hydrate was present in the pore space, but no reduction in permeability was

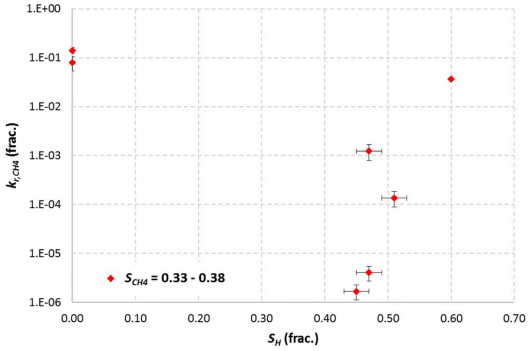

Fig. 11. Relative permeability to CH_4 as a function of hydrate saturation for constant CH_4 gas saturation. Error bars reflect instrumental uncertainties.

observed for increasing hydrate saturation. In fact, it seemed as if the relative permeability to CH_4 was increasing with increasing hydrate saturation for $S_{CH4} = 0.33–0.38$, albeit the spread in hydrate saturation was insufficient to conclude in general. Jaiswal et al. (2009) found two different trends for the change in relative permeability to CH_4 as a function of hydrate saturation when comparing two different core materials. A field sample demonstrated a decreasing relative permeability to CH_4 when the hydrate saturation increased from 0.07 to 0.31 (same trend for three different constant gas saturations of 0.20, 0.40 and 0.60). The same decrease in relative permeability to CH_4 was to the contrary not observed when the hydrate saturation increased from 0.05 to 0.36 in the other sample. The permeability values were more scattered and did not follow any particular trend. This shows that the relation between gas permeability and hydrate saturation remain unclear, and that it does not exist any general correlation between gas permeability and hydrate saturation for constant gas saturations. The effect of hydrate saturation on gas permeability will vary with the particular hydrate growth pattern and resulting hydrate distribution within the pores. The large change in relative permeability to CH_4 observed in the transitional CH_4 saturation (Fig. 11) indicates that it is difficult to reproduce the distribution of residual CH_4 gas after hydrate formation. Especially when the residual CH_4 saturation after hydrate formation is close to the critical CH_4 saturation needed to obtain flow. The effective permeability is then heavily affected by minor perturbations in the CH_4

distribution. The saturation method used to establish the initial brine saturation for the CH_4 experiments was the least successful method in achieving a homogenous brine distribution. Additional investigations into the effect of hydrate saturation on permeability alteration should be aided by *in situ* monitoring of the distribution of phases during flow.

4. Conclusions

This paper presents relative permeability to CH_4 and CO_2 in hydrate-bearing Bentheim sandstone core samples at reservoir conditions. The following conclusions are drawn:

- The relative permeability to CH_4 in a two-phase system without hydrates was higher than the relative permeability to CH_4 in a CH_4/brine/hydrate three-phase system, for similar CH_4 saturation. The modified Brooks-Corey exponent, n_g, increased from 2.7 to 3.6 when hydrate was present in the pore space.
- The relative permeability to CO_2 in a two-phase system without hydrates was higher than the relative permeability to CO_2 in a CO_2/brine/hydrate three-phase system, for similar CO_2 saturations. The modified Brooks-Corey exponent, n_g, increased from 4.0 to 5.8 when hydrate was present in the pore space.
- The observed reduction in permeability is believed to be related to an increase of immobile CH_4 (or CO_2) after hydrates have formed: A greater degree of the CH_4 (or CO_2) saturation is mobile when only CH_4 (or CO_2) and water are present in the pores.
- The relative reduction in permeability because of hydrates increased for decreasing CH_4 (or CO_2) saturation. The effective permeability of the CH_4 (or CO_2) was more sensitive to hydrate formation at low CH_4 (or CO_2) saturations, most likely because the limited CH_4 (or CO_2) phase was more prone to become disconnected and capillary immobilized.
- No correlation between permeability and hydrate saturation was found for constant CH_4 (or CO_2) saturation.

Acknowledgements

The authors would like to acknowledge Equinor for use of the MRI facility at Equinor's laboratories in Bergen. Some of the authors are indebted to the Research Council of Norway under Climit project: 255490.

Nomenclature

K_{abs}	absolute permeability (Darcy)
k_r^0	end-point relative permeability (frac.)
k_{ratio}	the ratio of the relative permeability to CH_4 (or CO_2) for the three-phase system and the relative permeability to CH_4 (or CO_2) for the two-phase system (frac.)
$k_{r,CH4}$	relative permeability to CH_4 (frac.)
$k_{r,CO2}$	relative permeability to CO_2 (frac.)
L	core length (frac.)
n	fitting parameter in permeability reduction formula (−)
n_g	fitting parameter in modified Brooks-Corey model (−)
S_{CH4}	saturation of methane (frac.)
S^*_{CH4}	effective saturation of methane (frac.)
S_{CO2}	saturation of carbon dioxide (frac.)
S^*_{CO2}	effective saturation of carbon dioxide (frac.)
S_g	saturation of gas (frac.)
S_H	saturation of hydrate (frac.)
S_r	residual saturation (frac.)
S_w	saturation of water (frac.)
S_{wi}	initial saturation of water (frac.)
V_{CH4}	volume of methane (mL)
V_{CO2}	volume of carbon dioxide (mL)
V_H	volume of hydrate (mL)
V_{pore}	pore volume (mL)
V^*_{pore}	effective pore volume (mL)
V_w	volume of water (mL)
Φ	porosity (frac.)

Appendix A. Supplementary data

Supplementary data to this article can be found online at https://doi.org/10.1016/j.petrol.2019.02.091.

References

Ahn, T., Lee, J., Huh, D.G., Kang, J.M., 2005. Experimental study on two-phase flow in artificial hydrate-bearing sediments. Geosystem Engineering 8 (4), 101–104. https://doi.org/10.1080/12269328.2005.10541244.

Almenningen, S., Flatlandsmo, J., Fernø, M.A., Ersland, G., 2017. Multiscale laboratory verification of depressurization for production of sedimentary methane hydrates. SPE J. 22 (01), 138–147. https://doi.org/10.2118/180015-PA.

Almenningen, S., Juliussen, H., Ersland, G., 2016. Permeability measurements on hydrate-bearing sandstone cores with excess water. In: Paper Presented at the 30th International Symposium of the Society of Core Analysts, Snowmass, Colorado, USA.

Almenningen, S., Iden, E., Fernø, M.A., Ersland, G., 2018. Salinity effects on pore-scale methane gas hydrate dissociation. J. Geophys. Res. Solid Earth 123 (7), 5599–5608. https://doi.org/10.1029/2017JB015345.

Alpak, F.O., Lake, L.W., Embid, S.M., 1999. Validation of a modified Carman-Kozeny equation to model two-phase relative permeabilities. In: Paper Presented at the SPE Annual Technical Conference and Exhibition, Houston, Texas, USA, . https://doi.org/10.2118/56479-MS.

Anderson, B., Boswell, R., Collett, T.S., Farrell, H., Ohtsuki, S., et al., 2014. Review of the findings of the ignik Sikumi Co2-ch4 gas hydrate exchange field trial. In: Paper Presented at the 8th International Conference on Gas Hydrates, Beijing, China.

Circone, S., Kirby, S.H., Stern, L.A., 2005. Direct measurement of methane hydrate composition along the hydrate equilibrium boundary. J. Phys. Chem. B 109 (19), 9468–9475. https://doi.org/10.1021/jp0504874.

Dai, S., Kim, J., Xu, Y., Waite, W.F., Jang, J., et al., 2018. Permeability anisotropy and relative permeability in sediments from the national gas hydrate program expedition 02, offshore India. Mar. Petrol. Geol (in press). https://doi.org/10.1016/j.marpetgeo.2018.08.016.

Dallimore, S., Yamamoto, K., Wright, J.F., Bellefleur, G., 2012. Scientific results from the JOGMEC/NRCan/Aurora mallik 2007–2008 gas hydrate production Research well program, mackenzie delta, northwest territories, Canada, BulletinNo. 601. Natural Resources Canada.

Delli, M.L., Grozic, J.L.H., 2014. Experimental determination of permeability of porous media in the presence of gas hydrates. J. Pet. Sci. Eng. 120, 1–9. https://doi.org/10.1016/j.petrol.2014.05.011.

Ersland, G., Husebø, J., Graue, A., Kvamme, B., Baldwin, B., et al., 2008. Measurements of gas permeability and non-Darcy flow in gas-water-hydrate systems. In: Paper Presented at the 6th International Conference on Gas Hydrates, Vancouver, Canada.

Graue, A., Kvamme, B., Baldwin, B., Stevens, J., Howard, J.J., et al., 2008. MRI visualization of spontaneous methane production from hydrates in sandstone core plugs when exposed to CO2. SPE J. 13 (2), 146–152. https://doi.org/10.2118/118851-PA.

Henning, R.W., Schultz, A.J., Thieu, V., Halpern, Y., 2000. Neutron diffraction studies of CO2 clathrate Hydrate: formation from deuterated ice. J. Phys. Chem. A 104 (21), 5066–5071. http://doi.org/10.1021/jp0001642.

Hågenvik, C., 2013. CO2 Injection in Hydrate Bearing Sandstone with Excess Water. MSc. University of Bergen, Bergen, Norway.

Jaiswal, N.J., Dandekar, A., Patil, S., Hunter, R.B., Collett, T.S., 2009. Relative permeability measurements of gas-water-hydrate systems. Natural gas hydrates - Energy resource potential and associated geologic hazards: AAPG Memoir 89, 723–733. https://doi.org/10.1306/13201135M893366.

Jang, J., Santamarina, J.C., 2014. Evolution of gas saturation and relative permeability during gas production from hydrate-bearing sediments: gas invasion vs. gas nucleation. J. Geophys. Res. Solid Earth 119 (1), 116–126. https://doi.org/10.1002/2013JB010480.

Johnson, A., Patil, S., Dandekar, A., 2011. Experimental investigation of gas-water relative permeability for gas-hydrate-bearing sediments from the mount elbert gas hydrate stratigraphic test well, Alaska north slope. Mar. Petrol. Geol. 28 (2), 419–426. https://doi.org/10.1016/j.marpetgeo.2009.10.013.

Kleinberg, R.L., Flaum, C., Griffin, D.D., Brewer, P.G., Malby, G.E., et al., 2003. Deep sea NMR: methane hydrate growth habit in porous media and its relationship to hydraulic permeability, deposit accumulation, and submarine slope stability. J. Geophys. Res. Solid Earth 108 (B10), 1–17. https://doi.org/10.1029/2003JB002389.

Krevor, S.C.M., Pini, R., Zuo, L., Benson, S.M., 2012. Relative permeability and trapping of CO2 and water in sandstone rocks at reservoir conditions. Water Resour. Res. 48 (2), 1–16. http://doi.org/10.1029/2011WR010859.

Kumar, A., Maini, B., Bishnoi, P.R., Clarke, M., Zatsepina, O., Srinivasan, S., 2010. Experimental determination of permeability in the presence of hydrates and its effect on the dissociation characteristics of gas hydrates in porous media. J. Pet. Sci. Eng. 70 (1–2), 114–122. https://doi.org/10.1016/j.petrol.2009.10.005.

Kvamme, B., Graue, A., Buanes, T., Kuznetsova, T., Ersland, G., 2007. Storage of CO2 in natural gas hydrate reservoirs and the effect of hydrate as an extra sealing in cold aquifers. Int. J. Greenh. Gas Con. 1 (2), 236–246. https://doi.org/10.1016/S1750-

5836(06)00002-8.
Mahabadi, N., Dai, S., Seol, Y., Jang, J., 2019. Impact of hydrate saturation on water permeability in hydrate-bearing sediments. J. Pet. Sci. Eng. 174, 696–703. https://doi.org/10.1016/j.petrol.2018.11.084.
Mahabadi, N., Dai, S., Seol, Y., Yun, T.S., Jang, J., 2016. The water retention curve and relative permeability for gas production from hydrate-bearing sediments: pore-network model simulation. Geochem. Geophys. Geosyst. 17 (8), 3099–3110. https://doi.org/10.1002/2016GC006372.
Mahabadi, N., Jang, J., 2014. Relative water and gas permeability for gas production from hydrate-bearing sediments. Geochem. Geophys. Geosyst. 15 (6), 2346–2353. http://doi.org/10.1002/2014GC005331.
Milkov, A.V., 2004. Global estimates of hydrate-bound gas in marine sediments: how much is really out there? Earth Sci. Rev. 66 (3–4), 183–197. https://doi.org/10.1016/j.earscirev.2003.11.002.
Moridis, G.J., Pruess, K., 2014. User's Manual of the Tough+ Core Code v1.5: A General-Purpose Simulator of Non-isothermal Flow and Transport through Porous and Fractured Media. Lawrence Berkeley National Laboratory, USA Report LBNL-6871E. Retrieved from.
Moridis, G.J., Kowalsky, M.B., Pruess, K., 2007. Depressurization-Induced gas production from class-1 hydrate deposits. SPE Reservoir Eval. Eng. 10 (5), 458–481. https://doi.org/10.2118/97266-PA.
Poli, A.A., Cirillo, M.C., 1993. On the use of the normalized mean square error in evaluating dispersion model performance. Atmos. Environ. Part A. General Topics 27 (15), 2427–2434. https://doi.org/10.1016/0960-1686(93)90410-Z.
Reagan, M.T., Moridis, G.J., Zhang, K., 2008. Sensitivity analysis of gas production from class 2 and class 3 hydrate deposits. In: Paper Presented at the Offshore Technology Conference, Houston, USA, . https://doi.org/10.4043/19554-MS.
Schoderbek, D., Martin, K.L., Howard, J.J., Silpngarmlert, S., Hester, K., 2012. North slope hydrate fieldtrial: CO2/CH4 exchange. In: Paper Presented at the OTC Arctic Technology Conference, Houston, USA, . https://doi.org/10.4043/23725-MS.
Seol, Y., Kneafsey, T.J., 2011. Methane hydrate induced permeability modification for multiphase flow in unsaturated porous media. J. Geophys. Res. Solid Earth 116 (B8), 1–15. https://doi.org/10.1029/2010JB008040.
Servio, P., Englezos, P., 2001. Effect of temperature and pressure on the solubility of carbon dioxide in water in the presence of gas hydrate. Fluid Phase Equilib. 190 (1), 127–134. https://doi.org/10.1016/S0378-3812(01)00598-2.
Servio, P., Englezos, P., 2002. Measurement of dissolved methane in water in equilibrium with its hydrate. J. Chem. Eng. Data 47 (1), 87–90. https://doi.org/10.1021/je0102255.
Tohidi, B., Yang, J., Salehabadi, M., Anderson, R., Chapoy, A., 2010. CO2 hydrates could provide secondary safety factor in subsurface sequestration of CO2. Environ. Sci. Technol. 44 (4), 1509–1514. https://doi.org/10.1021/es902450j.
Yamamoto, K., Terao, Y., Fujii, T., Ikawa, T., Seki, M., et al., 2014. Operational overview of the first offshore production test of methane hydrates in the Eastern Nankai Trough. In: Paper Presented at the Offshore Technology Conference, Houston, Texas, USA, . https://doi.org/10.4043/25243-MS.

V

International Journal of Greenhouse Gas Control 79 (2018) 272–278

Contents lists available at ScienceDirect

International Journal of Greenhouse Gas Control

journal homepage: www.elsevier.com/locate/ijggc

Visualization of hydrate formation during CO_2 storage in water-saturated sandstone

Stian Almenningen[a,*], Jarand Gauteplass[b], Per Fotland[c], Gry L. Aastveit[c], Tanja Barth[b], Geir Ersland[a]

[a] Department of Physics and Technology, University of Bergen, Norway
[b] Department of Chemistry, University of Bergen, Norway
[c] Equinor ASA, Bergen, Norway

ARTICLE INFO

Keywords:
Subsurface CO_2 sequestration
Gas hydrate
MRI tomography
Direct pore-level visualization

ABSTRACT

Formation of solid CO_2 hydrates during geosequestration of CO_2 may offer increased storage capacity and provide extra sealing in cold aquifers. Evaluation of the integrity and distribution of the formed hydrate seal requires comprehensive knowledge about the CO_2 flow and hydrate growth pattern within sedimentary pores. We address this knowledge gap by pore- to core-scale visualization of hydrate formation during liquid CO_2 injection in water-filled sandstone (P = 70 bar, T = 1–2 °C). Pore-level hydrate growth is analyzed by direct imaging of the pore space in a micromodel chip that is an analog to the pore network in a sandstone. Flow visualization of CO_2-water drainage followed by hydrate formation is also presented at core-scale in Bentheim sandstone using high-field MR imaging. The image results verified hydrate nucleation both at the liquid-liquid interface and in the water phase alone due to the presence of dissolved CO_2. The pore-filling hydrate growth pattern effectively reduced the sandstone permeability and showed the potential of CO_2 hydrate as a sealing mechanism during CO_2 sequestration.

1. Introduction

Combustion of fossil fuels for heating, transportation and electricity generation has contributed to an overall increase in atmospheric CO_2 concentration of 100 ppm (increase of 36%) since the pre-industrial era (IPCC, Climate Change, 2014). There is agreement between climate scientists that the recent increase in global average surface temperature partly is caused by the increased concentration of CO_2 in the atmosphere. An increase in the global average temperature will affect the melting of the polar ice with corresponding sea level rise, and may lead to changes in the weather patterns and more extreme weather (IPCC, Climate Change, 2014). Still, fossil fuels constitute around 86% of the world's primary energy consumption (BP, 2017) and the use of gas, oil and coal continues to grow (IEA, 2017); primarily because of economic growth in emerging countries seeking to increase their inhabitants' standard of living. The global energy needs are expected to increase by 30% from today and until 2040 (IEA, 2017).

The continued use of fossil fuels, until renewable energy alternatives become cost-effective and fully competitive, relies on the implementation of carbon capture and storage (CCS) to mitigate the contribution of anthropogenic CO_2 emissions to the atmosphere. Proposed sites for CO_2 sequestration range from mined salt caverns, depleted hydrocarbon reservoirs, saline aquifers, and in coal beds (Bachu, 2000). The combination of oil displacement and CO_2 storage is known as carbon capture, utilization and storage (CCUS) and provides an economic incentive for energy companies to inject and store CO_2. Sequestration in saline aquifers has a large volumetric potential and various projects are already up and running (Michael et al., 2010). In the Utsira formation offshore Norway the injection amounts to 10^6 tons of liquid CO_2 annually (Baklid et al., 1996). The injected CO_2 is immobilized by various physicochemical processes including structural and stratigraphic trapping, residual CO_2 trapping, solubility trapping and mineral trapping. The storage security of each trapping mechanism is increasing, respectively, but so is also the time needed for the trapping mechanism to become significant (Benson et al., 2005).

Introducing CO_2 to cold pore water (< 10 °C) at elevated pressure (> 25 bar) leads to formation of CO_2 hydrates. Suitable combinations of pressure and temperature are typically found ~250 to ~530 m below sea level (Tohidi et al., 2010). The solid structure of natural gas hydrates provides a high-density alternative for CO_2 storage with fast reaction kinetics similar to mineral trapping (Zatsepina and Pooladi-Darvish, 2011; Zatsepina and Buffett, 2002). Injecting CO_2 directly into

* Corresponding author.
E-mail address: stian.almenningen@uib.no (S. Almenningen).

https://doi.org/10.1016/j.ijggc.2018.11.008
Received 6 July 2018; Received in revised form 12 October 2018; Accepted 8 November 2018

Nomenclature

L	core length (frac.)
P	absolute pressure (bar)
$p\ (T_2)$	relative amount of measured T_2
PV_{inj}	pore volumes injected (frac.)
S_h	saturation of hydrate (frac.)
S_w	saturation of water (frac.)
T	temperature (°C)
T_2	time constant for the decay of transverse magnetization (ms)

cold aquifers results in immediate formation of hydrates in the near-well area and corresponding loss of injectivity (Ding and Liu, 2014; Gauteplass et al., 2018). Instead, CO_2 should be injected into aquifers where P, T conditions are outside of the hydrate stable region, but where the injected CO_2 later is introduced to hydrate forming conditions by the upward movement of CO_2 caused by buoyancy (Koide et al., 1995, 1997). Laboratory research shows that formation of CO_2 hydrates may act as a secondary seal in addition to stratigraphic and structural trapping (Tohidi et al., 2010; Kvamme et al., 2007). Further knowledge about the relative importance of CO_2 hydrate as a trapping mechanism is provided in this paper through direct visual observation of pore-scale hydrate growth patterns. Previous micromodel studies of CO_2 hydrate formation are mostly based on static fluid phases at the onset of growth (Hauge et al., 2016) or single-phase flow (Tohidi et al., 2011). Here, the effect of a moving CO_2 phase on hydrate formation characteristics is incorporated to simulate the movement of buoyant CO_2 in an aquifer. MR imaging is also applied to visualize the CO_2-drainage of water and subsequent formation of the hydrate seal on core-scale. This multiscale imaging approach enables us to couple the observations made of isolated events at micro-scale with Darcy-scale fluid flow.

2. Materials and methods

2.1. Micromodel visualization

Direct pore-level visualization of CO_2 hydrate blockage was performed by microscope observations of a transparent micromodel (Fig. 1). Based on a 2D thin-section of actual sandstone rock, the micromodel was etched (deep reactive ion etching) in silicon material with an average pore diameter of 100 µm and a constant vertical pore depth of 25 µm. Reproduction of actual pore bodies, pore necks and coordination numbers made the model suitable for flow and equilibria studies related to natural sediments (Song et al., 2014). The top layer was made of silica glass (SiO_2) to achieve necessary transparency, and the anodic bonding of the glass and the silicon wafer made the grain surfaces strongly water-wet (Buchgraber et al., 2012). The model was made to withstand a pore pressure of up to 150 bar without the need of any confinement pressure. Each corner of the model was connected with flow lines to enable injection of fluids and to monitor the pore pressure.

The pore space was completely saturated with distilled water and the temperature was reduced to 1.3 °C (± .1) by a custom-made cooling device; the micromodel was submerged in still water in an inner chamber while antifreeze was circulated through an adjacent outer chamber by a refrigerator bath (Neslab RTE17). The surrounding still water acted as a cooling medium and offered visual communication between the micromodel and the microscope (Nikon SMZ 1500) situated directly above the pore space. The pore pressure was set to 70 bar and maintained by constant pressure operation by a high-pressure pump (Quizix SP5200) connected to one corner of the model. Another pump, connected to the corner located diagonally from the water pump, was used to inject liquid CO_2 at constant volumetric rate of 0.5 mL/h. The subsequent displacement of water by CO_2 and crystallization of CO_2 hydrates were monitored and recorded by a camera (Nikon D7100) connected to the microscope. 2D hydrate growth rates were calculated using image analysis software (ImageJ) and the transmissibility of the pore space was evaluated by pressure recordings acquired from the pumps.

2.2. Core-scale MR imaging

A 4.7 T superconducting magnet (Bruker Biospec) was used to image the formation of CO_2 hydrate seals on a core-scale. MR (magnetic resonance) imaging is ideal to use for monitoring of hydrate growth, as MR signal from hydrogen protons in the solid hydrate structure is short lived and not acquired in standard spin-echo techniques. Conversion of

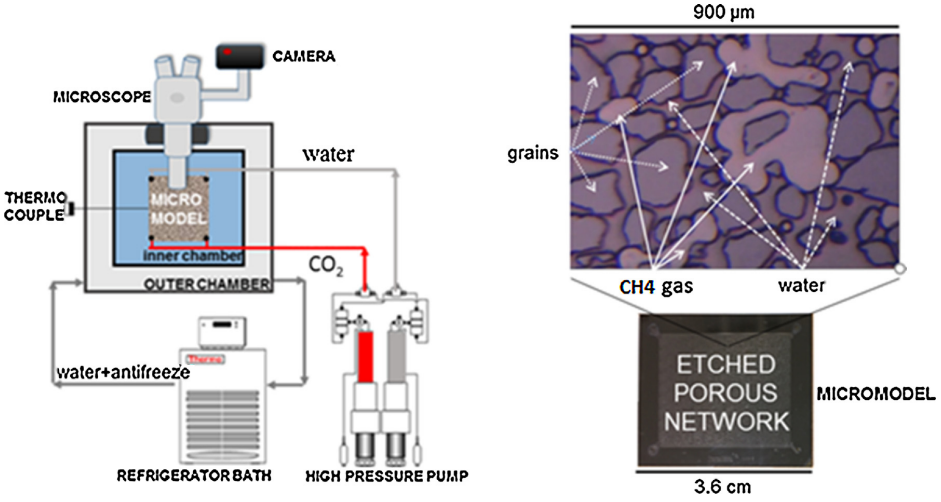

Fig. 1. Experimental set-up (left) and close-up image of micromodel saturated with water and methane gas (right) (Almenningen et al., 2017). The methane gas in the pore space is used for illustration purpose only. Liquid CO_2 was used in the experiments.

liquid water to solid constituent of the hydrate structure can simply be seen as a loss of MR signal (Ersland et al., 2010). The spin-echo scanning protocol RAREst (Rapid Acquisition with Relaxation Enhancement with short echo time) was used to ensure rapid acquisition of axial 2D images with an echo time of 6.24 ms and a rare factor of 2. A voxel size of 0.5 × 0.5 x 10 mm was chosen to resolve saturations on millimeter-scale with adequate signal-to-noise ratios. The MSME (Multi Slice – Multi Echo) protocol (echo time of 6.65 ms and 100 echoes in each T_2 decay) provided localized T_2 decay curves, which again was transformed to T_2 distributions by inverse Laplace transformation. Detailed descriptions of the two scanning protocols are found elsewhere (Gross et al., 2017).

The same injection scheme as for the micromodel study was implemented for the core-scale experiment (Fig. 2). A water-saturated Bentheim sandstone with average porosity of 0.23 (frac.) and permeability of 1.1 D (length = 10 cm and diameter = 6 cm), was used as porous media to mimic aquifer storage of CO_2. Bentheim sandstone consists of 96% quartz (Ramstad and Rueslåtten, 2013) and is strongly water-wet as the micromodel chip used in the pore-scale experiments. A non-magnetic core holder (CoreLab) with floating end-pieces and rubber sleeve surrounding both the core and the end-pieces, was pressurized with fluorinert (FC40) as the confining fluid. The 100% water-saturated core was gradually pressurized to 70 bar with distilled water and the effective stress (overburden) was maintained at 30 bar. The core holder was placed inside a custom-made cooling jacket where precooled air flowed through and allowed temperature control of ± .5 °C. After the temperature was set to around 2 °C, liquid CO_2 was injected from one side of the core at constant volumetric rate of 0.5 mL/min. The effluent side of the core was maintained at constant pressure (70 bar) by a back-pressure regulator. The subsequent displacement of water by CO_2 and crystallization of CO_2 hydrates were monitored and recorded by both mass balance calculations and MR imaging. Pressure recordings on each side of the core were used to quantify changes in permeability.

3. Results and discussion

In the core-scale experiment, the unfavorable viscosity ratio between liquid CO_2 (viscosity of 0.1 cP) and water (viscosity of 1.7 cP) led to early breakthrough of CO_2 and heterogeneous displacement during drainage (Fig. 3b). This emphasizes the importance of mobility control, i.e. controlling the viscosity and/or relative permeability of the injected CO_2, during geologic sequestration of CO_2. It is especially important in rocks with permeability contrasts in order to employ the full storage capacity of the reservoir. A total of 0.27 pore volumes (PV) of water were displaced after injecting 0.97 PV of CO_2. Further injection was hampered by nucleation of solid hydrates at the outlet end-piece and the injectivity decreased rapidly (Fig. 4). The hydrate growth continued throughout the entire core (Fig. 3d), both in regions drained by CO_2 and in regions still saturated with water (Fig. 3e). Diffusion of liquid CO_2 through the water phase enabled homogenous hydrate growth in areas not contacted by viscous displacement. The T_2 distribution curve shifted left during hydrate formation independent of initial fluid saturation (Fig. 5). A shift towards faster transverse relaxation, i.e. lower T_2 values, indicated an enhanced surface-to-volume ratio of the remaining liquid water. This was previously interpreted as an indication

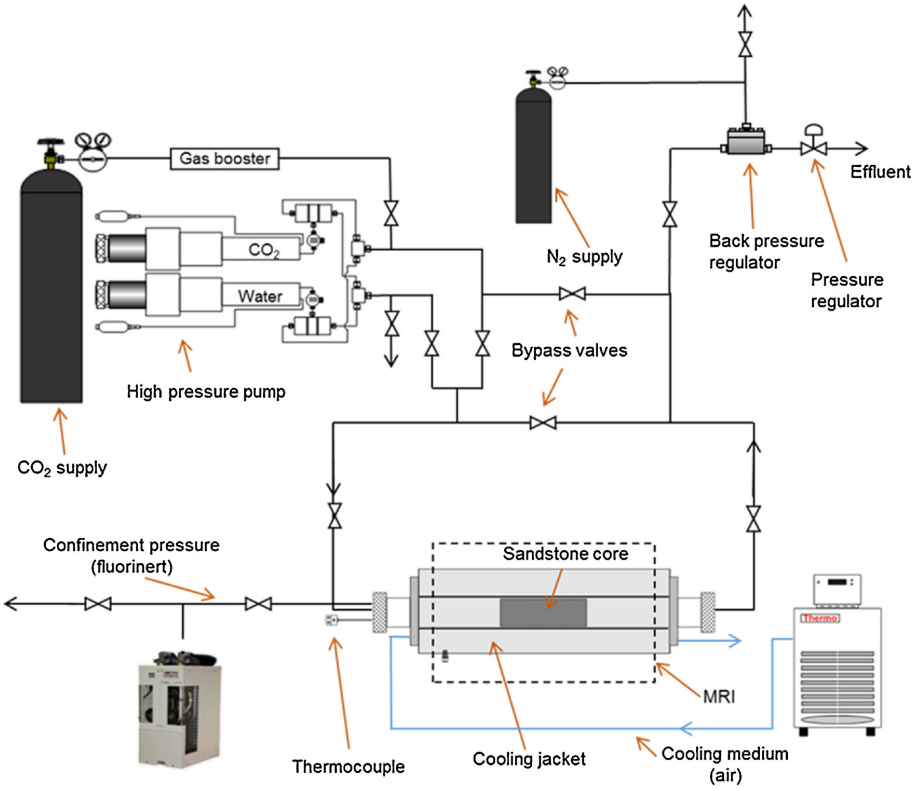

Fig. 2. Core-scale experimental set-up with MR imaging capabilities.

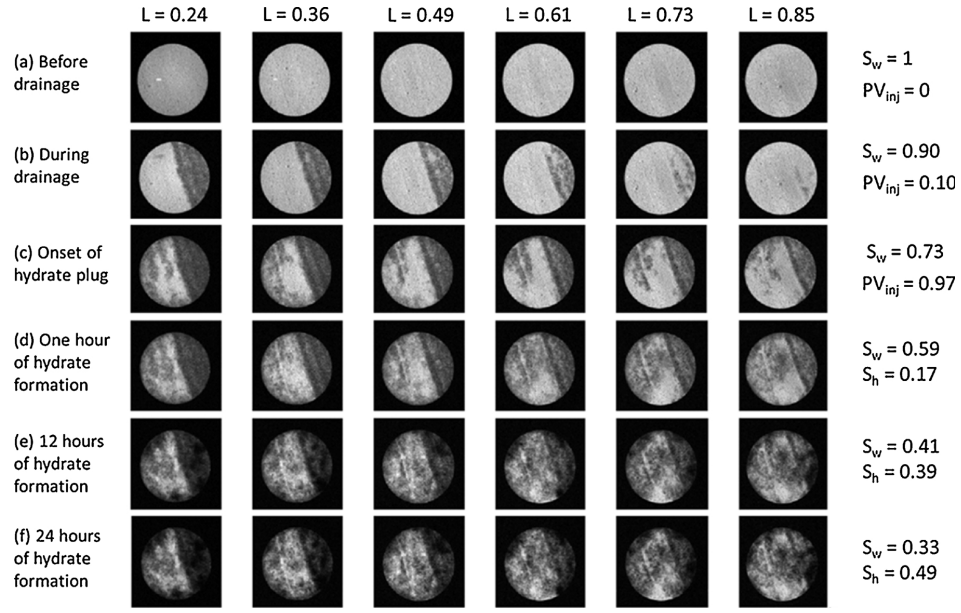

Fig. 3. Core-scale visualization of CO_2 hydrate growth during liquid CO_2 injection into a water-filled Bentheim sandstone core. Signal intensity (grey scale) relates to water saturation. Saturation values (right) reflect global fluid phase saturations in the entire core based on PVT data, where S_w denotes water saturation and S_h denotes hydrate saturation. The initial pressure was 70 bar and the temperature was approximately 2 °C. The drainage of water by CO_2 was highly heterogeneous (b) and led to a water saturation of 0.73 after injecting 0.97 PV of CO_2 (c). The hydrate plug initiated in the outlet end-piece (not shown) and eliminated the production of CO_2 and water. Continued hydrate growth throughout the pore network (d–f) resulted in a final hydrate saturation of 0.49.

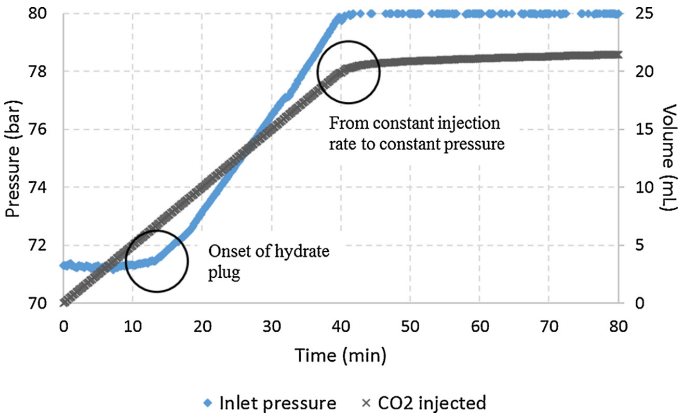

Fig. 4. Development of inlet pressure during liquid CO_2 injection into a water-filled Bentheim sandstone core. The initial pressure was 70 bar and kept constant at the outlet of the core by a back-pressure regulator. The temperature was approximately 2 °C. Hydrate formation led to an increase in differential pressure until the injection stopped at a differential pressure of 10 bar. No CO_2 or water was produced after the increase in differential pressure.

for pore-filling hydrate growth (Kleinberg et al., 2003). However, the relation between hydrate growth pattern and changes in the T_2 distribution is not straightforward as different configurations of the formed hydrate can yield the same shift in T_2 distribution. The final hydrate saturation ceased at 0.49 (frac.) after approximately 24 h of growth at constant pressure (Fig. 3f). The formed CO_2 hydrate effectively shielded the remaining pore water and inhibited further growth. The combined amount of liquid and hydrate-encapsulated CO_2 that was sequestered in the core was equivalent to 0.34 PV of liquid CO_2, an increase of 0.07 PV compared to the stored amount of liquid CO_2 after drainage only. The formed CO_2 hydrate provided increased storage capacity as well as increased storage security through effective flow restriction of the injected CO_2.

In the micromodel experiment, pore-level drainage of water by liquid CO_2 in sandstone pores led to residual water saturations of 0.20-0.30 (frac.), with local variations based on the governing capillary entry pressure (Fig. 6b). Hydrate growth initiated within few minutes after drainage. Nucleation of solid hydrates started at the curved liquid-liquid interface between CO_2 and water (Fig. 6c), where both components were readily available. The initial growth was slow and moved laterally into the water phase, contrary to the growth pattern observed for pore-scale methane hydrate where hydrate tended to surround and encapsulate the gas phase (Almenningen et al., 2018). After a period of 10–20 min with continuous CO_2 injection and little advancement of the localized hydrate fronts, complete crystallization of the water phase was brought about within only a minute (Fig. 6d). Hydrate front

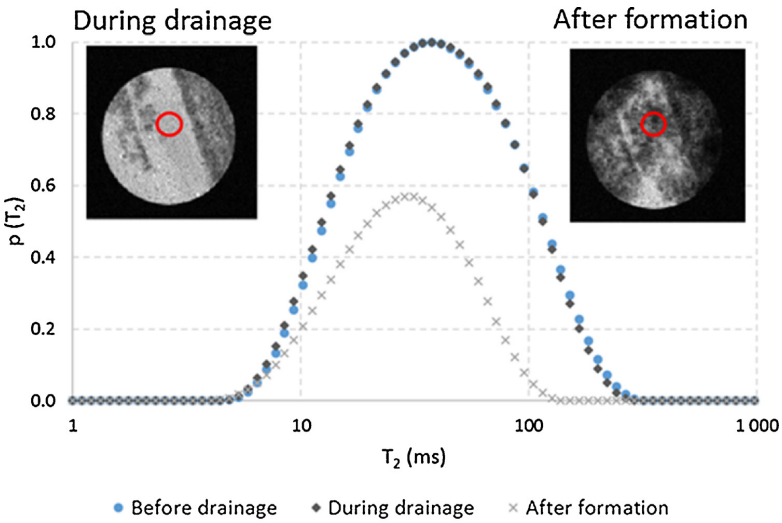

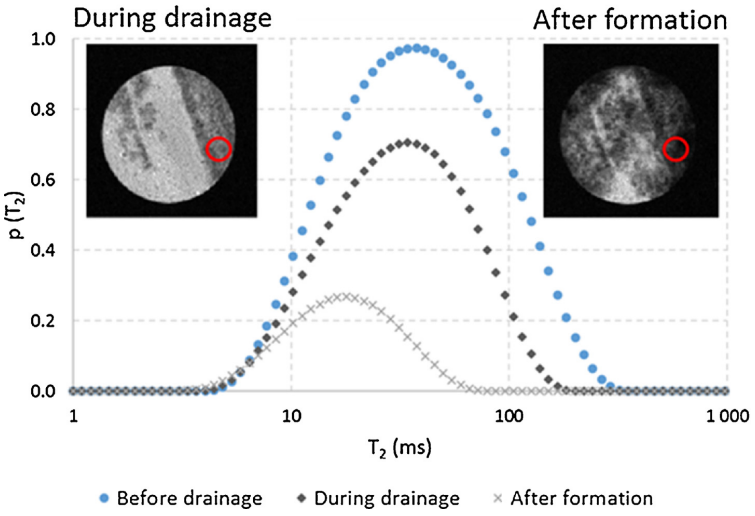

Fig. 5. Localized T_2 distribution before drainage, during drainage and after hydrate formation at the same cross-section of the core equivalent to L = 0.76. The distributions are normalized with respect to the amplitude of the 100% water saturation distribution. Top: T_2 distribution in an area not contacted by CO_2 during drainage (red circle). The amplitude of the distribution decreased and the mean shifted to the left during hydrate growth. Bottom: T_2 distribution in an area contacted by CO_2 during drainage (red circle). The amplitude of the distribution decreased and the mean shifted left as the CO_2 displaced water in the middle of pores. The same general trend was observed when hydrate formed.

movement was not observed; the hydrate crystallized simultaneously in water-filled pores independent of size. The injectivity was consequently reduced. However, careful examination of the images gave indication of the existence of thin water films between the solid hydrate and the pore wall, as is expected from theoretical considerations (Clennell et al., 1999) and previous observations (Tohidi et al., 2011). Further growth continued slowly into the stagnant CO_2 phase with a lateral speed in the order of 0.1 μm/s. The hydrate front did not propagate far before the growth ceased, seeming to lack sufficient supply of water to advance further into the CO_2 phase. The pore network was ultimately left with pore-filling liquid CO_2, which was completely immobilized by surrounding solid hydrates (Fig. 6e).

4. Concluding remarks

The drainage of water by liquid CO_2 and subsequent hydrate growth in sandstone pores were visualized on different length scales: 1) Micromodel studies of pore-level hydrate growth gave explicit knowledge of growth pattern and verified immobilization of liquid CO_2; 2) MR imaging of drainage at core-scale showed poor sweep efficiency of liquid CO_2 because of the unfavorable viscosity ratio between CO_2 and water. Subsequent hydrate growth in sandstone pores took place both in regions contacted by liquid CO_2 and in unswept regions with 100% water; homogenous hydrate growth evolved from dissolved CO_2 in the water phase. Both imaging techniques confirmed significant growth of hydrate when liquid CO_2 was injected into sandstone filled with unsaturated water, and demonstrated the potential for CO_2 hydrate to seal the system and immobilize liquid CO_2.

The reported results have implications for large-scale subsurface CO_2 storage in saline aquifers located partially within the CO_2 hydrate phase envelope. Upward migration of buoyant CO_2 will form a layer of solid hydrate with the pore water at the base of the hydrate stability

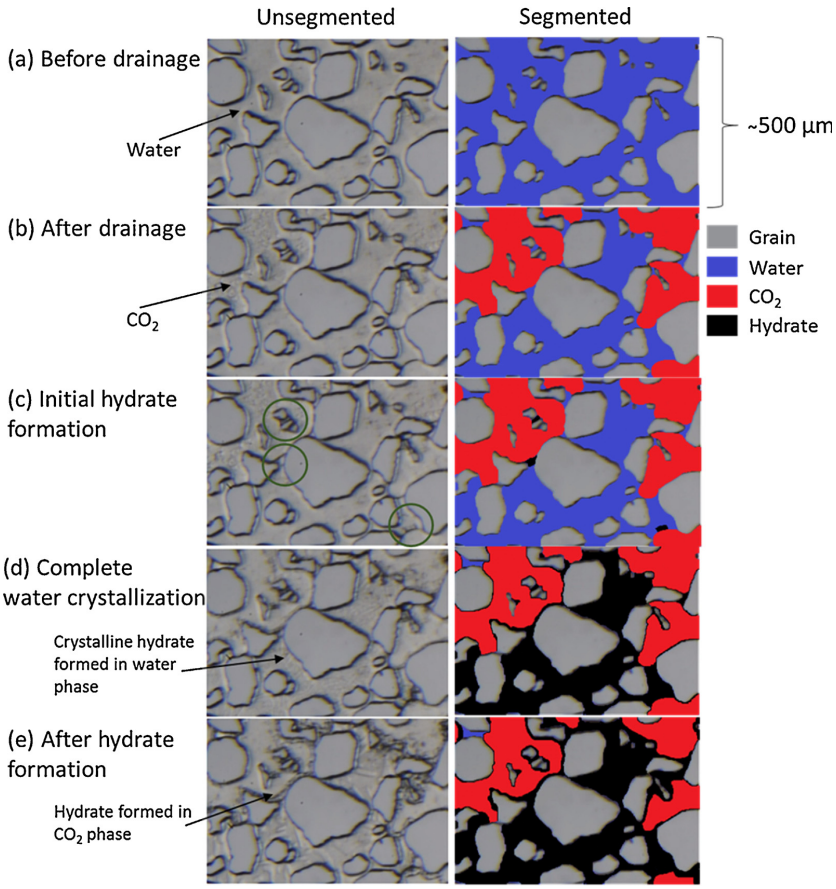

Fig. 6. Pore-scale visualization of CO_2 hydrate growth during liquid CO_2 injection into a water-filled sandstone analog. The initial pressure was 70 bar and the temperature was equal to 1.3 °C. Segmented images is added for clarity. CO_2 drained approximately 50% of the pore space in the field of view (b) which originally was filled with water (a). Hydrate started forming at the CO_2-water interface after ~2 min of injection (c). Crystalline hydrate formed in the water phase after ~14 min and the injectivity dropped to zero (d). The hydrate growth advanced toward the liquid CO_2 phase but ceased after ~40 min (e).

zone. Homogenous crystallization of the water phase creates an effective barrier for further viscous displacement. Continued supply of CO_2 from below will eventually spread laterally and the areal extent of the seal will increase. The formation of a physical hydrate barrier enables screening of aquifers, with no or little preexisting seals, as target for safe CO_2 storage. Still, the long-term integrity of the formed hydrate seal should be investigated for saline formation brine and with respect to hydrate redistribution and CO_2 diffusion via grain-coating water films.

Acknowledgements

The authors would like to acknowledge Equinor for financial support and the use of the MRI facility at Equinor's laboratories in Bergen. Some of the authors are indebted to the Research Council of Norway under Climit project: 255490. Live recordings of pore-scale displacement of water by CO_2 and subsequent crystallization of CO_2 hydrates are available online (DOI not yet provided).

References

IPCC, Climate Change, 2014. In: Core Writing Team, Pachauri, R.K., Meyer, L.A. (Eds.), Synthesis Report. Contribution of Working Groups I, II and III to the Fifth Assessment Report of the Intergovernmental Panel on Climate Change. IPCC, Geneva, Switzerland, pp. 151.

BP, 2017. BP Statistical Review of World Energy 2017. (Accessed 25 April 2018). https://www.bp.com/content/dam/bp/en/corporate/pdf/energy-economics/statistical-review-2017/bp-statistical-review-of-world-energy-2017-full-report.pdf.

IEA, 2017. World Energy Outlook 2017. (Accessed 25 April 2018). https://www.iea.org/weo2017/.

Bachu, S., 2000. Sequestration of CO2 in geological media: criteria and approach for site selection in response to climate change. Energy Convers. Manage. 41, 953–970.

Michael, K., Golab, A., Shulakova, V., Ennis-King, J., Allinson, G., Sharma, S., Aiken, T., 2010. Geological storage of CO2 in saline aquifers—a review of the experience from existing storage operations. Int. J. Greenh. Gas Control. 4, 659–667.

Baklid, A., Korbol, R., Owren, G., 1996. Sleipner vest CO2 disposal, CO2 injection into a shallow underground aquifer. In: Paper Presented at the SPE Annual Technical Conference and Exhibition. Denver Colorado, USA. https://doi.org/10.2118/36600-MS.

Benson, S., Cook, P., Anderson, J., Bachu, S., Nimir, H., Basu, B., Whittaker, S., 2005. IPCC Special Report on Carbon Dioxide Capture and Storage. Chapter 5 – Underground Geologic Storage. Cambridge University Press, New York.

Tohidi, B., Yang, J., Salehabadi, M., Anderson, R., Chapoy, A., 2010. CO2 hydrates could provide secondary safety factor in subsurface sequestration of CO2. Environ. Sci. Technol. 44, 1509–1514.

Zatsepina, O.Y., Pooladi-Darvish, M., 2011. CO2 -hydrate formation in depleted gas

reservoirs–A methodology for CO2 storage. Energy Procedia 4, 3949–3956.
Zatsepina, O.Y., Buffett, B.A., 2002. Nucleation of CO2-hydrate in a porous medium. Fluid Phase Equilib. 200, 263–275.
Ding, T., Liu, Y., 2014. Simulations and analysis of hydrate formation during CO2 injection into cold saline aquifers. Energy Procedia 63, 3030–3040.
Gauteplass, J., Almenningen, S., Ersland, G., Barth, T., 2018. Hydrate seal formation during laboratory CO2 injection in a cold aquifer. Int. J. Greenh. Gas Control. 78, 21–26.
Koide, H., Takahashi, M., Tsukamoto, H., Shindo, Y., 1995. Self-trapping mechanisms of carbon dioxide in the aquifer disposal. Energy Convers. Manage. 36, 505–508.
Koide, H., Takahashi, M., Shindo, Y., Tazaki, Y., Iijima, M., Ito, K., Omata, K., 1997. Hydrate formation in sediments in the sub-seabed disposal of CO2. Energy 22, 279–283.
Kvamme, B., Graue, A., Buanes, T., Kuznetsova, T., Ersland, G., 2007. Storage of CO2 in natural gas hydrate reservoirs and the effect of hydrate as an extra sealing in cold aquifers. Int. J. Greenh. Gas Control. 1, 236–246.
Hauge, L.P., Gauteplass, J., Høyland, M.D., Ersland, G., Kovscek, A., Fernø, M.A., 2016. Pore-level hydrate formation mechanisms using realistic rock structures in high-pressure silicon micromodels. Int. J. Greenh. Gas Control. 53, 178–186.
Tohidi, B., Anderson, R., Clennell, M.B., Burgass, R.W., Biderkab, A.B., 2011. Visual observation of gas-hydrate formation and dissociation in synthetic porous media by means of glass micromodels. Geology 29, 867–870.
Song, W., de Haas, T.W., Fadaei, H., Sinton, D., 2014. Chip-off-the-old-rock: the study of reservoir-relevant geological processes with real-rock micromodels. Lab Chip 14, 4382–4390.
Buchgraber, M., Castanier, L.M., Kovscek, A.R., 2012. Microvisual investigation of foam flow in ideal fractures: role of fracture aperture and surface roughness. Paper Presented at the SPE Annual Technical Conference and Exhibition. https://doi.org/10.2118/159430-MS. San Antonio, Texas, USA.
Almenningen, S., Flatlandsmo, J., Kovscek, A., Ersland, G., Fernø, M.A., 2017. Determination of pore-scale hydrate phase equilibria in sediments using lab-on-a-chip technology. Lab Chip 17, 4070–4076.
Ersland, G., Husebø, J., Graue, A., Baldwin, B.A., Howard, J., Stevens, J., 2010. Measuring gas hydrate formation and exchange with CO2 in Bentheim sandstone using MRI tomography. Chem. Eng. J. 158, 25–31.
Gross, D., Zick, K., Guthausen, G., 2017. Recent MRI and diffusion studies of food structures. Annu. Rep. NMR Spectrosc. 90, 145–197.
Ramstad, T., Rueslåtten, H., 2013. Pore scale numerical analysis for geological sequestration of CO2. Tech. Rep. 1–63.
Kleinberg, R.L., Flaum, C., Griffin, D.D., Brewer, P.G., Malby, G.E., Peltzer, E.T., Yesinowski, J.P., 2003. Deep sea NMR: Methane hydrate growth habit in porous media and its relationship to hydraulic permeability, deposit accumulation, and submarine slope stability. J. Geophys. Res. Solid Earth 108, 1–17.
Almenningen, S., Iden, E., Fernø, M.A., Ersland, G., 2018. Salinity effects on pore-scale methane gas hydrate dissociation. J. Geophys. Res. Solid Earth 123, 5599–5608.
Clennell, M.B., Hovland, M., Booth, J.S., Henry, P., Winters, W.J., 1999. Formation of natural gas hydrates in marine sediments: 1. Conceptual model of gas hydrate growth conditioned by host sediment properties. J. Geophys. Res. Solid Earth 104, 22985–23003.

VI

Chemical Engineering Journal 381 (2020) 122646

Contents lists available at ScienceDirect

Chemical Engineering Journal

journal homepage: www.elsevier.com/locate/cej

Multiscale investigation of CO_2 hydrate self-sealing potential for carbon geo-sequestration

Jarand Gauteplass[a,b,*], Stian Almenningen[b], Geir Ersland[b], Tanja Barth[a], Jinhai Yang[c], Antonin Chapoy[c]

[a] Department of Chemistry, University of Bergen, Norway
[b] Department of Physics and Technology, University of Bergen, Norway
[c] Institute of Petroleum Engineering, Heriot-Watt University, Edinburgh, UK

HIGHLIGHTS

- CO_2 hydrate reduces the risk of leakage from carbon geo-sequestration.
- Integrity of the CO_2 hydrate seal strongly depends on rock properties.
- Sandstone showed greater potential than limestone for hydrate seal development.
- CO_2 trapped by a combination of pore-spanning hydrate structures and capillary forces.

GRAPHICAL ABSTRACT

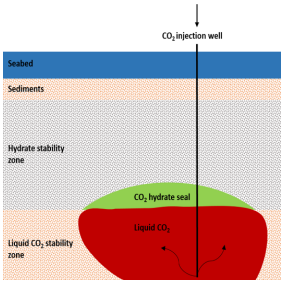

ARTICLE INFO

Keywords:
CO_2 storage
Hydrate seal
Leakage rate
Secondary safety factor
Pore-level visualization

ABSTRACT

Storage of liquid CO_2 in shallow geological formations is a recently proposed concept that can facilitate increased storage capacity and improved mobility control. If stored below the gas hydrate stability zone (GHSZ), unwanted vertical migration of CO_2 can be effectively inhibited by the formation of solid hydrate layers. Lowering the risks of CO_2 leakage to the atmosphere is instrumental to accelerate the implementation of full-scale carbon sequestration in the North Sea and elsewhere.

In the laboratory, we have successfully visualized CO_2 trapping phenomena, measured CO_2 leakage rates, and demonstrated that the integrity of the hydrate seal strongly depends on fluid-rock interactions and initial water distribution. CO_2 propagation in water-filled core samples has been monitored over a total of 140 days inside the GHSZ. Solid CO_2 hydrate formed and sealed the pore space in both homogeneous sandstone and heterogeneous limestone cores. However, the physical flow barrier developed considerably faster in sandstone (after 1.8 pore volumes – PV) compared to limestone (after 7.4 PV), with a factor ten reduced CO_2 leakage rate through the seal in favor of sandstone. Furthermore, pore-scale images of upward CO_2 migration verified trapping of CO_2 both as solid hydrate precipitation and as liquid CO_2 clusters made discontinuous and stabilized by capillary forces. Small-scale hydrate rearrangement followed initial formation, and caused temporarily dissociation of local hydrate structures without affecting the overall integrity of the seal. Our study suggests that a homogeneous, water-filled GHSZ directly above a CO_2 storage site can provide a secondary safety mechanism and significantly reduce the risk of CO_2 leakage.

* Corresponding author at: Department of Chemistry, University of Bergen, Norway.
E-mail address: Jarand.Gauteplass@uib.no (J. Gauteplass).

https://doi.org/10.1016/j.cej.2019.122646
Received 1 July 2019; Received in revised form 26 August 2019; Accepted 27 August 2019
Available online 28 August 2019

1. Introduction

Gas hydrates are naturally occurring clathrates formed in regions of high pressures and low temperatures, i.e. permafrost sediments and deep-sea continental shelves. During formation, water molecules encapsulate small-sized guest molecules such as methane (CH_4) or carbon dioxide (CO_2) in a network of cage-like structures [1]. Agglomeration of solid hydrates within the pore space leads to greatly reduced permeability and blockage of fluid flow [2,3]. Thus, development of flow barriers due to hydrate growth can be utilized as a sealing mechanism for subsurface CO_2 storage and reduce the likelihood of carbon leakage [4]. CO_2 is typically retained in geological formations by structural trapping, capillary trapping, fluid dissolution, and mineral reactions. The importance of each retention method changes over time [5]. Structural and capillary trapping are relevant from the onset of CO_2 injection, whereas the importance of dissolution and especially mineral trapping increases with time. In sediments below deep seabed locations (> 2800 m), CO_2 can also be retained in negative buoyancy zones [6]. The additional trapping mechanism of CO_2 as solid hydrate shows great potential for offshore Europe, where the predicted thickness of the CO_2 hydrate stability zone (HSZ) is nearly 0.5 km of the upper sediments [7]. Gas hydrate in nature (predominately permafrost, feather edge, and subglacial areas) may be a liability to global warming, however, the stability of offshore sedimentary hydrate at the base of the HSZ (CO_2 hydrate seal location) has generally low susceptibility to warming climate [8]. Solid CO_2 hydrate offers a high-density storage alternative to mineral precipitation which often suffers from slow geochemical reaction rates [9]. In contrast, CO_2 hydrate formation is quite fast ($<$ hours) and the kinetics are controlled by the availability of water and the thermal conductivity of the base rock [10]. Hydrate nucleation typically initiates at the fluid interfaces because here guest and water molecules are readily available [11]. Induction time for further massive growth can be long due to slow transport through initial hydrate films at the interfaces [12], and the induction time is also sensitive to the pore size distribution [13]. Increasing the driving forces (e.g. pressure, temperature, chemical potential) evidently accelerates CO_2 hydrate formation [14].

Storage of liquid CO_2 in the upper sediments potentially improves the storage capacity compared to conventional storage of supercritical CO_2 in deep formations. This is because liquid CO_2 is denser than supercritical CO_2, and the solubility of CO_2 in water increases with decreasing temperatures. Because CO_2 is usually transported in a liquid state, it can be injected without having to perform heating operations, and the extra weight in the injection well implies that a lower wellhead pressure is required compared to supercritical CO_2 [15]. Another benefit is the lower buoyancy of liquid CO_2, which reduces gravity segregation and risks of unwanted, upward CO_2 migration [7]. In addition, the macroscopic sweep efficiency increases as liquid CO_2 promotes a more favorable mobility ratio during brine displacement toward a production well [15]. Self-sealing CO_2 storage increases the stability and safety of carbon storage and can accelerate full-scale carbon capture and storage (CCS) deployment. CCS technologies are expected to contribute substantially toward transforming the energy sector and achieving the goals from the Paris Agreement [16]. The technologies target those industrial sectors that will continue to rely on hydrocarbons for decades to come, until renewable energy alternatives are cost-effective and fully competitive. Approximately 2/3 of the current global electricity production remains from fossil fuels [17].

One of the biggest impediment to widespread deployment of CCS is access to geological storage [18]. Therefore, CO_2 hydrate research in porous media is highly relevant because a top-sealing hydrate layer can potentially facilitate carbon storage in areas without known geological traps and cap rocks. Substantial research has been published on the four conventional CO_2 retention mechanisms mentioned above. However, existing research on sedimentary CO_2 hydrate is sparse, with a lot of knowledge gaps related to mechanisms and integrity of CO_2 hydrate seal. Most gas hydrate studies focuses on methane recovery from hydrate dissociation and to some extent from CO_2–CH_4 replacement [19] in geological formations. Forming hydrate layers at the base of the GHSZ as a mean to immobilize and retain upward CO_2 migration is less featured in existing literature. The concept was first presented in 1995 by Koide et al. [20]. Kvamme et al. [21] suggested that liquid transport channels separate hydrate from mineral surfaces, and may serve as distribution channels for CO_2 after initial hydrate formation. Furthermore, Tohidi et al. [22] verified experimentally significant CO_2 retention in hydrate-bearing unconsolidated sand without obvious reduction in permeability. More recently, Massah et al. [23] demonstrated high-density storage of CO_2 hydrate in silica sand (formed in a 5300 cm^3 pressure chamber), and Gauteplass et al. [3] investigated the effect of flow rate, temperature, and salinity on sealing capacity of CO_2 hydrates in consolidated sandstone. Increasing the temperature and salinity, had an adverse effect on formation time of CO_2 hydrate seals, while the effect of flow rate was insignificant in the low flow rate regime. However, others report no measurable effect of salinity on CO_2 hydrate induction time in porous media for certain range of salt concentration [24].

This article presents new insight into self-sealing CO_2 hydrate, particularly highlighting hydrate formation and sealing in multi-porosity and –permeability systems at ultra-low injection rates. To the best of the authors' knowledge, this is the first public research paper investigating the CO_2 hydrate seal potential in carbonates. Direct observations in micromodels complement conventional coreflooding experiments to incorporate pore-level interactions affecting fluid behavior at macro-scale. Micromodels have previously been employed to gain knowledge on pore-level hydrate growth of various guest molecules [25–29] and hydrate dissociation patterns [30,31]. The multiscale approach applied here evaluates the effect of initial water distribution and rock properties on CO_2 hydrate growth pattern and sealing potential.

2. Experimental section

2.1. Coreflooding experiments

Porous media of various properties (detailed in Table 1) were dried, vacuumed, and fully saturated with saline water. Magnetic resonance (MR) images were obtained of the limestone and sandstone cores ex situ to determine the initial water distribution. The superconductive magnet (Bruker BioSpec) has a magnetic field strength of 4.7 T (200 MHz), and the cores were imaged with a spin-echo scan protocol called RAREst (Rapid Acquisition with Relaxation Enhancement with short echo time). Axial two-dimensional slices were positioned uniformly throughout the length of the core, and the voxel resolution was set to $0.5 \times 0.5 \times 10$ mm. The unconsolidated sand pack (average grain size of 256 μm) was prepared by packing layers of dry silica sand grains uniformly within the sleeve by applying a steel piston of constant pressure. The sand column and the end pieces were separated by a

Table 1
Rock, brine, and saturation properties of various porous media used in this study.

	Edwards limestone	Bentheimer sandstone	Silica sand pack
Length, diameter	15.25 cm, 4.83 cm	14.83 cm, 5.12 cm	15.50 cm, 3.82 cm
Pore volume	71 mL	68 mL	72 mL
Porosity (frac.)	0.25	0.22	0.40
Permeability (Abs.)	0.08 D	1.1 D*	0.36 D
Brine composition	3.5 wt% ($CaCl_2$, NaCl)	3.5 wt% (NaCl)	3.5 wt% (NaCl)
Initial saturation	100% brine	100% brine	100% brine

* Value based on statistics from twin core plugs. Not explicitly measured in this study.

double-layered filter (coarse-to-fine) to avoid sand production.

Positioned inside the core holder, the pore volume was stepwise pressurized up to 70 bar with net effective stress of 30 bar. The core temperature was subsequently lowered to 4 °C, moving the system within the gas hydrate stability zone (GHSZ). A schematic of the experimental coreflooding setup is presented in Fig. 1. For consolidated cores, sampling of effluent CO_2 was conducted regularly after hydrate seal formation. Injection of liquid CO_2 was controlled by precise high-pressure pumps (Sanchez Technologies Stigma and Quizix Q5000 series), and a cooling jacket and circulating antifreeze ensured a uniform temperature distribution across the core length. Solid hydrate formation within the pore network occurred for all porous media during steady-state CO_2 injection. Pressure, volume, and temperature measurements were combined to determine the formation of CO_2 hydrates in the opaque system.

2.2. Micromodel experiments

Microfluidic experiments facilitate an excellent platform for direct visualization of pore-level fluid flow and distribution. Qualitative rather than quantitative aspects of such experiments should be highlighted due to the limited volume and number of pores in etched micromodels. A detailed schematic of the micromodel flow rig is shown in Fig. 2. The glass micromodel with etched pore network (68.5 × 5.0 mm) and uniform depth of 50 µm was positioned vertically inside the pressure chamber with main flow direction from bottom to top. The model was carefully pressurized with deionized water to approximately 70 bar (overburden 120 bar) and subsequent cooled by a cryostat (Grant LTC). Methylene blue (0.6 wt%) was added to the water phase for improved visualization and phase identification. The dye is excluded from formation of solid CO_2 hydrates due to molecular size constraints, and does not have any measurable effect on hydrate stability and wettability alterations [25,33]. The water initially occupying the pore space was displaced upward by liquid CO_2 (0.5 mL/hr) followed by hydrate formation. After hydrate formation, the injection mode was switched from constant flow rate to constant pressure of 100 bar, which was controlled by a Quizix pump (Q5000 series). This caused a pressure difference of almost 30 bar across the micromodel. A digital magnifying camera (MOS OPTEM zoom 125) connected to a PC obtained time-lapse images and videos of the field of view inside the pore network. The field of view was illuminated by Meiji Techno fiber optic lite source (FL150). Overburden, temperature, and inlet and outlet pressure were logged during the course of the experiments.

3. Results and discussion

3.1. Hydrate flow barriers

CO_2 migration over a total of 140 days in water-filled porous media of unique porosity, pore-size distribution and permeability were conducted in the laboratory. Interactions of CO_2 and brine at experimental conditions led to formation of solid hydrates, and subsequent build-up of injection pressure in silica sand, in Bentheimer sandstone, and in Edwards limestone material (Fig. 3). Initial hydrate formation occurred after approximately 0.2 PV of CO_2 injected for every core. In the case of unconsolidated silica sand, the initial build-up and collapse of pressure gradient was quickly followed by massive hydrate growth and a significant pressure drop across the sand pack. The hydrate seal was fully developed in the sand pack after 0.6 PV of CO_2 had advanced through the pores. In consolidated Bentheimer sandstone, a modest increase in pressure gradient was temporarily observed at 0.2 PV, however the seal did not fully develop until 1.8 PV of CO_2 was injected. The consolidated Edwards limestone experienced a substantial increase in pressure gradient up until 0.4 PV CO_2 injected, followed by a gradual

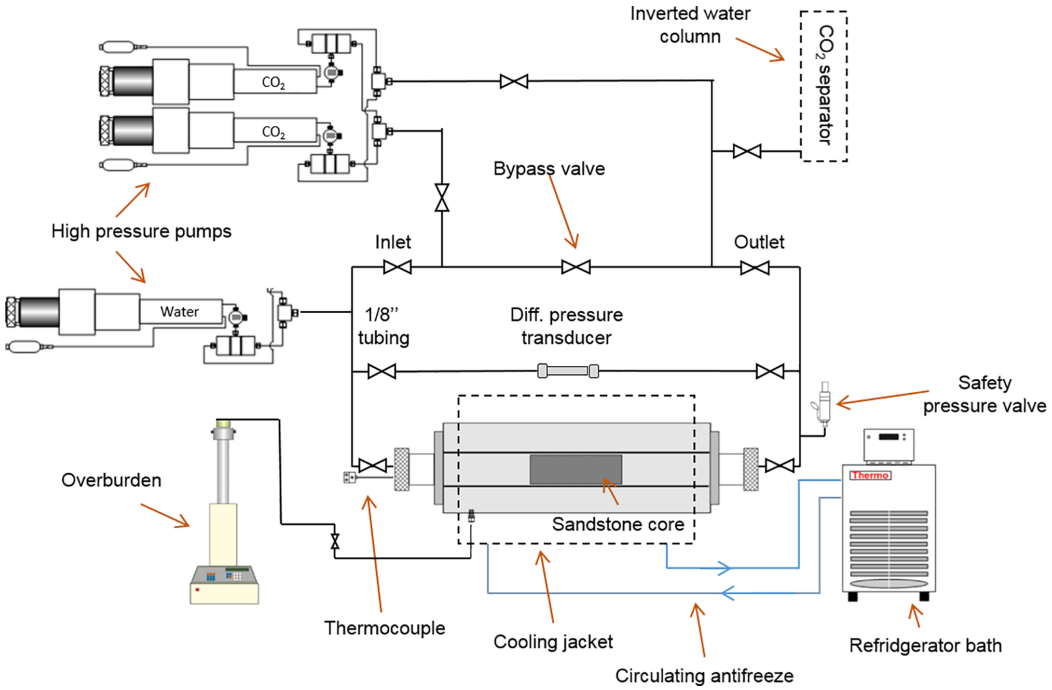

Fig. 1. Coreflooding setup designed for CO_2 hydrate formation at high pressures (70 bar) and low temperatures (4 °C). MR images were obtained ex situ. For consolidated cores, measurements of effluent CO_2 was conducted regularly after hydrate seal formation. Modified from Hågenvik [32].

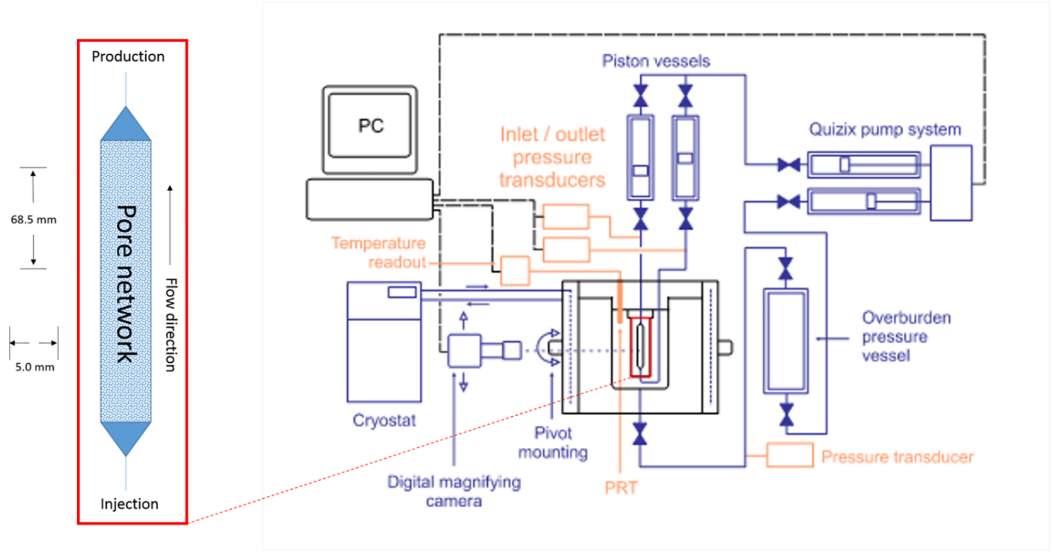

Fig. 2. Glass micromodel with etched pore network (left), and schematic overview of the micromodel rig including cryostat, digital camera with magnifier lens connected to PC, and Quizix Q5000 pump system. The micromodel is positioned vertically within the pressure cell. Modified from Tohidi et al. [34].

reestablishment of injectivity. A total of 7.4 PV of CO_2 was needed to obtain a viscous flow barrier in the limestone core, highlighting a significant increase of volumes CO_2 injected compared to quartz-based porous media. Our results corroborate recent studies on hydrate seal formation in Bentheimer sandstone [3], in tight (0.04 mD) reservoir sandstone [35], and gas permeability effects in hydrate-bearing silica sand [36]. Fast kinetics and short hydrate induction times are instrumental in order to convert upward flow of CO_2 to solid hydrate structures before the migration front escapes the GHSZ and reaches the seabed.

3.2. *Quantifying CO_2 escape rates*

Once CO_2 hydrate established flow discontinuities through the porous media, a significant pressure drop was imposed by the injection pump (15 bar differential pressure) to demonstrate the robustness of the

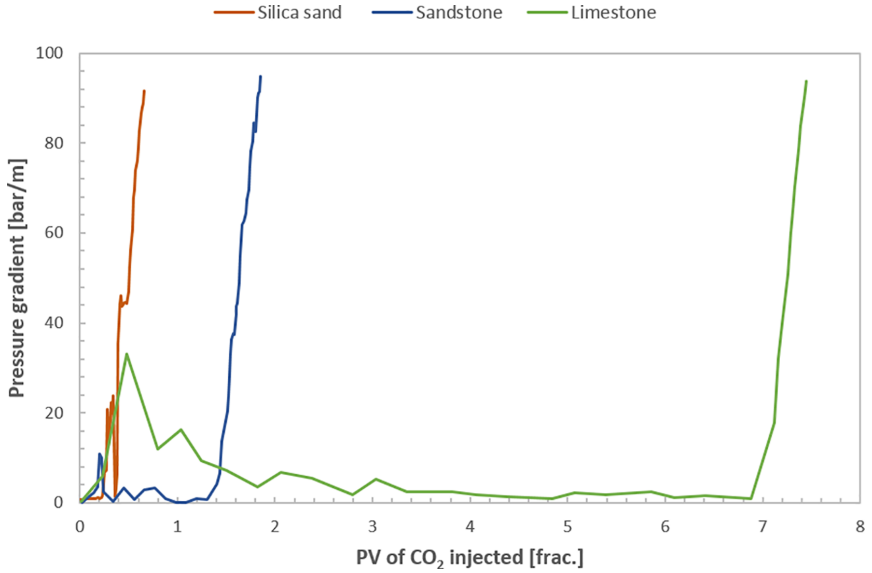

Fig. 3. Development of physical flow barriers in silica sand (0.6 PV), consolidated sandstone (1.8 PV) and consolidated limestone (7.4 PV) from CO_2 hydrate formation. Hydrates formed during continuous CO_2 migration through the pore network. All experiments were conducted at 4 °C and 70 bar, with the pore space initially filled with brine (3.5 wt% salinity). (For interpretation of the references to color in this figure legend, the reader is referred to the web version of this article.)

hydrate seal and compensate for natural pressure decline during conversion of liquid CO_2 to dense CO_2 hydrates. The hydrate seal withstood the stress test (> 80 bar/m) in all of the porous media (Fig. 3.) and showed no sign of bulk structural collapse at current experimental conditions. The consolidated sandstone and limestone cores were further used for investigation of the sealing properties of the formed hydrate layers by quantifying the CO_2 leakage rate across the seals (Table 2 and Fig. 4). After hydrate seal formation (1.8 PV – sandstone, 7.4 PV – limestone), the outlet production line was emptied for CO_2, as breakthrough occurred in both rocks before hydrates formed and sealed off the CO_2 migration paths. Accumulation of CO_2 at the outlet after this point was defined as 'escaped CO_2' and the volume was quantified regularly. The constant pressure drop was maintained during the sampling period. The limestone experiment ran for a total of 47 days, whereas the sandstone ran for 89 days due to a lower initial volumetric injection rate.

Daily CO_2 escape rates through hydrate layers in limestone (green columns) and sandstone (blue columns) are compared directly over a 21-days sampling period in Fig. 4. Though the absolute permeability of limestone (0.08 D) is much lower than sandstone (1.1 D), the CO_2 flow in sandstone was blocked earlier and more efficiently (lower leakage rate) compared to limestone. During the sampling period, seepage of CO_2 through the hydrate seal in sandstone ranged from 0.004 to 0.021 mL/day (average of 0.011 mL/day), whereas in limestone it ranged from 0.068 to 0.163 mL/day (average of 0.103 mL/day). These measurements indicate an order of magnitude higher leakage rate of CO_2 in limestone compared to sandstone. This pattern is consistent for every measuring period, and demonstrates a significant difference in hydrate sealing capacity in quartz-dominated versus calcite-dominated porous media. Furthermore, at 51 days after the hydrate barrier developed (not shown in Fig. 4), the CO_2 seepage rate stabilized at a reduced rate of 0.001 mL/day for the next 20 days in sandstone. Because the limestone experiment was ended 40 days after hydrate barrier formation, no sampling data is available for comparison to additional CO_2 escape rate reduction in sandstone. Focus should therefore be on the sampling period from 19 to 40 days after hydrate formation, where the two experiments are directly comparable and hydrate induction time is accounted for. However, based on the limestone trend line in Fig. 4, there are no indications of a sudden decrease in CO_2 seepage rate at current conditions.

The ability of solid hydrates to seal CO_2 migration paths in porous media depends on several parameters, including rock properties (mineral composition, pore-size distribution, wettability), and fluid properties (composition, saturation, distribution). Even though both media were initially 100% saturated with water prior to CO_2 injection, the pore connectivity caused the water distribution within the cores to vary significantly, as demonstrated in Fig. 5. Here, axial MR images are obtained from sandstone (left) and limestone (right) at fractional lengths L = 0.5 (middle) and L = 0.8 (outlet). Signal intensity is displayed in grey scale and areas of high water saturation (large pores) correlates with bright pixels. Initial water distribution in sandstone appears consistent in both the axial and longitudinal plane as opposed to limestone. In the heterogeneous limestone, large water-filled pores appear scattered and poorly connected. Dark pixels represents areas of minerals and micro pores where hydrate formation is unlikely due to severe capillary threshold pressures. CO_2 invasion in predominately large pores is followed by hydrate formation in areas where both phases are readily available. This facilitates development of a continuous hydrate seal in homogeneous sandstone pores, in contrast to a fragmented hydrate seal in heterogeneous limestone pores, based on the obtained MR images.

While formation of hydrate seals the pore space by reducing the effective porosity, mineral dissolution processes have the opposite effect. Carbonate materials are highly reactive in a CO_2-water system [37]. Limestone dissolution can cause substantial permeability and porosity increase [38], hence creating new potential CO_2 escape paths. Increase in local porosity due to dissolution in Edward limestone is shown in Fig. 6, by comparing pre- and post-experimental MR images. Axial water signal intensity (bright pixels) increased by a factor of 1.5 (at length 0.35) and by a factor of 2.4 (L = 0.43), highlighted with box A and B. In addition to interior porosity increase, mineral dissolution led to a substantial cavity on the core surface (box C). These microstructural changes further increased the number of CO_2 flow channels in the carbonate pore network. If availability of water is restrained in the newly formed channels, CO_2 hydrates cannot successfully form and seal off this zone. The combination of heterogeneous water distribution and local mineral dissolution is likely the main reason why CO_2 leakage rates were an order of magnitude higher in limestone than in sandstone. Dissolution processes after formation of hydrates were hampered by hydrate barriers blocking transportation of dissolved Ca^{2+} through the core sample.

In general, untreated (not aged with crude oil) sandstone and limestone cores are strongly water-wet in a CO_2-water system [39]. However, wettability alterations have been reported using supercritical CO_2 at high temperature and pressure in quartz [40], and at high salinity and pressure (200 bar) in calcite [41]. We simulate offshore shallow aquifer conditions in this paper using liquid CO_2, low temperatures and salinities, and moderate pressures. These conditions presumably make our sandstone and carbonate samples maintain their hydrophilic mineral surfaces and strongly water-wet properties throughout the experiments. Though the surface charge is opposite in the two cores due to the different mineral composition, water will still distribute itself along grain surfaces and in smaller pores, whereas non-wetting CO_2 will occupy the center of larger pores when overcoming the capillary threshold pressure. Furthermore, the activity of water molecules adjacent to mineral surfaces are lower compared to water molecules in the center of pores [42]. The reduced activity of water molecules implies that wetting films are preserved after hydrate formation, and may act as escape routes [21,25,42]. To investigate pore-level trapping mechanisms and fluid distribution channels, micromodels serving as an analogue to three-dimensional rocks were studied in the following section.

3.3. Pore-level CO_2 hydrate mechanisms

Direct visualization of upward CO_2 migration in a glass micromodel verified CO_2 trapping by hydrate formation. The initial CO_2 flow path was efficiently made discontinuous and the phase immobilized as CO_2 and water gradually converted to solid hydrate in the pore network (Fig. 7), resulting in a significant increase in inlet pressure. The injection pump was eventually set to constant pressure equal to 100 bar after 86 min, and the integrity of the hydrate seal was maintained throughout the experiment. The insets in Fig. 7 show preferred CO_2 (red color) flow paths after draining the water phase (blue color) from the largest pores in an upward direction. In such a flow regime, capillary

Table 2
Comparison of CO_2 sealing properties in carbonate and sandstone.

	Edwards limestone	Bentheimer sandstone
Pressure, Temperature	70 bar, 4 °C	70 bar, 4 °C
Flow rate	0.05 mL/min	0.005 mL/min
Hydrate barrier developed	After 7.4 PV inj (7 days)	After 1.8 PV inj (17 days)
Rate of escaped CO_2 (average)	0.10* mL/day	0.011* mL/day
Sampling period	21 days	21 days
Length of experiment	47 days	89 days
Total amount of CO_2 injected	631 mL	259 mL

* The original values measured at standard temperature and pressure conditions have been converted to experimental conditions by simple density calculations. The relative CO_2 escape rate (tenfold increase) relation should be highlighted rather than the absolute values.

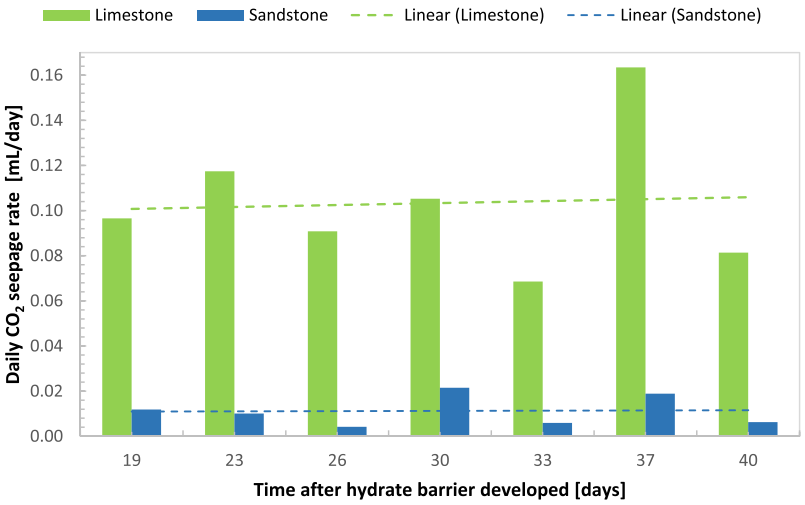

Fig. 4. Rate of CO_2 escaping the hydrate seal of respectively Edwards limestone and Bentheimer sandstone. The measured rate (mL/day) is averaged over the time period of sampling. Linear trend lines indicate average CO_2 escape rates of 0.10 mL/day (limestone) and 0.011 mL/day (sandstone) for the 21 days sample period. Both experiments were conducted at 4 °C and 70 bar, and with 3.5 wt% brine salinity. (For interpretation of the references to color in this figure legend, the reader is referred to the web version of this article.)

forces dominate the pore occupancy and filling sequences [43]. Some redistribution occurred in the network, where initial CO_2 migration paths were redirected by local snap-off events. These shifts led to capillary trapped CO_2 surrounded by water-filled pore throats. Hydrate growth (grey color) appeared uniformly throughout the network, rather than as a distinct hydrate front advancing through the pore space. Conversion to solid hydrates occurred predominately in larger pores initially occupied by liquid CO_2. The liquid CO_2 saturation effectively decreased during hydrate formation and the remaining liquid CO_2 was located in the upper production channel and in a few large pores in the model. A combination of pore-spanning hydrate layers and strong capillary forces stabilized the isolated pockets of liquid CO_2. The micro-visual data showed no sign of viscous displacement or substantial film flow after hydrate seal formation. The limiting fluid phase in the system is water, however full conversion of water to hydrate was not observed. Water, liquid CO_2 and hydrates co-existed due to lack of available host/guest molecules at the current locations. The formed CO_2 hydrate effectively shielded the remaining pore water and inhibited further growth. However, with time, molecular diffusion causes the free water to be fully saturated with CO_2. Substantial hydrate nucleation from CO_2 dissolved in water has been experimentally verified at similar conditions [44].

CO_2 hydrates precipitated in pores of various geometrical shapes and sizes. Initial formation in pores occupied by liquid CO_2 was soon followed by formation in smaller water-filled pores and pore-throats, where the induction time is typically longer [13]. On the scale of days the hydrate morphology changed from a dark, coarse opaque filling to higher degree of transparency due to rearrangement of the hydrate crystals [27]. Ostwald ripening stabilized the maturing hydrate structure [45,46]. Agglomeration of individual hydrate fronts took place, driven by the minimization of energy and surface-to-volume ratio. Massive hydrates spanned entire pore diameters without evidence of preserved water films (> 10 μm thickness) at current resolution. Hydrates appeared pore-filling as well as cementing within the field of view. However, shadowing effects near the pore walls may mask thin water films between grains and hydrate, as visualized at pore-scale [25,47]. In the upper production channel, hydrates were distributed as layers along the pore walls with liquid CO_2 occupying the center. This CO_2 was not converted to hydrates for the time investigated because of halted water supply.

The pressure drop imposed by the injection pump was maintained at 25 bar for several days during continuous visual monitoring. Fig. 8 shows evidence of small-scale hydrate dissociation at specific locations within the porous network (marked with red rings). The right image was obtained three days later under identical conditions. The dissociation temperature for the system was experimentally and

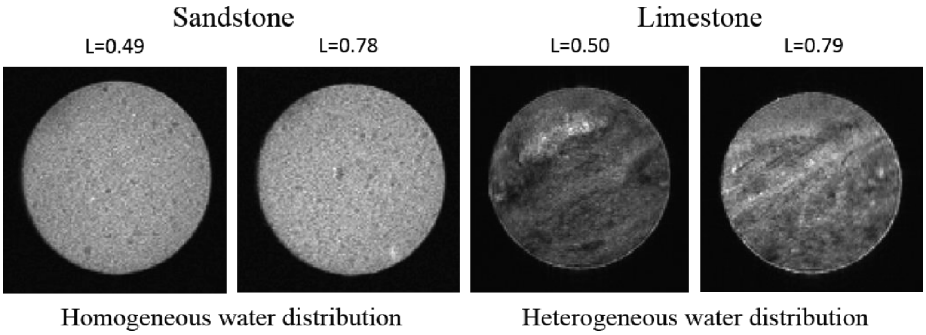

Fig. 5. Axial MR images (0.5 × 0.5 × 10 mm voxel resolution) of Bentheimer sandstone (left) and Edwards limestone (right) at two fractional core lengths obtained prior to CO_2 injection. Signal intensity is displayed in grey scale and areas of high water saturation correlates with bright pixels. Pore sizes and initial water distribution in the sandstone appears consistent in both the axial and longitudinal plane as opposed to the limestone core.

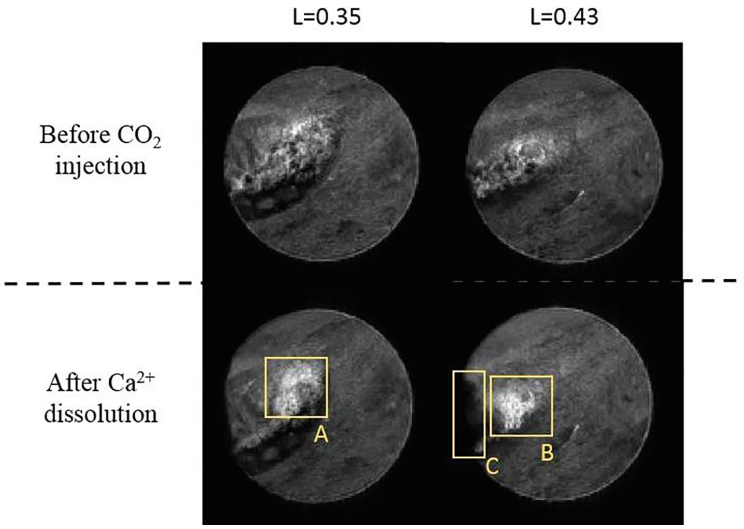

Fig. 6. Before and after images ($0.5 \times 0.5 \times 10$ mm voxel resolution) of CO_2 injection in Edwards limestone obtained by MRI. Mineral dissolution by the CO_2/brine solution led to large vugs to the left in the cross-sections resulting in areas of increased water saturation (box A and B) and completely dissolved limestone (box C) leaving a substantial cavity on the core surface. The lower images were obtained after the CO_2 experiment ended, and the sample had been re-saturated with 100% water to gain high signal intensity.

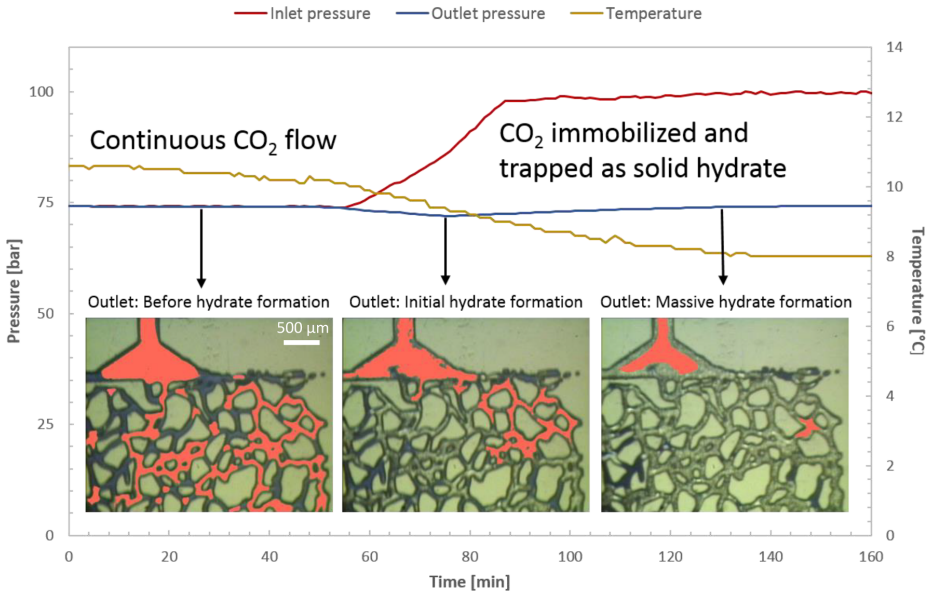

Fig. 7. Verification of pore-level CO_2 trapping. Inlet pressure increased during upward CO_2 migration as hydrates formed and blocked CO_2 flow paths in the pore network. Insets: Stepwise isolation and immobilization of CO_2 during hydrate formation (red color = liqCO_2, blue = water, grey = hydrate). (For interpretation of the references to color in this figure legend, the reader is referred to the web version of this article.)

numerically verified to be 2.0–2.5 °C higher than the current temperature. The few observations of local hydrate dissociation are believed to be part of gradual hydrate redistribution, with associated reformation at nearby places. Large and well-organized hydrate crystals grow at the expense of smaller crystals, and CO_2 and water are temporarily released through this rearrangement process. The inherent self-preserving property of hydrates [48] slowed further dissociation. The limited hydrate dissociation did not result in viscous mobilization of released CO_2 in pores due to high capillary threshold pressures and interstitial hydrate layers. Over time, hydrate re-formation of the liberated fluids will occur due to the favorable thermodynamic properties promoting stability. The dissociation of local hydrate structures and following hydrate formation had no measurable effect on the overall integrity of the solid hydrate seal under current conditions.

4. Conclusions

We have shown that the integrity of the CO_2 hydrate seal strongly depends on rock properties. Hydrate formed physical migration barriers in both consolidated and unconsolidated media, and the barriers

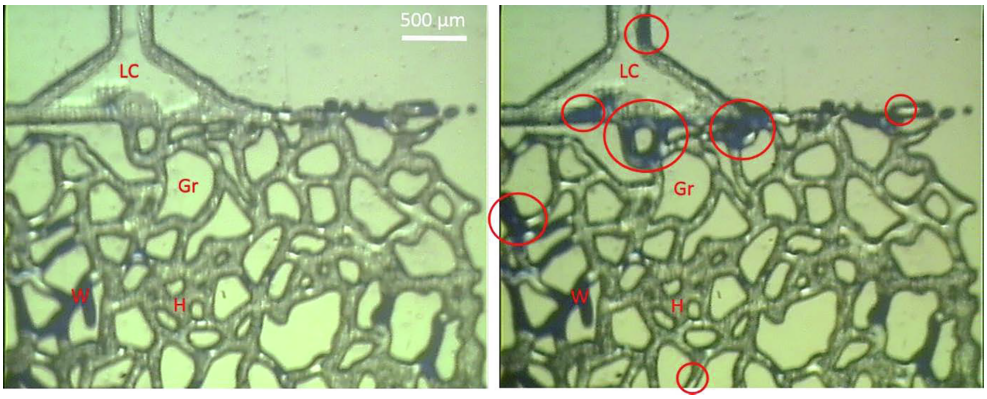

Fig. 8. Visual observations of local CO_2 hydrate dissociation with differential pressure of 25 bar and temperature equal to 8 °C. The left image was captured following the formation of the hydrate seal, whereas the right image is captured three days later under identical conditions. Red circles show specific areas of release of free water and liquid CO_2. The liquid CO_2 was trapped by capillary forces and interstitial hydrate layers, and the local hydrate dissociation did not affect the overall integrity of the CO_2 hydrate seal. Legends: Gr = Grains, LC = Liquid CO_2, W = Water, H = Hydrate. (For interpretation of the references to color in this figure legend, the reader is referred to the web version of this article.)

withstood significant pressure drops. However, the hydrate seal developed faster in sandstone than limestone, with a factor ten reduction in CO_2 leakage rate through the seal in favor of the sandstone. We believe this discrepancy in seal integrity can be ascribed to heterogeneous initial water (pore size) distribution and mineral dissolution in limestone, as supported by MRI data. Formation of vugs/wormholes in CO_2 invaded limestone pores, increased the effective porosity and the number of potential CO_2 escape channels. In sandstone where rock-fluid reactions were not observed, the CO_2 leakage rate was significantly reduced after 51 days of hydrate sealing, and remained constant for the rest of the measurements (20 additional days). Furthermore, pore-scale images of upward CO_2 migration verified trapping of CO_2 both as solid hydrate precipitation and as discontinuous liquid CO_2 clusters stabilized by capillary forces. Water, liquid CO_2, and hydrate phases were all observed to co-exist in pores within the GHSZ for the time investigated. Small-scale hydrate rearrangement followed initial formation, and caused temporarily dissociation of local hydrate structures without affecting the overall integrity of the seal. Our findings support higher CO_2 retention rates through hydrate layers in sandstone than limestone, and that CO_2 is immobilized by a combination of pore-spanning hydrate layers and capillary threshold in hydrophilic pore networks. If rock-fluid reactions are limited, a water-filled GHSZ directly above a CO_2 storage site can provide a secondary safety mechanism and significantly reduce the risk of CO_2 leakage toward the seabed and the atmosphere.

Acknowledgements

We gratefully acknowledge Equinor for access to MRI facilities in Bergen, Norway and financial support by the Research Council of Norway [grant number 255490] and by the Academia-agreement between Equinor and the University of Bergen.

References

[1] E.D. Sloan, Gas hydrates: review of physical/chemical properties, Energy Fuels 12 (2) (1998) 191–196.
[2] A.I. Evrenos, J.K. Heathman, J. Ralstin, Impermeation of porous media by forming hydrates in situ, J. Petrol. Technol. (1971.) 23(09).
[3] J. Gauteplass, S. Almenningen, G. Ersland, T. Barth, Hydrate seal formation during laboratory CO2 injection in a cold aquifer, Int. J. Greenhouse Gas Control 78 (2018) 21–26.
[4] H. Koide, M. Takahashi, Y. Shindo, Y. Tazaki, M. Iijima, K. Ito, N. Kimura, K. Omata, Hydrate formation in sediments in the sub-seabed disposal of CO2, Energy 22 (2) (1997) 279–283.
[5] S. Benson, D.R. Cole, CO2 sequestration in deep sedimentary formations, Elements 4 (5) (2008) 325–331.
[6] F. Qanbari, M. Pooladi-Darvish, S. Hamed Tabatabaie, S. Gerami, Storage of CO2 as hydrate beneath the ocean floor, Energy Procedia 4 (2011) 3997–4004.
[7] C.A. Rochelle, A.P. Camps, D. Long, A. Milodowski, K. Bateman, D. Gunn, P. Jackson, M.A. Lovell, J. Rees, Can CO2 hydrate assist in the underground storage of carbon dioxide? Geol. Soc., London, Special Publications 319 (1) (2009) 171–183.
[8] C.D. Ruppel, J.D. Kessler, The interaction of climate change and methane hydrates, Rev. Geophys. 55 (1) (2017) 126–168.
[9] W.D. Gunter, B. Wiwehar, E.H. Perkins, Aquifer disposal of CO2-rich greenhouse gases: extension of the time scale of experiment for CO2-sequestering reactions by geochemical modelling, Mineral. Petrol. 59 (1) (1997) 121–140.
[10] O.Y. Zatsepina, M. Pooladi-Darvish, Storage of CO2 hydrate in shallow gas reservoirs: pre- and post-injection periods, Greenhouse Gases Sci. Technol. 1 (3) (2011) 223–236.
[11] A.V. Palodkar, A.K. Jana, Formulating formation mechanism of natural gas hydrates, Sci. Rep. 7 (1) (2017) 6392.
[12] B. Kvamme, S.A. Aromada, N. Saeidi, Heterogeneous and homogeneous hydrate nucleation in CO2/water systems, J. Cryst. Growth 522 (2019) 160–174.
[13] X. Zhang, J. Li, Q. Wu, C. Wang, J. Nan, Experimental study on the effect of pore size on carbon dioxide hydrate formation and storage in porous media, J. Nat. Gas Sci. Eng. 25 (2015) 297–302.
[14] S.-P. Kang, J.-W. Lee, Kinetic behaviors of CO2 hydrates in porous media and effect of kinetic promoter on the formation kinetics, Chem. Eng. Sci. 65 (5) (2010) 1840–1845.
[15] V. Vilarrasa, O. Silva, J. Carrera, S. Olivella, Liquid CO2 injection for geological storage in deep saline aquifers, Int. J. Greenhouse Gas Control 14 (Supplement C) (2013) 84–96.
[16] P. Ekins, N. Hughes, S. Pye, M. Winning, R. Macrory, B. Milligan, S. Haszeldine, J. Watson, The role of CCS in meeting climate policy targets, 2017, Report by the UCL Institute for Sustainable Resources, p. 150.
[17] EASAC, Negative emission technologies: What role in meeting Paris Agreement targets? 2018, EASAC policy report 35. p. 39.
[18] OECD/IEA, 20 Years of Carbon Capture and Storage – Accelerating Future Deployment, International Energy Agency, 2016.
[19] G. Ersland, J. Husebø, A. Graue, B.A. Baldwin, J. Howard, J. Stevens, Measuring gas hydrate formation and exchange with CO2 in Bentheim sandstone using MRI tomography, Chem. Eng. J. 158 (1) (2010) 25–31.
[20] H. Koide, M. Takahashi, H. Tsukamoto, Y. Shindo, Self-trapping mechanisms of carbon dioxide in the aquifer disposal, Energy Convers. Manage. 36 (6) (1995) 505–508.
[21] B. Kvamme, A. Graue, T. Buanes, T. Kuznetsova, G. Ersland, Storage of CO2 in natural gas hydrate reservoirs and the effect of hydrate as an extra sealing in cold aquifers, Int. J. Greenhouse Gas Control 1 (2) (2007) 236–246.
[22] B. Tohidi, J. Yang, M. Salehabadi, R. Anderson, A. Chapoy, CO2 hydrates could provide secondary safety factor in subsurface sequestration of CO2, Environ. Sci. Technol. 44 (4) (2010) 1509–1514.
[23] M. Massah, D. Sun, H. Sharifi, P. Englezos, Demonstration of gas-hydrate assisted carbon dioxide storage through horizontal injection in lab-scale reservoir, J. Chem. Thermodyn. 117 (2018) 106–112.
[24] S.H.B. Yang, P. Babu, S.F.S. Chua, P. Linga, Carbon dioxide hydrate kinetics in porous media with and without salts, Appl. Energy 162 (2016) 1131–1140.
[25] B. Tohidi, R. Anderson, B. Clennell, R.W. Burgass, A. Biderkab, Visual observation of gas-hydrate formation and dissociation in synthetic porous media by means of

glass micromodels, Geology 29 (9) (2001) 867–870.
[26] D. Katsuki, R. Ohmura, T. Ebinuma, H. Narita, Formation, growth and ageing of clathrate hydrate crystals in a porous medium, Philos. Mag. 86 (12) (2006) 1753–1761.
[27] L.P. Hauge, J. Gauteplass, M.D. Høyland, G. Ersland, A. Kovscek, M.A. Fernø, Pore-level hydrate formation mechanisms using realistic rock structures in high-pressure silicon micromodels, Int. J. Greenhouse Gas Control 53 (2016) 178–186.
[28] S. Almenningen, J. Flatlandsmo, A.R. Kovscek, G. Ersland, M.A. Ferno, Determination of pore-scale hydrate phase equilibria in sediments using lab-on-a-chip technology, Lab Chip (2017).
[29] M. Muraoka, Y. Yamamoto, In situ chamber built for clarifying the relationship between methane hydrate crystal morphology and gas permeability in a thin glass micromodel cell, Rev. Sci. Instrum. 88 (6) (2017) 064503.
[30] D. Katsuki, R. Ohmura, T. Ebinuma, H. Narita, Visual observation of dissociation of methane hydrate crystals in a glass micro model: production and transfer of methane, J. Appl. Phys. 104 (8) (2008) 083514.
[31] S. Almenningen, E. Iden, M.A. Fernø, G. Ersland, Salinity effects on pore-scale methane gas hydrate dissociation, J. Geophys. Res. Solid Earth 123 (7) (2018) 5599–5608.
[32] C. Hågenvik, CO2 Injection in Hydrate Bearing Sandstone with Excess Water, University of Bergen, 2013, p. 117.
[33] M. Sohrabi, A. Danesh, D.H. Tehrani, M. Jamiolahmady, Microscopic mechanisms of oil recovery by near-miscible gas injection, Transp. Porous Media 72 (3) (2008) 351–367.
[34] B. Tohidi, R. Anderson, B. Clennell, J. Yang, A. Bashir, R.W. Burgess, Application of high pressure glass micromodels to gas hydrate studies, International Conference on Gas Hydrates – 4, Yokohama, 2002.
[35] S. Almenningen, P. Betlem, A. Hussain, S. Roy, K. Senger, G. Ersland, Demonstrating the potential of CO2 hydrate self-sealing in Svalbard, Arctic Norway, Int. J. Greenhouse Gas Control 89 (2019) 1–8.
[36] A. Okwananke, A. Hassanpouryouzband, M. Vasheghani Farahani, J. Yang, B. Tohidi, E. Chuvilin, V. Istomin, B. Bukhanov, Methane recovery from gas hydrate-bearing sediments: an experimental study on the gas permeation characteristics under varying pressure, J. Petrol. Sci. Eng. 180 (2019) 435–444.
[37] A.R. Lawter, N.P. Qafoku, R.M. Asmussen, D.H. Bacon, L. Zheng, C.F. Brown, Risk of geologic sequestration of CO2 to groundwater aquifers: current knowledge and remaining questions, Energy Procedia 114 (2017) 3052–3059.
[38] C. Noiriel, P. Gouze, D. Bernard, Investigation of porosity and permeability effects from microstructure changes during limestone dissolution, Geophys. Res. Lett. (24) (2004) 31.
[39] S. Iglauer, C.H. Pentland, A. Busch, CO2 wettability of seal and reservoir rocks and the implications for carbon geo-sequestration, Water Resour. Res. 51 (1) (2015) 729–774.
[40] S. Saraji, L. Goual, M. Piri, H. Plancher, Wettability of supercritical carbon dioxide/water/quartz systems: simultaneous measurement of contact angle and interfacial tension at reservoir conditions, Langmuir 29 (23) (2013) 6856–6866.
[41] M. Arif, M. Lebedev, A. Barifcani, S. Iglauer, CO2 storage in carbonates: wettability of calcite, Int. J. Greenhouse Gas Control 62 (2017) 113–121.
[42] M.B. Clennell, M. Hovland, J.S. Booth, P. Henry, W.J. Winters, Formation of natural gas hydrates in marine sediments: 1. Conceptual model of gas hydrate growth conditioned by host sediment properties, J. Geophys. Res.: Solid Earth 104 (B10) (1999) 22985–23003.
[43] J. Gauteplass, H. Follesø, A. Graue, A. Kovscek, M.A. Fernø, Visualization of pore-level displacement mechanisms during CO2 injection and EOR processes, EAGE IOR 2013 – 17th European Symposium on Improved Oil Recovery, St. Petersburg, Russia, (2013).
[44] S. Almenningen, J. Gauteplass, P. Fotland, G.L. Aastveit, T. Barth, G. Ersland, Visualization of hydrate formation during CO2 storage in water-saturated sandstone, Int. J. Greenhouse Gas Control 79 (2018) 272–278.
[45] M. Chaouachi, S.H. Neher, A. Falenty, W.F. Kuhs, Time resolved coarsening of clathrate crystals: the case of gas hydrates, Cryst. Growth Des. 17 (5) (2017) 2458–2472.
[46] X. Chen, D.N. Espinoza, Ostwald ripening changes the pore habit and spatial variability of clathrate hydrate, Fuel 214 (2018) 614–622.
[47] D. Sadeq, S. Iglauer, M. Lebedev, T. Rahman, Y. Zhang, A. Barifcani, Experimental pore-scale analysis of carbon dioxide hydrate in sandstone via X-Ray micro-computed tomography, Int. J. Greenhouse Gas Control 79 (2018) 73–82.
[48] T.-H. Kwon, G.-C. Cho, J.C. Santamarina, Gas hydrate dissociation in sediments: pressure-temperature evolution, Geochem. Geophys. Geosyst. (3) (2008) 9.

VII

International Journal of Greenhouse Gas Control 89 (2019) 1–8

Contents lists available at ScienceDirect

International Journal of Greenhouse Gas Control

journal homepage: www.elsevier.com/locate/ijggc

Demonstrating the potential of CO_2 hydrate self-sealing in Svalbard, Arctic Norway

Stian Almenningen[a,*], Peter Betlem[b], Arif Hussain[c], Srikumar Roy[c], Kim Senger[b], Geir Ersland[a]

[a] Department of Physics and Technology, University of Bergen, PO Box 7809, 5020, Bergen, Norway
[b] Department of Arctic Geology, University Centre in Svalbard, PO Box 156, 9171, Longyearbyen, Norway
[c] iCRAG, School of Earth Sciences, University College Dublin, Belfield, D04N2E5, Ireland

ARTICLE INFO

Keywords:
CCS in Longyearbyen, Norway
CO_2 hydrate formation
Extra (secondary) sealing

ABSTRACT

Here we report the potential self-sealing properties of CO_2 hydrate for the Longyearbyen CO_2 Lab's shallow aquifer in Svalbard, Arctic Norway, through hydrate formation experiments. The experiments were conducted on a 9 cm long core plug of a fluvio-deltaic sandstone of the Barremian Helvetiafjellet Formation recovered from a fully-cored research well in Adventdalen in Svalbard at a depth of 187 m. CO_2 injection into the brine-filled (1.0 wt.% NaCl) core plug was conducted at realistic reservoir conditions; the pore pressure was 20 bar and the temperature was 0.1 °C. Solid CO_2 hydrate formed in the core plug after injecting 0.40 pore volumes (frac.) of CO_2 and immediately reduced the apparent permeability to zero. A differential pressure across the core plug of 18 bar (200 bar/m) was sustained for 250 h without producing any CO_2 from the core plug. This demonstrates the potential of CO_2 hydrate formation as a secondary seal in settings with favorable CO_2 hydrate formation conditions in or above the reservoir. The results further indicate that the self-sealing nature of CO_2 hydrate should be considered while characterizing carbon sequestration reservoirs in both marine and permafrost-affected settings.

1. Introduction

Geological sequestration of anthropogenic CO_2 is acknowledged as an important contribution to mitigate the increase of global mean temperatures (IPCC, 2014). Different options exist for storing CO_2 in the subsurface: storage in depleted hydrocarbon reservoirs and salt caverns, oil displacement in reservoirs, displacement of methane and sequestration in coal beds, and storage in deep saline aquifers (Bachu, 2000). Injection of CO_2 into oil reservoirs has been used for decades to enhance the oil recovery (Blunt et al., 1993), providing an economic incentive for energy companies to inject and store CO_2. The largest potential of CO_2 sequestration in geological media is found in deep saline aquifers (Bachu, 2015), and several projects have already been initiated (Michael et al., 2010; Eiken et al., 2011). For instance, one million tons of liquid CO_2 separated offshore from a CO_2-rich produced gas are injected annually into the Utsira aquifer 800 m below the seabed in the northern North Sea (Baklid et al., 1996; Arts et al., 2008).

Sequestration of CO_2 in aquifers is not limited to geological formations offshore. Pilot-scale projects, where limited volumes of CO_2 were sequestered, were operated at, for instance, Ketzin in Germany (Kempka et al., 2010) and at Frio in Texas (Doughty et al., 2008). However, negative public opinion, concerns about groundwater contamination and NIMBY (not-in-my-backyard) opposition hamper large-scale onshore CO_2 sequestration, especially in Europe. Sub-permafrost CO_2 storage was envisioned on the Arctic archipelago of Svalbard, Norway (Braathen et al., 2012; Senger et al., 2015). The location is suitable given sedimentary successions directly beneath the settlement of Longyearbyen and the proximity to the coal-fueled power plant emitting approximately 70,000 tons of CO_2 annually (Senger et al., 2015). The main target aquifer comprises a 300 m thick sequence of tight, naturally fractured sandstones interbedded with siltstones and shales, where injectivity is ensured through fracture flow (Ogata et al., 2012; Mulrooney et al., 2019). The required storage capacity is limited compared to the expected storage capacity of the reservoir, given the modest CO_2 emissions from the power plant. Senger et al. (2015) estimated the volumetric capacity of low density CO_2 (61.15 kg/m^3) to be 0.004–3.9 million tons and high density CO_2 (807.76 kg/m^3) to be 0.052–52 million tons. The large volumetric difference is a function of different scenarios and the uncertain CO_2 phase dominated by the pressure conditions in the target reservoir. The storage aquifer is overlain by approximately 400 m of shale-dominated successions that provide sealing to the injected CO_2. The top seal integrity is evident

* Corresponding author.
E-mail address: stian.almenningen@uib.no (S. Almenningen).

https://doi.org/10.1016/j.ijggc.2019.06.010
Received 11 April 2019; Received in revised form 12 June 2019; Accepted 12 June 2019

Nomenclature

L	Core length (frac.)
P	Absolute pressure (bar)
PV	Pore volumes (frac.)
S_H	Saturation of hydrate (%)
t	Time (hours)
T	Temperature (°C)
T_2	Time constant for the decay of transverse magnetization (ms)
ΔP	Differential pressure across the core plug (bar)
Φ	Porosity (%)

from a large pressure differential across the cap rock, with hydrostatic to slightly overpressure within the overlying Helvetiafjellet Formation and severe underpressure in the lower part of the cap rock and the underlying reservoir sandstones (Senger et al., 2016; Birchall et al., 2018). Decompaction fracturing related to Cenozoic uplift and enhanced by periodic glaciations and deglaciations is considered the main contributor to the underpressure. The seal comprises the Lower Cretaceous Rurikfjellet Formation composed of shales intercalated with thin sandstone beds, and the Upper Jurassic-Lower Cretaceous Agardhfjellet Formation consisting of organic-rich, fossiliferous, shaly successions (Koevoets et al., 2018). The presence of natural thermogenic gas within the lower, most organic-rich part of the Agardhfjellet Formation suggests that "shale gas" may occur regionally. In places where the Agardhfjellet Formation lies within the gas hydrate stability zone (Betlem et al., 2019), this may lead to gas hydrate formation within the fracture systems of the shales. An upper aquifer, comprising the fluvial-dominated sandstones of the Lower Cretaceous Helvetiafjellet Formation (Grundvåg et al., 2019), serves as a possible test site for injection of gas-phase CO_2 in the shallow subsurface, as well as a possible monitoring layer immediately beneath the permafrost. In this study, we utilize a core plug from this upper aquifer.

Successful implementation of subsurface carbon storage relies on a geological seal that traps injected CO_2, but it has been advocated that CO_2 hydrate formation in the subsurface may immobilize upward migrating CO_2 that has leaked through a stratigraphic or structural trap (Koide et al., 1995, 1997). CO_2 hydrate consists of a lattice of water molecules arranged around a CO_2 guest molecule, and the solid compound is known to reduce permeability when forming inside a porous rock (Almenningen et al., 2019; Kleinberg et al., 2003). The concept of CO_2 immobilization by hydrate formation has been proven under laboratory conditions for Bentheim sandstone core plugs (Gauteplass et al., 2018) and in unconsolidated sand (Tohidi et al., 2010), showing the potential for CO_2 hydrate self-sealing in carbon sequestration offshore. In this paper, we investigate the same potential of CO_2 hydrate self-sealing in tight, consolidated rock from an onshore sub-permafrost setting. CO_2 hydrate formation is studied inside a core plug retrieved from the Lower Cretaceous Helvetiafjellet Formation overlying the proposed main seal in the CO_2 storage project in Longyearbyen. The 70 m thick, sandstone-dominated formation is located 100–200 m below the surface and lies partly within the permafrost region (Braathen et al., 2012), and overlaps with the estimated stability zone for both CO_2 and natural gas hydrates (Betlem et al., 2019). With theoretical conditions deemed suitable for CO_2 (and natural gas) hydrate formation, the aim of this work is to verify CO_2 hydrate formation at given reservoir conditions and demonstrate the self-immobilizing properties of CO_2 in this geological setting.

2. Experimental

2.1. Core plug analysis

The host sediment for the CO_2 injection was retrieved from well DH4 drilled in Adventdalen near Longyearbyen (Braathen et al., 2012). The cylindrical core plug with a diameter of 6.2 cm and length of 9 cm was recovered from a depth interval of 186.55–186.65 m in the Helvetiafjellet Formation. The local temperature was measured at 0.1 °C, while the local pressure is assumed to be near hydrostatic to slightly overpressured (Bælum et al., 2012). Fluid discharge analysis from a nearby pingo indicates salinity values of down to 0.5 wt.% NaCl (Hodson et al., 2019) in the upper sub-permafrost aquifer located close to the core interval. However, given the reservoir's coastal proximity, salinities of up to 3.5 wt.% NaCl are feasible, and salinity values of 1.0 wt.% NaCl were assumed for the experiments. The thermobaric conditions are favorable to CO_2 hydrate formation regardless of the salinity (Fig. 1).

The diameter of the core was reduced to 5.12 cm at the laboratory and the core was dried at 70 °C for 24 h to remove water from the pore space. The core plug was then purged under vacuum and re-saturated with brine containing 1.0 wt.% NaCl. The core was further pressurized to 60 bar with brine, and the absolute permeability was measured by constant volumetric flow rate injection and application of Darcy's law. Injection of several pore volumes of brine ensured that residual salt

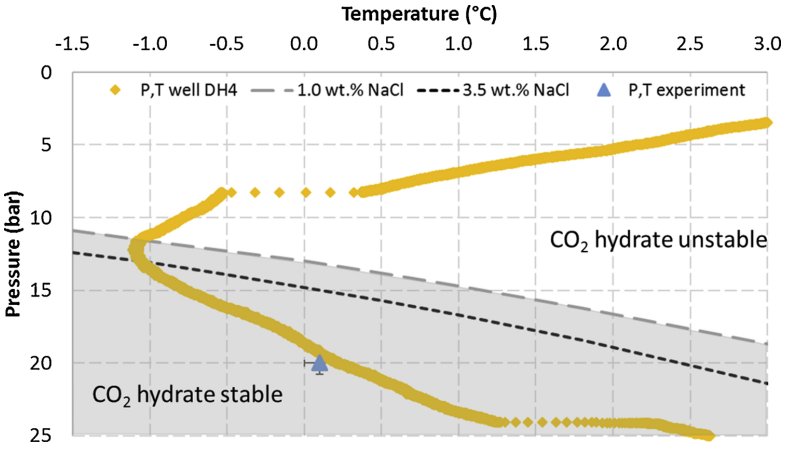

Fig. 1. Pressure and temperature (P,T) trace of well DH4. The experimental conditions (blue triangle) mimicked the actual P,T of the well at the depth interval where the core was retrieved from. The P,T conditions are favorable for CO_2 hydrate formation even at a pore-water salinity of 3.5 wt.% NaCl (similar to seawater). A salinity of 1.0 wt.% NaCl was used in the experiments in this work. The CO_2 hydrate stability curves are calculated with the CSMGem software (Colorado School of Mines, 2015).

potentially present after drying the core was displaced. The porosity was calculated by quantifying the mass of water that entered into the dry core. Magnetic resonance (MR) imaging (Bruker Biospec, 4.7 T) of the core plug saturated with water (the core plug was depressurized after the permeability measurement) provided spatial information on the initial water saturation. Standard spin-echo protocols, RAREst and MSME, were used for imaging and to provide local T_2 distributions, respectively (Mitchell et al., 2013). The spatial resolution of the images was 0.5 × 0.5 × 10 mm. Polished thin-sections and mm-scale rock chips were prepared from a neighboring core retrieved from the same well at a depth interval of 185.90–185.95 m. A blue dye was injected for porosity visualization and thin-sections were observed under Nikon Eclipse petrographic microscope to determine sandstone composition and texture. A Hitachi TM 3030Plus tabletop scanning electron microscope (SEM) fitted with Oxford EDS detector was also used for semi-quantitative elemental analysis. SEM was used consecutively to determine 3D pore structure and distribution of cemented phases (clays and quartz overgrowths) in pores. Element concentration maps were produced using the Oxford Instruments Aztec One (v.3.2) software.

2.2. Experimental set-up

A Hassler core holder connected to high-pressure pumps (ST Stigma 1000) was used to conduct the CO_2 injection experiments (Fig. 2). Separate pumps labelled injection and production were connected to each end of the core holder and facilitated injection of CO_2 and production of CO_2 and/or water. The overburden pressure was exerted by synthetic oil pressurized by a Teledyne Isco syringe pump. A rubber sleeve separated the core from the confinement oil and ensured that injected fluids passed through the interior of the core. A fixed end-piece with distribution grooves was connected to the inlet end of the core while an adjustable end-piece was used at the outlet end. The adjustable end-piece was pushed against the core end by the confinement oil and provided triaxial (radial and longitudinal) overburden pressure. Resistance measurements were enabled by an LCR meter (Hewlett-Packard) that was connected to electrodes attached to each of the two flow lines. Temperature control was provided by a refrigerator bath (Neslab RTE17) that circulated cooled antifreeze through a cooling jacket fitted outside the core holder. A temperature sensor (Omega) placed at the inlet core surface was used to monitor the temperature, and pressure readings were measured in each of the pumps.

2.3. Experimental procedure

The brine-saturated core was fitted inside the rubber sleeve and placed inside the core holder. The production pump, filled with brine, was used to pressurize the pore pressure to 20 bar while the overburden pressure simultaneously was pressurized to 50 bar. The temperature was set to 0.1 ± 0.1 °C and kept constant throughout the entire experiment. Gaseous CO_2 (> 99.999%) was injected by the injection pump from the inlet side of the core. The injected volumetric flow rate was initially 5 mL/min but was reduced to 0.1 mL/min after 30 min because of low injectivity. The production pump was set to constant pressure mode and produced the displaced water at constant pressure 20 bar. The differential pressure (injection pressure minus production pressure) and the resistance across the core were measured continuously to identify potential plugging due to CO_2 hydrate formation. A frequency of 10 kHz was used for resistance measurements, and the resistance values were later converted to resistivity by adjusting for the cross-sectional area and length of the core.

In the case of complete plugging of the core because of CO_2 hydrate formation, the long-term integrity of the hydrate plug was tested by applying a differential pressure across the core for ten days. The constant volumetric flow rate injection was then switched to constant pressure injection. A designated valve in the production flow line was used to sample the produced brine for CO_2. The core was shut-off from the production line during sampling and the brine in the production pump was depressurized into an inverted volumetric flask filled with water. Potential CO_2 in the production pump could then be quantified as gas bubbles in the volumetric flask. The production pump was re-pressurized with brine and connected back to the core after CO_2 sampling. The CO_2 hydrate plug was eventually dissociated by increasing the core temperature to room temperature while applying constant pressure. The amount of liberated CO_2 gas during dissociation was quantified and used to estimate the saturation of the hydrate plug. A hydration number of 6.2 was assumed for the CO_2 hydrate (Udachin et al., 2001).

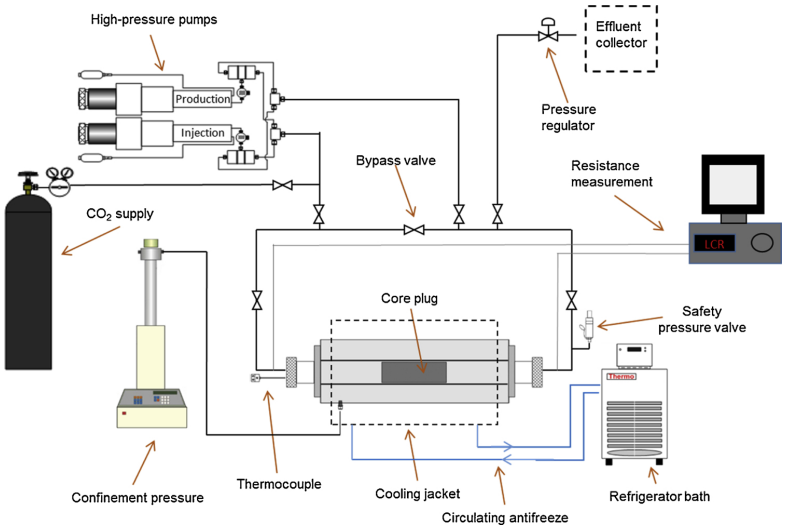

Fig. 2. Schematic of experimental design including core holder, high-pressure pumps, refrigerator bath, and LCR meter. Modified from Hågenvik (2013).

3. Results and discussion

3.1. Core plug properties

The core sample retrieved from the Helvetiafjellet Formation consisted of well-sorted, medium-grained, quartz-arenite sandstone. The quartz grains were rounded to sub-rounded and dominantly monocrystalline, with no significant fluid inclusion features (Fig. 3a and b). Most of the quartz grains exhibited undulose extinction, which was related to grain-to-grain contacts. The sandstone was quartz-cemented and showed well-developed syntaxial overgrowths (Fig. 3d) which may act as primary barrier to fluid flow. The sample was clay-poor (< 3% clay matrix), however a small proportion of dark brown to black, moderately compacted sedimentary shale fragments were observed. The shale fragments indicated ductile deformation and may occasionally block the pore space. The porosity was dominantly intergranular, with limited secondary grain dissolution porosity. Scattered rare traces of diagenetic framboidal pyrite were also observed.

The SEM-EDS results were consistent with petrographic observations and showed that the core was predominantly composed of Si (35.5 wt.%) with a very nominal contribution (< 1%) from phyllosilicate minerals, *i.e.* Al (0.3 wt.%) and K (0.1 wt.%). The concentration of other important sandstone forming minerals, like Fe, Mg, and K, was very low (perhaps below detection limit of the EDS detector) and was indicative of an overall quartzitic nature of the Helvetiafjellet Formation.

The porosity of the core plug was measured to 5.6 ± 0.1%, with an average grain density of 2.61 g/cm^3 and average grain size of 395 µm. The absolute permeability to water was measured to 0.04 ± 0.01 mD, in line with previous studies of the interval, *e.g.* Bjørlykke et al. (1979). The initial distribution of water was visualized by MR imaging (Fig. 4). The gray-scale images represent porosity maps since the core was assumed completely filled with water. The center of the middle parts of the core was lacking water compared with the rest of the core because of lower porosity in that area. The average T_2 and the area under the T_2 distribution were lower in the middle parts of the core indicating tighter pores here. Heterogeneities were also observed within the same cross-section of the core (L = 0.06, Fig. 4). The T_2 distribution was obtained for three different areas in this cross-section and showed significant discrepancies. One area (blue circle, Fig. 4) had a large intensity with an average T_2 of 2.9 ms. This area corresponds to one of the heterogeneities that is observed at the top of the core plug in Fig. 4c. These features were lithic conglomerates consisting primarily of mudstone filled with brine. The short relaxation time measured in these features reflects the small grain sizes of mudstone. A second area (red circle, Fig. 4) representing the main sandstone had a low intensity with an average T_2 of 8.4 ms. The subsequent CO_2 injection was not aided by *in situ* imaging of the core, but an unstable displacement of water by CO_2 was expected because of the unfavorable mobility ratio between CO_2 and water and the heterogeneous nature of the core plug.

3.2. Initial CO_2 hydrate plug

The initial CO_2 injection with constant volumetric rate equal to 5.0 mL/min led to an immediate increase of the injection pressure because of the low permeability of the core plug (Fig. 5). The injection rate was subsequently reduced to 0.1 mL/min, but the differential pressure (injection pressure minus production pressure) continued to increase as only 0.01 mL/min of water was being produced at the current differential pressure. The production rate increased slowly as the injection pressure increased, and the CO_2/water front arrived at the inlet core end after 6 h of injection. The low permeability of the core and corresponding low flow rate ensured that the temperature of the core was maintained at constant T = 0.1 ± .1 °C throughout the injection process. Additional four hours of CO_2 injection were sustained, equivalent of displacing 0.40 PV (frac.) of water by CO_2, before the CO_2 hydrate plug formed and abruptly diminished the flow through the core plug. The CO_2 hydrate formation was concurrently verified by no water production, increase in differential pressure, and increase in resistivity across the core plug (Fig. 5). The resistivity equipment malfunctioned during the first ten hours of the injection, but the resistivity was obtained immediately prior to and during hydrate plugging. The abrupt increase in resistivity across the length of the core verified conversion of liquid water to solid CO_2 hydrate inside the core plug. A CO_2 hydrate

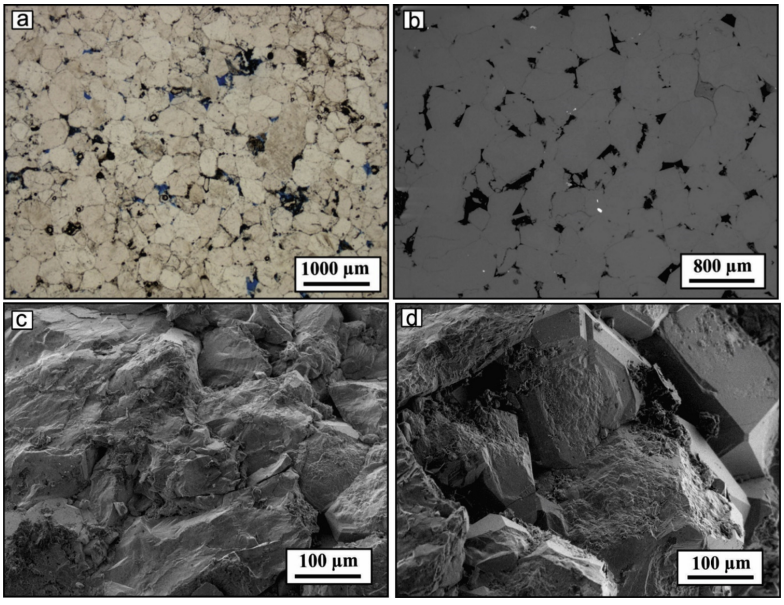

Fig. 3. a) Plane-polarized light photomicrograph of a thin-section from the lower part of the Helvetiafjellet Formation. The rock consisted of clean, well-sorted, medium-grained quartz arenite. b) BSE image showing the quartz-rich nature of the rock. The black spaces correspond to intergranular porosity whereas scattered white spots show framboidal pyrite. c) Pore-scale image of sandstone with d) well-developed syntaxial quartz overgrowths.

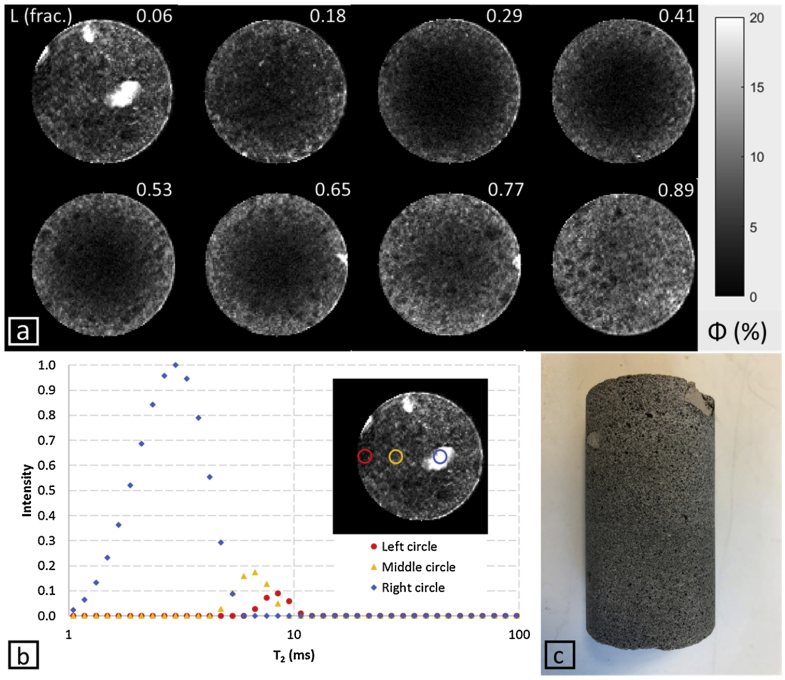

Fig. 4. a) Porosity map in gray-scale of eight different cross-sections of the core acquired from MR imaging. b) T_2 distributions from three different areas in the same cross-section of the core. Each intensity value is scaled to the peak intensity of the right area (blue diamonds). c) Photograph of the core plug.

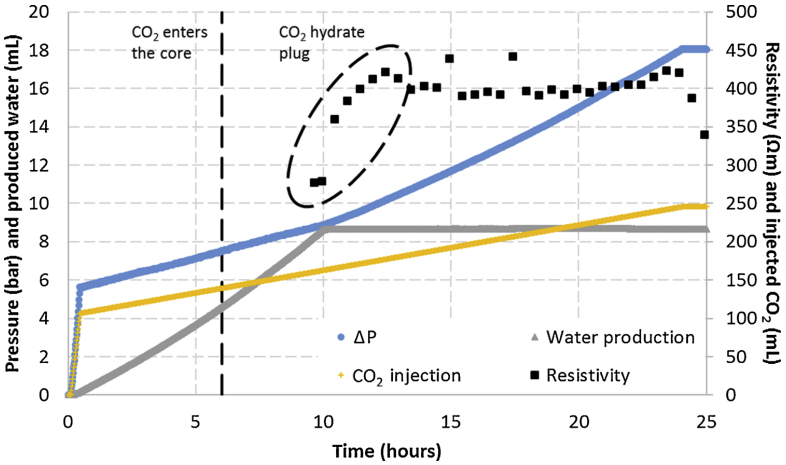

Fig. 5. Formation of CO_2 hydrate plug during CO_2 injection into water-filled core at T = 0.1 °C and P = 20 bar. The injected CO_2 was quickly pressurized to 26 bar (ΔP = 6 bar) and the differential pressure (blue circles) continued to increase as the CO_2 was injected with constant volumetric rate equal to 0.1 mL/min (yellow pluses). The injected CO_2 entered the core after 6 h, and a CO_2 hydrate plug formed after 0.40 PV (frac.) of CO_2 was injected into the core at t = 10 h. The formed CO_2 hydrate plug abruptly ended the water production (gray triangles) and increased the resistivity across the core (black squares).

plug forming only in the flow line or in the inlet end-piece contacting the core end would on the contrary not affect the resistivity measurements across the core plug.

The stability pressure of CO_2 hydrate at $T = 0.1$ °C in equilibrium with 1.0 wt.% NaCl water is 13.2 bar according to the CSMGem software (Colorado School of Mines, 2015). The initial pore-water pressure of 20 bar was already within the hydrate stability region, however, the CO_2 hydrate did not form until after four hours of CO_2 flow in the core. This time period between the moment at which the P,T conditions of hydrate formation is reached until hydrate growth begins is called the induction time. The induction time could vary stochastically from one hydrate formation to another (Sloan and Koh, 2008). In this particular CO_2 injection scheme, the CO_2 hydrate formed and plugged the flow path through the core before CO_2 broke through at the production side of the core. A core with length close to 9 cm was sufficient to produce a layer of impermeable CO_2 hydrate that effectively stopped the CO_2 from reaching the production pump. Similar CO_2 injection experiments on Bentheim sandstone resulted in the formation of CO_2 hydrate plugs, but usually the CO_2 hydrate plug formed at a later stage of the injection after CO_2 broke through the end of the core (Gauteplass et al., 2018).

Bentheim sandstone consists of more than 95% quartz (Ramstad and Rueslåtten, 2013) and has a porosity and permeability of 23–24% and 1.1–1.9 D, respectively (Almenningen et al., 2019). The lower permeability and tighter pores of the core plug from Helvetiafjellet Formation used in this study are likely to have led to more effective CO_2 hydrate sealing and a lower induction time.

The CO_2 was injected with constant volumetric rate of 0.1 mL/min for close to 15 h after the CO_2 hydrate plug formed (t = 25 h, Fig. 5), which increased the injection pressure to 38 bar. The CO_2 injection was then switched to constant pressure control, while the production pressure was kept constant to 20 bar. The induced differential pressure of 18 bar was maintained for close to 250 h to investigate the long-term stability of the CO_2 hydrate plug (Fig. 6). Neither was water produced nor CO_2 injected during this time span. The production pump was sampled twice for CO_2 after 100 and 250 h, but no CO_2 was found in the production water. The resistivity declined monotonically during the no-flow period, and may be attributed to CO_2 dissolving in the pore water with subsequent formation of carbonic acid and dissociation into conducting ions. However, adding conductive ions from CO_2 dissolution is expected to decrease the brine conductivity for high salt concentrations (Börner et al., 2015). Redistribution of the formed hydrate phase may also have an impact on the conductivity by affecting the tortuosity of the conducting brine (Hauge et al., 2016).

3.3. Second CO_2 hydrate plug

The successful CO_2 hydrate self-sealing at 20 bar was followed by a sensitivity analysis of the effect of pore pressure. The existing CO_2 hydrate plug was dissociated by reducing the injection and production pressure to 11 and 5 bar, respectively. The displacement of water by CO_2 was resumed (Fig. 7), and eventually the CO_2 broke through the core and water production was replaced by CO_2 production. After 20 h, the injection and production pressure were increased to 18 and 10 bar, respectively. The injected CO_2 was pressurized above the hydrate stability pressure of 13.2 bar, and the pressure dropped linearly through the length of the core plug to the production pressure below the hydrate stability pressure. The CO_2 flow remained constant for 20 h during this pressure condition and no CO_2 hydrate formed. The pressure was then further increased to 20 bar for the injection pressure and 15 bar for the production pressure. This led to an immediate formation of CO_2 hydrate and the pore space was again blocked for CO_2 flow. The CO_2 hydrate formed a flow barrier independent of whether CO_2 displaced water in a fully water saturated core, or CO_2 flowed through already established flow channels in conjunction with residual water. The saturation history of the core was insignificant as long as the P,T conditions were favorable for hydrate formation.

The core remained plugged for 450 h and no CO_2 was injected nor produced in this time period (Fig. 8). The production pump was already filled with CO_2 by the time the hydrate plug formed and explicit CO_2 sampling was therefore not performed during the long-term stability testing. The resistivity response was similar as to the initial long-term test and showed a steady decline during the no-flow period.

Thermal stimulation through temperature increase was used to dissociate the CO_2 hydrate plug after the long-term integrity of the plug was verified (Fig. 9). The theoretical CO_2 hydrate dissociation temperature was already reached at T = 1.2 °C given the moderate overpressure at the production side, but dissociation was not observed until some minutes later when the temperature had increased to 2.3 °C. One hour later the CO_2 hydrate plug was completely dissociated and the flow of CO_2 recommenced. The amount of released CO_2 gas during the dissociation process was quantified and used to estimate the CO_2 hydrate saturation in the core as approximately, S_H = 5%. The magnitude of the CO_2 hydrate saturation had thus been small but still effective in blocking the flow through the core. The CO_2 hydrate most likely formed at the interface between CO_2 gas and residual liquid water, which has been previously observed for liquid CO_2 at higher pressure (Almenningen et al., 2018). A thin but extensive solid CO_2 hydrate layer immobilized the flow channels of gaseous CO_2. The blocking was probably most pronounced in pore throats connecting the intergranular pores (Fig. 3b).

4. Concluding remarks

The effectiveness of CO_2 hydrate self-sealing was verified in a core plug retrieved from the Helvetiafjellet Formation in Svalbard, Norway. 0.40 PV (frac.) of CO_2 was injected at reservoir P,T conditions before the flow of CO_2 was blocked by CO_2 hydrate formation. A repeated test, where initial flow of CO_2 through the core was established, also led to complete blocking of CO_2 flow when the injection and production pressure were increased above the CO_2 hydrate stability pressure. The flow of CO_2 was effectively stopped when the P,T conditions were favorable for hydrate formation, independent of whether CO_2 displaced water for the first time or CO_2 flowed in already established flow channels in conjunction with residual water. The formed CO_2 hydrate seal was impermeable for the entire length of the experiments (several hundred hours).

The core plug experiments in this work demonstrates the potential of CO_2 hydrate self-sealing as a secondary safety factor in the CCS

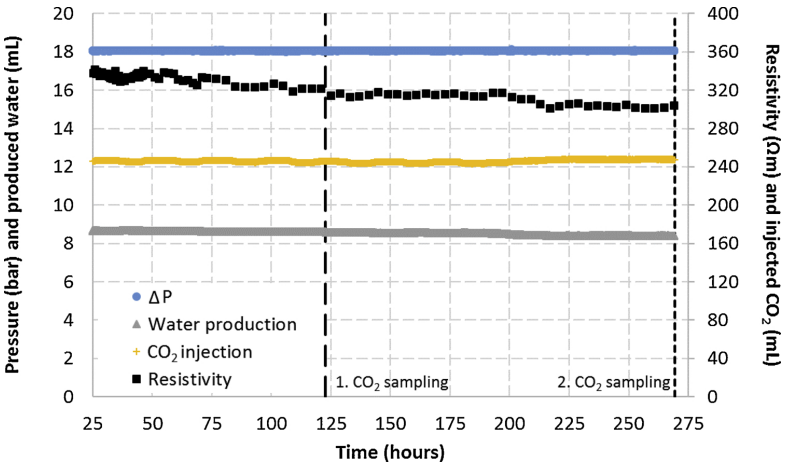

Fig. 6. Long-term stability of the CO_2 hydrate plug at T = 0.1 °C and constant differential pressure across the core equal to 18 bar (blue circles). No CO_2 was injected (yellow pluses) and no water was produced (gray triangles) during 250 h. The effluent water was sampled for CO_2 twice, but no CO_2 escaped through the hydrate-plugged core.

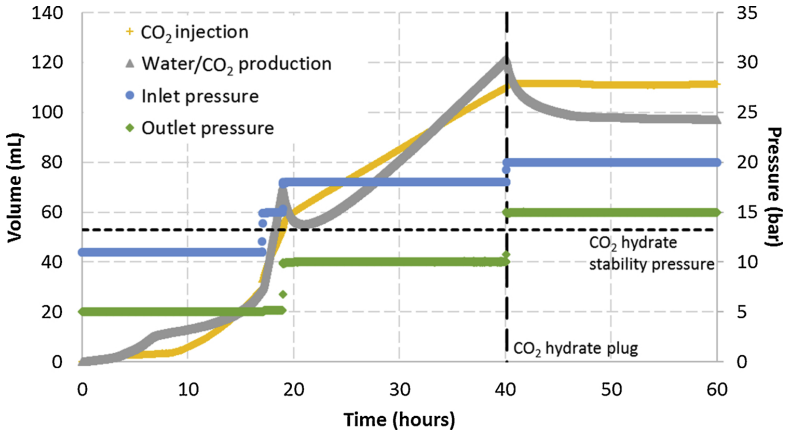

Fig. 7. Pressure-controlled CO_2 injection (yellow pluses) below and above the CO_2 hydrate stability pressure (P = 13.2 bar) at T = 0.1 °C. The flow of CO_2 through the core was sustained even when the injection pressure (blue circles) was set to 18 bar and the production pressure (green diamonds) was set to 10 bar. CO_2 hydrate plugging commenced after 40 h when the injection and production pressure were set to 20 bar and 15 bar, respectively. The CO_2 hydrate stability pressure is calculated with the CSMGem software (Colorado School of Mines, 2015).

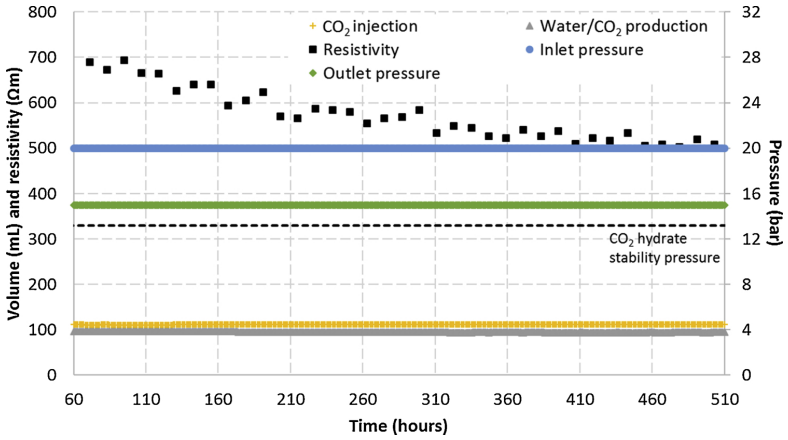

Fig. 8. Long-term stability of the CO_2 hydrate plug at T = 0.1 °C and constant differential pressure across the core equal to 5 bar. No CO_2 was injected (yellow pluses) and no water was produced (gray triangles) during 450 h. The CO_2 hydrate stability pressure is calculated with the CSMGem software (Colorado School of Mines, 2015).

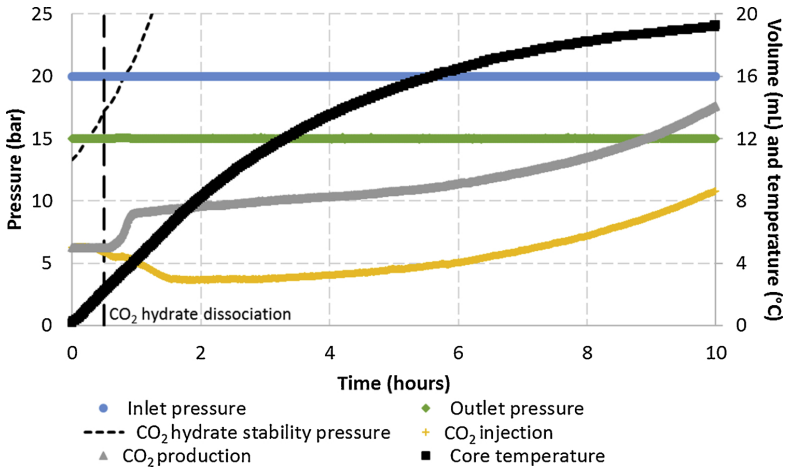

Fig. 9. Thermal dissociation of CO_2 hydrate plug at constant injection pressure (blue circles) equal to 20 bar and constant production pressure (green diamonds) equal to 15 bar. The CO_2 hydrate plug started to dissociate after 0.5 h when the temperature reached 2.3 °C (black squares). The flow of CO_2 through the core was recommenced after approximately 2 h. The CO_2 hydrate stability curve is calculated with the CSMGem software (Colorado School of Mines, 2015).

project in Longyearbyen. In the unlikely event of CO_2 leakage through the top seal overlying the CO_2 injection target, the CO_2 will react with the pore water and form hydrates at the prevailing *P,T* conditions in the Helvetiafjellet Formation. The results suggest that the CO_2 hydrate self-sealing is not limited to CO_2 sequestration in shallow marine aquifers, but applies as well to CO_2 storage projects in permafrost settings. The hydrate blockage of pores is more effective in low permeability rock with tight pores than in high permeability rock associated with unconsolidated sediments offshore. The long-term integrity of the formed hydrate seal cannot be determined through laboratory core plug experiments alone, and should be investigated by field-scale numerical simulations. Further, it should be considered that the hydrate seal will be prone to vertical shifts in response to changing surface temperatures, and the upward movement of the CO_2 hydrate stability zone potentially caused by global warming.

Acknowledgements

The authors would like to acknowledge Equinor for financial support and the use of the MRI facility at Equinor's laboratories in Bergen. The core sample and reservoir conditions were provided by the Longyearbyen CO_2 Lab project (http://co2-ccs.unis.no). The constructive feedback from two anonymous reviewers is much appreciated.

References

Almenningen, S., Gauteplass, J., Fotland, P., Aastveit, G.L., Barth, T., Ersland, G., 2018. Visualization of hydrate formation during CO2 storage in water-saturated sandstone. Int. J. Greenh. Gas Control 79, 272–278.

Almenningen, S., Gauteplass, J., Hauge, L.P., Barth, T., Fernø, M.A., Ersland, G., 2019. Measurements of CH4 and CO2 relative permeability in hydrate-bearing sandstone. J. Pet. Sci. Eng. 177, 880–888.

Arts, R.J., Chadwick, A., Eiken, O., Thibeau, S., Nooner, S., 2008. Ten Years' Experience of Monitoring CO2 Injection in the Utsira Sand at Sleipner, Offshore Norway. First Break, pp. 26.

Bachu, S., 2000. Sequestration of CO2 in geological media: criteria and approach for site selection in response to climate change. Energy Convers. Manage. 41, 953–970.

Bachu, S., 2015. Review of CO2 storage efficiency in deep saline aquifers. Int. J. Greenh. Gas Control 40, 188–202.

Bælum, K., Johansen, T.A., Johnsen, H., Rod, K., 2012. Subsurface structures of the Longyearbyen CO2 Lab study area in Central Spitsbergen (Arctic Norway), as mapped by reflection seismic data. Nor. J. Geol. 92, 377–389.

Baklid, A., Korbol, R., Owren, G., 1996. Sleipner vest CO2 disposal, CO2 injection into a shallow underground aquifer. SPE Annual Technical Conference and Exhibition.

Betlem, P., Senger, K., Hodson, A., 2019. 3D thermobaric modelling of the gas hydrate stability zone onshore central Spitsbergen, Arctic Norway. Mar. Pet. Geol. 100, 246–262.

Birchall, T., Senger, K., Braathen, A., Olaussen, S., 2018. Subnormal pressure regimes of the northern Barents Shelf: causes and implications for hydrocarbon exploration. EAGE Annual Conference & Exhibition.

Bjørlykke, K., Elvekhøi, B.A., Malm, A.O., 1979. Diagenesis in Mesozoic sandstones from Spitsbergen and the North Sea—a comparison. Geol. Rundschau 68, 1152–1171.

Blunt, M., Fayers, F.J., Orr, F.M., 1993. Carbon dioxide in enhanced oil recovery. Energy Convers. Manage. 34, 1197–1204.

Börner, J.H., Herdegen, V., Repke, J.U., Spitzer, K., 2015. The electrical conductivity of CO2-bearing pore waters at elevated pressure and temperature: a laboratory study and its implications in CO2 storage monitoring and leakage detection. Geophys. J. Int. 203, 1072–1084.

Braathen, A., Bælum, K., Christiansen, H.H., Dahl, T., Eiken, O., Elvebakk, H., Hansen, F., Hanssen, T.H., Jochmann, M., Johansen, T.A., Johnsen, H., Larsen, L., Lie, T., Mertes, J., Mørk, A., Mørk, M.B., Nemec, W., Olaussen, S., Oye, V., Rød, K., Titlestad, G.O., Tveranger, J., Vagle, K., 2012. The Longyearbyen CO2 Lab of Svalbard, Norway—initial assessment of the geological conditions for CO2 sequestration. Nor. J. Geol. 92, 353–376.

Colorado School Of Mines, 2015. Center for Hydrate Research. [Online]. Available: http://hydrates.mines.edu/CHR/Software.html (Accessed 2 March 2016). .

Doughty, C., Freifeld, B.M., Trautz, R.C., 2008. Site characterization for CO2 geologic storage and vice versa: the Frio brine pilot, Texas, USA as a case study. Environ. Geol. 54, 1635–1656.

Eiken, O., Ringrose, P., Hermanrud, C., Nazarian, B., Torp, T.A., Høier, L., 2011. Lessons learned from 14 years of CCS operations: Sleipner, In Salah and Snøhvit. Energy Procedia 4, 5541–5548.

Gauteplass, J., Almenningen, S., Ersland, G., Barth, T., 2018. Hydrate seal formation during laboratory CO2 injection in a cold aquifer. Int. J. Greenh. Gas Control 78, 21–26.

Grundvåg, S.E., Jelby, M.E., Sliwinska, K.K., Nøhr-Hansen, H., Aadland, T., Sandvik, S.E., Tennvassås, I., Engen, T., Olaussen, S., 2019. Sedimentology and palynology of the Lower Cretaceous succession of central Spitsbergen: integration of subsurface and outcrop data. Nor. J. Geol. http://www.arcex.no/norwegian-journal-of-geology-sedimentology-and-palynology-of-the-lower-cretaceous-succession-of-central-spitsbergen-integration-of-subsurface-and-outcrop-data/.

Hågenvik, C., 2013. CO2 Injection in Hydrate Bearing Sandstone with Excess Water. MSc. University of Bergen, Norway.

Hauge, L.P., Gauteplass, J., Høyland, M.D., Ersland, G., Kovscek, A., Fernø, M.A., 2016. Pore-level hydrate formation mechanisms using realistic rock structures in high-pressure silicon micromodels. Int. J. Greenh. Gas Control 53, 178–186.

Hodson, A.J., Nowak, A., Redeker, K.R., Holmlund, E.S., Christiansen, H.H., Turchyn, A.V., 2019. Seasonal dynamics of methane and carbon dioxide evasion from an open system Pingo: Lagoon Pingo, Svalbard. Front. Earth Sci. 7.

IPCC, 2014. R.K. Pachauri L.A. Meyer Geneva, SwitzerlandClimate Change 2014: Synthesis Report. Contribution of Working Groups I, II and III to the Fifth Assessment Report of the Intergovernmental Panel on Climate Change [Core Writing Team2014. Pachauri, R.K., Meyer, L.A. (Eds.), Climate Change 2014: Synthesis Report. Contribution of Working Groups I, II and III to the Fifth Assessment Report of the Intergovernmental Panel on Climate Change [Core Writing Team.

Kempka, T., Kühn, M., Class, H., Frykman, P., Kopp, A., Nielsen, C.M., Probst, P., 2010. Modelling of CO2 arrival time at Ketzin – part I. Int. J. Greenh. Gas Control 4, 1007–1015.

Kleinberg, R.L., Flaum, C., Griffin, D.D., Brewer, P.G., Malby, G.E., Peltzer, E.T., Yesinowski, J.P., 2003. Deep sea NMR: methane hydrate growth habit in porous media and its relationship to hydraulic permeability, deposit accumulation, and submarine slope stability. J. Geophys. Res. Solid Earth 108, 1–17.

Koevoets, M.J., Hammer, Ø., Olaussen, S., Senger, K., Smelror, M., 2018. Integrating subsurface and outcrop data of the Middle Jurassic to Lower Cretaceous Agardhfjellet Formation in central Spitsbergen. Nor. J. Geol. 98.

Koide, H., Takahashi, M., Tsukamoto, H., Shindo, Y., 1995. Self-trapping mechanisms of carbon dioxide in the aquifer disposal. Energy Convers. Manage. 36, 505–508.

Koide, H., Takahashi, M., Shindo, Y., Tazaki, Y., Iijima, M., Ito, K., Kimura, N., Omata, K., 1997. Hydrate formation in sediments in the sub-seabed disposal of CO2. Energy 22, 279–283.

Michael, K., Golab, A., Shulakova, V., Ennis-King, J., Allinson, G., Sharma, S., Aiken, T., 2010. Geological storage of CO2 in saline aquifers—a review of the experience from existing storage operations. Int. J. Greenh. Gas Control 4, 659–667.

Mitchell, J., Chandrasekera, T.C., Holland, D.J., Gladden, L.F., Fordham, E.J., 2013. Magnetic resonance imaging in laboratory petrophysical core analysis. Phys. Rep. 526, 165–225.

Mulrooney, M.J., Larsen, L., Van Stappen, J., Rismyhr, B., Senger, K., Braathen, A., Olaussen, S., Mørk, M.B.E., Ogata, K., Cnudde, V., 2019. Fluid flow properties of the Wilhelmøya Subgroup, a potential unconventional CO2 storage unit in central Spitsbergen. Nor. J. Geol. 99.

Ogata, K., Senger, K., Braathen, A., Tveranger, J., Olaussen, S., 2012. The Importance of Natural Fractures in a Tight Reservoir for Potential CO2 Storage: A Case Study of the Upper Triassic–middle Jurassic Kapp Toscana Group (Spitsbergen, Arctic Norway). Geological Society, London Special Publications, 374, SP374.9.

Ramstad, T., Rueslåtten, H., 2013. Pore Scale Numerical Analysis for Geological Sequestration of CO2. Technical Report, 1-63.

Senger, K., Tveranger, J., Braathen, A., Olaussen, S., Ogata, K., Larsen, L., 2015. CO2 storage resource estimates in unconventional reservoirs: insights from a pilot-sized storage site in Svalbard, Arctic Norway. Environ. Earth Sci. 73, 3987–4009.

Senger, K., Mulrooney, M.J., Braathen, A., Ogata, K., Olaussen, S., 2016. Integrated characterization of an organic-rich Caprock Shale, Svalbard, Arctic Norway. Fifth EAGE Shale Workshop.

Sloan, E.D., Koh, C., 2008. Clathrate Hydrates of Natural Gases. CRC Press, Boca Raton, Florida.

Tohidi, B., Yang, J., Salehabadi, M., Anderson, R., Chapoy, A., 2010. CO2 hydrates could provide secondary safety factor in subsurface sequestration of CO2. Environ. Sci. Technol. 44, 1509–1514.

Udachin, K.A., Ratcliffe, C.I., Ripmeester, J.A., 2001. Structure, composition, and thermal expansion of CO2 hydrate from single crystal X-ray diffraction measurements. J. Phys. Chem. B 105, 4200–4204.

Graphic design: Communication Division, UiB / Print: Skipnes Kommunikasjon AS

uib.no

ISBN: 9788230852903 (print)
9788230857984 (PDF)